UNIVERSITÀ DEGLI STUDI FIRENZE

Dipartimento di Ingegneria Industriale (DIEF)

Dottorato di Ricerca in Ingegneria Industriale

CICLO XXXIII

Experimental and Computational Analysis of Small-Size Solar Receiver for Industrial and Residential Application

PhD Candidate
Sahand Hosouli

Tutor
Prof. Maurizio De Lucia

Supervisor
Dr. Giacomo Pierucci

Coordinator
Prof. Giampaolo Manfrida

"One, remember to look up at the stars and not down at your feet. Two, never give up work. Work gives you meaning and purpose and life is empty without it. Three, if you are lucky enough to find love, remember it is there and don't throw it away."

— Stephen Hawking

I am dedicating this PhD research thesis to my father and my mother for their endless Love. My mum is my mentor, providing guidance in many aspects of my life. I have learned to be a better person because of her and I am very grateful for that. My dad brought me lots of joy and laughter during my studies. He is supportive of anything I do. Although he is the most optimistic person on the planet, he always makes me look on the bright side when things get tough. I would never have accomplished this much in life without their love and continued support. Thank you for teaching me to believe in my dreams and myself.

This thesis is not only the product of my years as a doctoral student but also the many people that supported me in this endeavor. There are far too many to thank in this space. Yet some must be named. I would like to thank, first and foremost, my advisor Professors Maurizio De Lucia, whose patience, wisdom, kindness, and unrelenting support literally made this thesis possible

Moreover, I owe a debt of gratitude to my supervisor Dr. Giacomo Pierucci for all his interest in my work and for the guidance that he has been constantly providing to me. I'm deeply thankful for his advice and support on this project. His assistance, words of encouragements and knowledge positively impact this PhD research work.

I would like to thank all of my friends who have helped and supported me during my time in Italy. Friends from University of Florence and beyond—Hamid Rashidi, Nathan Formosa, Milad Mirabedin, Pardis Pahlevani, Elnaz Zaher, Maryam Khodayeki, Shahin Saleh and Hooman Faghir.

And last but not least, I would like to thank Rosa who supported me in ways too many to list throughout the years in Firenze.

Sahand

Summary

Use of solar thermal energy in residential and industrial applications has to be sustained to reduce the concentration of greenhouse gas in atmosphere due to the exploitation of fossil fuels in producing energy. In this context, the renewable energies play an important role. The energy request in industrial and residential sector involves a noticeable fraction (more than 50%) of the total requested supply for human activities. Concentrating collectors could be the right technology to produce heat at medium temperature (between 85 and 250°C) to provide thermal energy to users with high consumption rates and low-temperature heat demand like domestic hot water and space heating in addition to the industrial process heat applications.

Thus, in this study UF-RT01 receiver (University of Florence Receiver Tube 01) of small size parabolic trough collector called m-PTC were investigated experimentally by indoor and outdoor tests and computationally by 3D heat transfer FEM model. The m-PTC suitable to be integrated in the roof of industrial environments where the space for installation of solar collectors is in general limited and the heat demand temperature is below than 200°C.

The UF-RT01 receiver has a specific design, being formed by two coaxial tubes so that the fluid inlet and output are at the same side. It was properly developed to scale the PTC technology toward smaller size (chord length from 6-8 meters to around 0.5 m): the purpose is the installation in urban context and the application in industrial process. The outer absorber tube is made of steel and has a diameter of 10 mm (1 mm thickness) for a length of 1860 mm; the smaller coaxial tube is made of steel and has an internal diameter of 6 mm (0.5 mm thickness). Furthermore, a selective coating has been selected to reduce the emission in infrared range and increase the energy absorption in solar spectral range. Inside, a vacuum level is fixed at 10^{-4} mbar to reduce the heat losses to the radiative ones.

In order to study the thermal losses of the receiver, two different indoor test stand have been realized. The thermal loss measurement is set up under indoor test without Sun irradiance, imposing a controlled internal heating. This process is based on the Joule effect, feeding electric heaters with current to obtain a steady state condition at different reference temperatures. In preliminary test stand by removing the inner coaxial steel tube, two nickel-chrome wire heaters are inserted along the length of absorber tube. An additional external heater is also placed before the Kovar part to meet the adiabatic condition and minimizing the temperature gradient. The UF-RT01 has been analyzed experimentally and performances are evaluated as a function of different operating temperatures, reaching up to 180°C. A maximum value for heat loss amounts at about 24 W when ΔT is 161°C (receiver average temperature of 180°C). In order to obtain more uniformity of temperature along the absorber tube the second test set up has been developed for thermal loss measurement and instead of nickel-chrome wire heater, an industrial cartridge heater made of resistance wire (NiCr20/80) as a core covered with stainless steel 304 as a sleeve (sheath) has been used. Three different tube from same type (UF-RT01) have been tested in the range of interest and the procedure was repeated for about 150 cases. In comparison to preliminary test stand, results showed more uniformity in temperature distribution along the tube. A maximum value of 17.89 W is found when ΔT is 163°C (receiver average temperature of 190°C).

In order to achieve production assurance and have more clear vision about the results due to the different results obtained from test on RT03 in comparison to the RT01 and RT02 with higher thermal loss, new tests have been conducted on additional tubes. Similar setup and test procedure

have been conducted in order to evaluate the uniformity of temperature along the tube and estimate the heating supplier parameters in additional tubes. Seven different tube from same type have been tested and labeled as RT04-RT10. Results from tests on RT01 and RT02 are in accordance with new results obtained from heat loss test on RT04-RT10. Therefore, the different results related to the RT03 are to be expected as a result of variation in production quality by manufacturer of receiver tube.

The Finite Element Method (FEM) has been used in order to predict the thermal performance and analyze the relevant physical characteristics of the receiver tube (specially the value of emissivity at higher temperature). Heat transfer model using FEM simulation method has been realized with Comsol Multiphysics software. An adaptive mesh refinement (AMR) with different mesh configurations has been conducted in order to increase storage and computational savings. By using a parametric sweep to vary the maximum element size, the model solved using meshes with different mesh density in order to study how it affects the solution. The heat transfer model is able to precisely predict the heat losses at low temperature of the absorber tube with constant value of emissivity reported by manufacturer. The estimation of emissivity at the higher temperature obtained by solving the model with various emissivity values for each test at specific input power until the average temperature inside the absorber tube obtained by simulation were in agreement with experimental value. The obtained emissivity function has been used in model in order to solve the model for various input power values and the results showed that the model and emissivity function are able to predict the thermal loss with high accuracy.

In order to perform the out-door test according the designed and assembled test rig platform at first phase has been slightly modified to reduce the heat losses and reach stable inlet temperature . The reliability of implemented test bench and output power and efficiency of a novel small size parabolic trough collector have been evaluated by preliminary test. For this purpose an out-door tests at ambient temperature on the designed small size PTC test rig is carried out during clear sky day. Furthermore, the peak optical efficiency test has been conducted based on introduced requirements at quasi-steady condition. The general point of the outdoor efficiency test is extracting the efficiency curve of the collector for normal incidence based on the efficiency curve coefficients. 24 tests have been done under various inlet temperature and irradiance under clear sky condition and the exemplary performance measurement data for present research stems from 153 experimental points.

The preliminary out-door experimental test on the collectors showed that the test rig meets the initial design expectations in order to control the system in stable condition. The peak optical efficiency test has been conducted at quasi-steady condition and the average peak optical efficiency of the collector is 61.8% with total absolute error of 1.4%. With regard to the peak optical efficiency and for assuring that experimental results from the outdoor testing are valid, a cross check with the efficiency curve of the collector by weighted least squares (WLS) fitting shows almost similar values. The obtained value for peak optical efficiency from efficiency curve is 62.1%. Efficiency measurement of solar collector have been conducted from inlet temperature of 28 °C up to 123°C for various DNI values. A Maximum of 63.1% for thermal efficiency is found when the inlet temperature is 28.41°C and a minimum of 54.6% corresponds at 122.90°C. The total standard absolute uncertainty of thermal efficiency for test at inlet temperature of 28.41°C and 122.90°C are 0.7% and 0.8%, respectively. The efficiency curve of the collector by WLS fitting were also obtained from outdoor test results

Index

List of Figures

List of Tables

List of Original Publications

1. Pierucci, G., Hosouli, S., De Lucia, M., et al., Experimental Methodology and Thermal Loss Tests on Small Size Absorber Tubes for Solar Applications. Energies, 11(10), 2552, 2018.

2. Pierucci G, Hosouli S, De Lucia, M., et al., Realization of a test rig for small solar collectors and preliminary test. AIP Conf. Proc., vol. 2126, AIP Publishing LLC; 2019, p. 120016.

3. Salvestroni M, Pierucci G, Hosouli, S., De Lucia, M., et al., Design of a small size PTC: computational model for the receiver tube and validation with heat loss test. IOP Conf. Ser. Mater. Sci. Eng., vol. 556, IOP Publishing; 2019, p. 12025.

4. Salvestroni M, Pierucci G, Hosouli, S., De Lucia, M., et al., Design of a seasonal storage for a solar district heating in Florence. IOP Conf. Ser. Mater. Sci. Eng., vol. 556, IOP Publishing; 2019, p. 12026.

1 - Introduction

1.1 - Energy Consumption: Challenges and issues

Environment and energy are the two main issues in front of human beings at the present time. Population growing and industrial developments in the past few centuries have caused in a huge rise in energy demand with an annual increasing rate at about 2.3% [1]. Emissions from consumption of fossil fuels are the primary reason of rapid and accelerating growth in atmospheric CO_2 [2]. The energy demand is increasing rapidly, with an excessive fossil fuels consumption in civil and industrial sectors. Based on annual energy outlook on 2005 due to the growing demand, by 2025 the oil consumption could reach more than 120 million barrels/day [3].

The wave of the global fervor for industrialization has come with its attendant effect of increasing CO_2 emissions which consequently, causes natural reactions in the form of environmental pollution, global warming and climate change [4]. Global energy-related carbon dioxide (CO_2) emissions grew an estimated 1.7% in 2018 due to increased fossil fuel consumption [5]. Human activities are estimated to have caused approximately 1.0°C of global warming and it is possible to reach 1.5°C between 2030 and 2052 if it continues to increase at the present rate [6].

The concentration of CO_2 in the atmosphere has risen from close to 280±10 parts per million (ppm) in 1800, at first slowly and then increasingly faster to a value of 367 ppm in 1999, due to the increasing pace of industrial development and global agricultural after the Industrial Era (about 1750). The following evidences confirms the impact of fossil fuel consumption on atmospheric CO_2 content: in the first place, similar rate of atmospheric O_2 reduction with emissions of CO_2 (combustion consumes O_2). In the second place, the lack of ^{14}C, and depleted content of ^{13}C (isotopic signatures of fossil fuel) and last but not least, higher observed CO_2 concentration in the northern hemisphere, where most fossil fuel burning occurs [7].

Figure 1 illustrates the world total primary energy supply shares by fuel in 1973 and 2016. The amount of world total primary energy supply in 1971 accounted for 6101 Mtoe (Millions of tonnes of oil equivalent) and this, rose to nearly 13761 Mtoe in 2016. The energy generated by Oil, which was the first source of energy in the world in 1971, fell by 15% of all energy supply in 2016. In contrast, total energy supply comes from oil, coal and natural gas increase from 5299 Mtoe to 11160 Mtoe in 2016 [8].

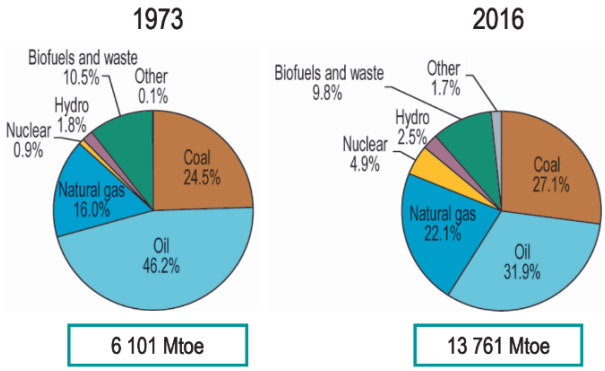

Figure 1. World total primary energy supply [8].

Based on International energy outlook 2016 report, world energy-related CO_2 emissions projection shows an increase of 34 percent over the projection period between 2010 and 2040. Figure 2 shows an increase from 32.2 billion metric tons in 2012 to 35.6 billion metric tons in 2020 [9].

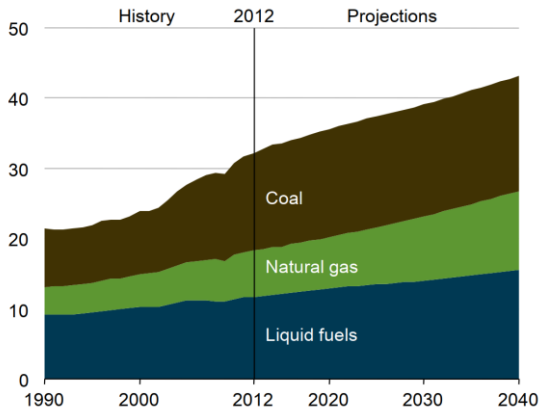

Figure 2. World energy-related carbon dioxide emissions by fuel type [9].

As previously stated, the concentration of greenhouse gas in atmosphere dramatically has increased due to the exploitation of fossil fuels to produce energy (e.g. electric, heat) [10]. As a result, several strategies have to be carried out in order to reduce the fossil fuels consumption. In this context, the renewable energies play an important role [11].

Renewable energy source (RES) includes solar, biomass, geothermal, hydropower and wind energies and these resources could provide energy with almost zero emissions of greenhouse-gases (GHG) and air pollutants [12]. RESs supply 14% of the total world energy demand and the share of RESs is anticipated to significantly increase to 30–80% in 2100 [13,14].

In the EU, the energy was mainly consumed by four sectors in 2014 (transport, industry, residential and services). Figure 3 shows final energy consumption by sectors in the EU [15].

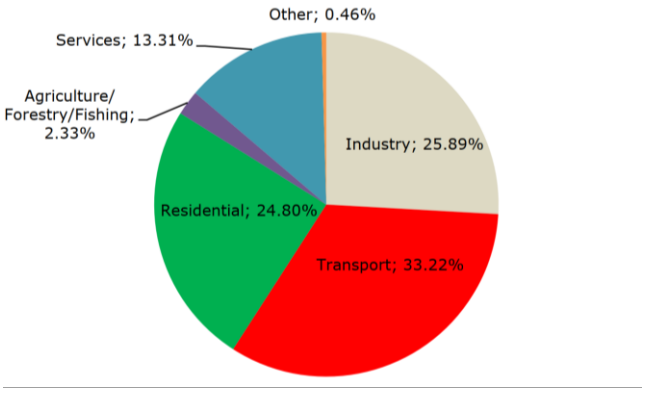

Figure 3. Final energy consumption by sectors in the EU [15].

International Energy Agency (IEA) statistics (2018) reports that, industry is the main energy consumer in top five countries by total final consumption. For example in China, final energy consumption related to industry is around 50% [8]. By the sector, about 32-35% of total global energy consumption is related to the industrial section and 74% of this fraction is used to meet the process heat demand and 26% is related to the electricity [16,17].

Space heating, space cooling, process heating, process cooling, cooking and water heating are six main final energy consumption related to heating and cooling. In 2015, heating sector including space heating, process heating, cooking and water heating was the main area of consumption by 96% of final energy demand for heating and cooling in EU. In contrast, cooling sector including space cooling and process cooling was about 4% of final energy demand for heating and cooling in EU. Figure 4 shows that about 85% of final energy demand for heating and cooling was used in buildings for space heating (54%) and in the industry for process heating (32%) [18].

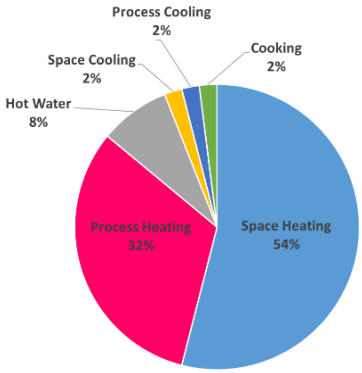

Figure 4. Final energy demand for heating and cooling in the EU by sector in 2015.

Final energy demand for heating and cooling by fuel source in the EU in 2015 reported by Heat Roadmap Europe (HRU) shows that about 66% of final energy demand provided by fossil fuels and in detail 42% by gas, 12% by oil and 12% by coal [19].

Renewable sources can play an important role in reducing the consumption of fossil fuels. The energy request in industrial and residential sector involves a noticeable fraction (more than 50%) of the total requested supply for human activities in the EU [20,21]. The only way to meet this global energy demand without contributing to climate change and environmental problems implies the utilization of renewable sources [21].

1.2 - Fundamentals of Low and Medium-Temperature Solar Thermal Energy

1.2.1 - Solar Energy Technologies

Climate change is likely to affect both energy consumption and energy production in many parts of the world [22]. The rise of attention in solar energy application has taken place since 1970, due to the then increasing cost of energy from conventional sources. Solar radiation is the most abundant and permanent energy source on Earth. The amount of solar energy received by the surface of the earth per minute is larger than the energy consumption by the whole population in a year [23].

The solar energy concept is defined as collecting and utilization of light and/or heat energy generated by the Sun and its related technologies (passive and active) [24]. Figure 5 shows present solar energy technologies classification.

The gathering of solar energy without transforming thermal or light energy into any other form is called passive technology. An example of passive solar technology is collection, storage and

distributing of solar heat energy for the domestic heating (especially during the winter season). The collecting of solar radiation and using mechanical and electrical equipment (such as pumps or fans) to convert the solar energy to heat and electric power is called active solar technology [11].

Active solar energy technology classified into photovoltaic technology, solar thermal technology and concentrated solar power technology. In the past few years, the direct conversion of sunlight into electrical energy by semiconductors has become one of the most promising photovoltaic technology. The application of solar energy for thermal energy requirements of domestic and/or industrial sector such as heating, cooling, drying, cooking, etc. is called solar thermal technology or concentrated solar thermal (CST). On the other hand, concentrated solar power (CSP) technologies are being employed to generate electricity [11,25,26].

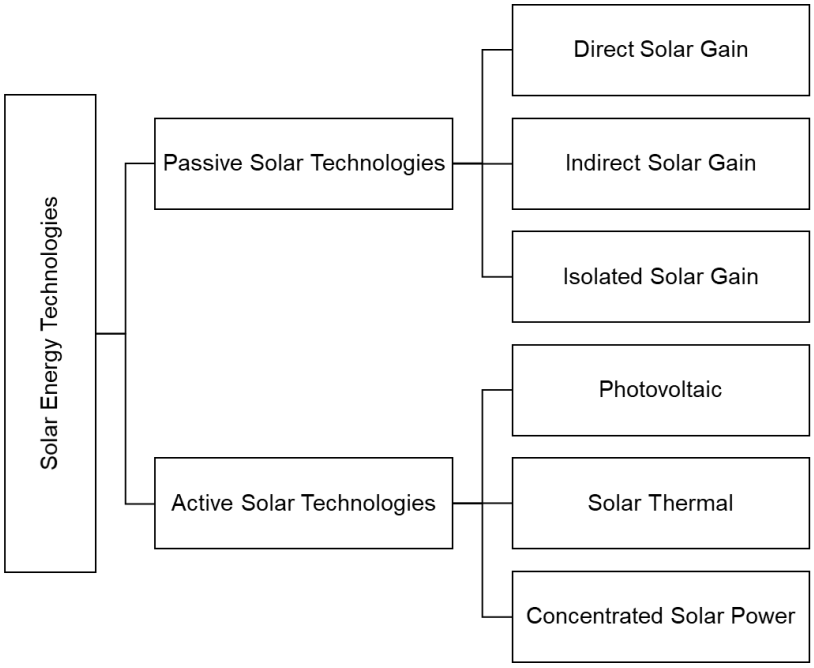

Figure 5. Classification of the present solar energy technologies.

CSP technology using mirrors and sunlight is reflected to a receiver where heat is collected by a thermal energy carrier (primary circuit). Collected heat can be used directly for water/steam or through secondary circuit to power a turbine and generate electricity [27].

Four types of CSP technologies are available, including parabolic trough collector (PTC), parabolic dish systems (PDS), linear Fresnel reflector (LFR) and solar power tower (SPT). Figure 6 shows schematics of currently available CSP technologies [28].

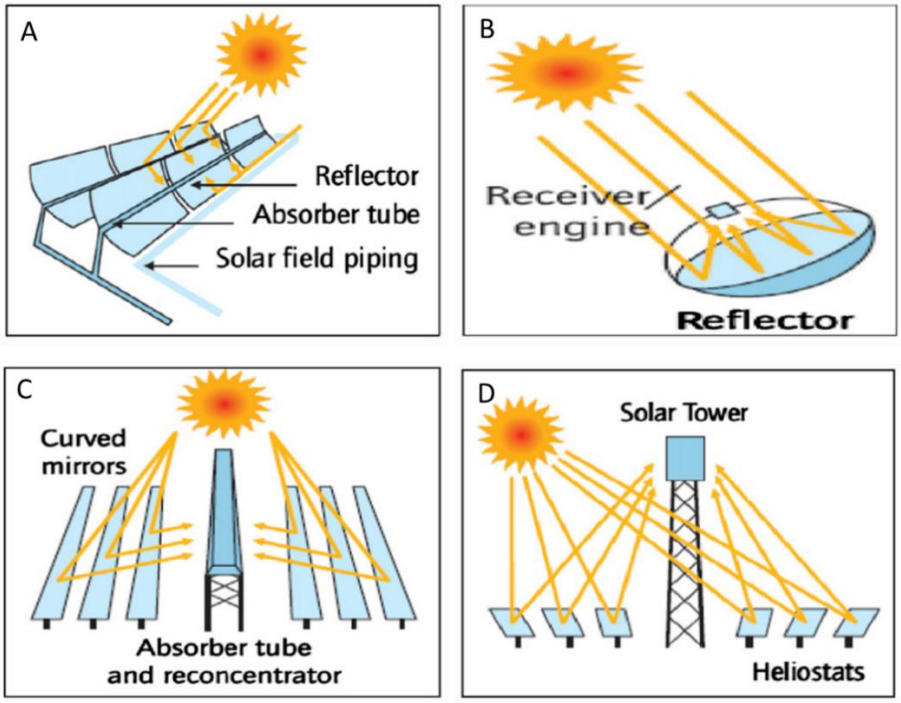

Figure 6. Currently available CSP technologies: (A) PTC; (B) PDS; (C) LFR; (D) SPT [28].

Figure 7 shows the installed operational CSP technologies statistics by country and type of technology reported in 201, the majority of CSP technologies are currently located in Spain and USA (about 98%). It is clear that among the CSP technologies, PTC technology represents the largest portion by 96.3%, whereas PDS is the smallest by 0.1% [27].

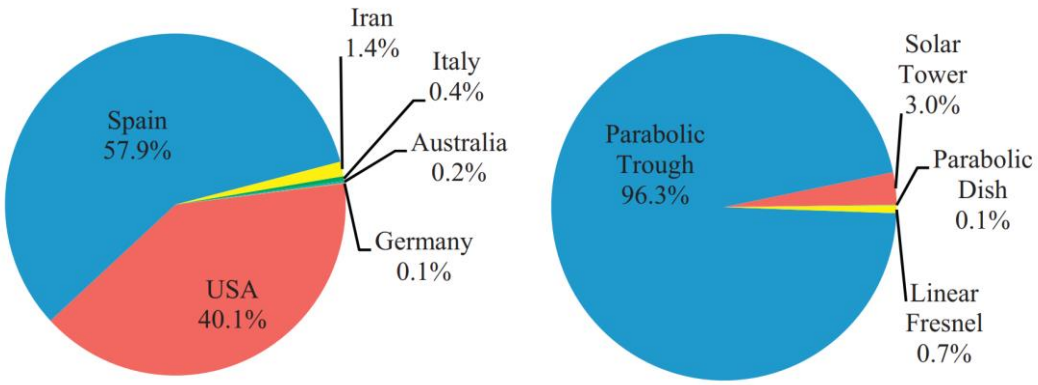

Figure 7. Installed operational CSP power (March 2011), by country and by technology [27].

Operation temperature for industrial process heat is divided into three ranges: low (T<100°C), medium (100°C<T<250°C) and high (T>250°) [29]. Less than a third of industrial heat energy consumption is under 150°C, 22% is related to the temperature range of 150°C to 400°C and just under a half (48%) is related to the high temperature (above 400°C) [8,30].

Concentrating collectors could be the right technology to produce heat at medium temperature to provide thermal energy to users that require temperatures between 85 and 250°C. Users with high consumption rates and low-temperature heat demand like domestic hot water and space heating in addition to the industrial process heat applications like ironing, cleaning, drying, sterilization, etc. are the main medium temperature users [31–33]. However, IEA reported on December 2015 that

0.3% of total installed solar thermal capacity (about 88MWth) is related to the solar heat for industrial processes [29].

The markets and potential sites for CSP plants are located in areas known as the "Sun Belt" where greater solar radiation is available from the sun. These areas around the world are generally being identified by using the global distribution of Direct Normal Irradiance (DNI) [34]. Figure 8 shows the worldwide distribution of the DNI reported by Solargis (Global Solar Atlas 2.0) on 2019 [35].

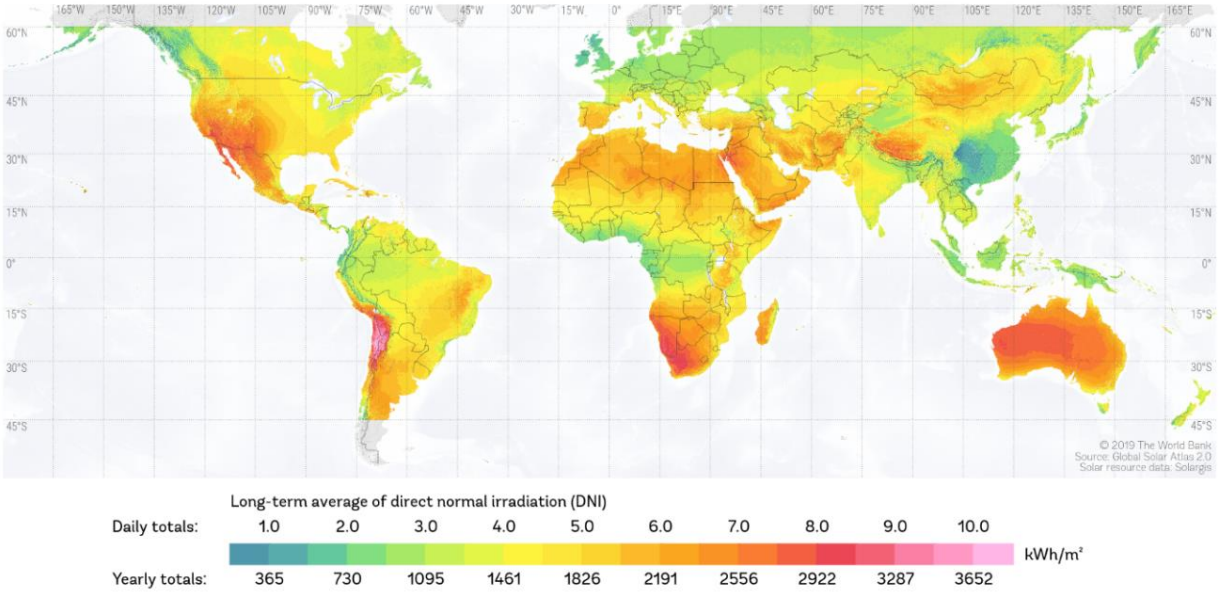

Figure 8. Map of worldwide distribution of DNI [35].

Commercially feasible CSP plants should maintain a DNI levels above 2000 kW·h/m^2/yr and DNI level has a major impact on Levelized Cost Of Energy (LCOE) of the plant, current commercial CSP plants are being developed based on this level of irradiance and countries with extremely high radiation levels such as South Africa or Chile came into focus during recent project developments [34,36].

Figure 9 illustrates the distribution of DNI in Italy reported by Solargis (Global Solar Atlas 2.0) on 2019 [35]. Italy has conditions suitable for CSP development only in limited areas in terms of favorable land morphology for solar field installations and high level of DNI. The most desirable locations in Italy for CSP developments are main islands (Sardinia and Sicily) and south regions where the DNI level is above 1800 kW·h/m2/yr. Figure 10 shows the 5 MW Archimede solar plant with molten salt as heat transfer fluid in Sicily. Currently, there are several projects under development mainly in Sardinia and Sicily and the Italian action plan for renewable energy sources launched in 2010 set a target of 17% share of total energy consumption from renewable energy sources by 2020. [37].

Figure 9. Map of distribution of DNI in Italy [35].

Figure 10. Archimede solar plant in Sicily [37].

The four main CSP technologies are different in their general design and focusing principles. Nevertheless, there are common features for subcomponents of a CSP power plant. In general, CSP systems are based on the concept of concentrating solar radiation to produce steam (hot air) for electricity generation using conventional power cycles or heat for low-medium temperature applications [38]. Concentrator is the optical system which directs the solar radiation on to the absorber, while the system including the absorber, its cover and other accessories is defined receiver. Depending on CSP technology the reflecting surfaces may be parabolic, spherical or flat and continuous or segmented [21]. CSP systems consist of a large reflective surface collecting the incoming solar radiation and concentrating it onto a solar receiver with a small aperture area. An

ideal solar receiver would have small conduction and convection heat losses with a high solar absorptance. The receiver absorbs the solar radiation and transfers the heat to a fluid. This hot heat transfer fluid may directly drive a heat engine, transfer the heat to a secondary cycle (such as steam generation), or allow storing the energy for later use during hours without sunshine [39].

Table 1 shows a summary on the components of a solar field and the respective assessment parameters suggested by German Aerospace Center (DLR). Durability is required as a prior condition for all these components and a minimum lifetime of 20 years is required for all components of the solar field [36].

Table 1. Components of the solar field and assessment parameters.

Component	Assessment parameter
Reflectors/mirrors	Reflectance, shape
Receivers	Absorptance, emittance
Collector support structure	Stiffness, mirror attachments
Drives/tracking	Tracking precision, wear
Heat transfer fluid	Chemical stability, hydrogen content, corrosiveness
Flexible Joints	Reactive forces, tightness
Valves, pumps	Functionality
Foundations	Alignment precision

1.2.2 - Solar Thermal Energy Collectors

Table 2 shows a classification of available solar thermal energy collectors available on the market [21].

Table 2. Solar thermal energy collectors available in the market.

Collector	Tracking system	Absorber	T_{max} (°C)
Flat plate	Stationary	Flat	80
Evacuated tube	Stationary	Flat	200
Compound parabolic	Stationary/one-axis	Flat/tubular	250
Parabolic trough	One-axis	Tubular	450
Linear Fresnel	One-axis	Tubular	250
Parabolic dish	Two-axis	Point	1500
Heliostat field	Two-axis	Point	2000

1.2.2.1 Parabolic Trough Collector

Design and construction of PTC depend generally on its applications. Consequently, depending upon the request, several methods can be connected to PTC. However, the most common PTC system includes support mechanism, concentrating reflector, receiver element, Heat Transfer Fluid (HTF), thermal storage device and tracking system [40].

PTCs are designed to track the sun in order to concentrate the solar radiation into a focal line and can be divided into two different parts: concentrator (including the support structure and the reflector) and receiver (including the absorber tube located at the focal axis through which the HTF flows, and the transparent cover). Figure 11 shows a schematic of a typical PTC [21]. A detailed review on solar parabolic trough collector presented in Appendix D.

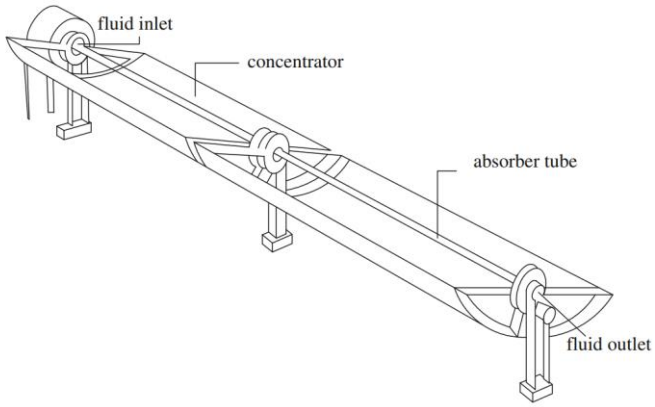

Figure 11. Schematic of a parabolic trough collector [21].

1.2.2.1.1 Structure of parabolic trough collector

The main part of the PTC system is a trough collector. It's characterized by geometrical parameters such as aperture width, rim angle, trough length and focus length. In order to optimize the geometrialc parameters of PTC for making it suitable for various applications as well as different geographical locations, numerous researches are being done. The concentrator in PTCs is a cylindrical parabola which generally presents a reflective surface. The support structure should be able to tolerate aggressive atmospheric conditions (such as wind loads). In general, the tracking system requires the PTC to rotate in one-axis and usually by means of a mechanical transmission system coupled with an electric motorsa [21,40]. Figure 12 shows the geometrical parameters of the trough.

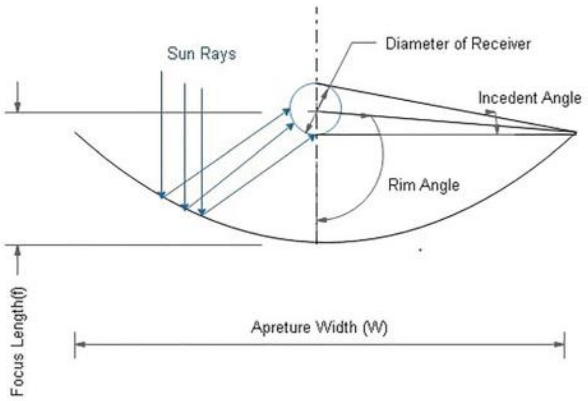

Figure 12. Geometrical Parameters of Trough [40].

In addition to the above mentioned geometrical parameters, trough length and focal length are also used to characterize the form and size of a parabolic trough (Figure 13) [41].

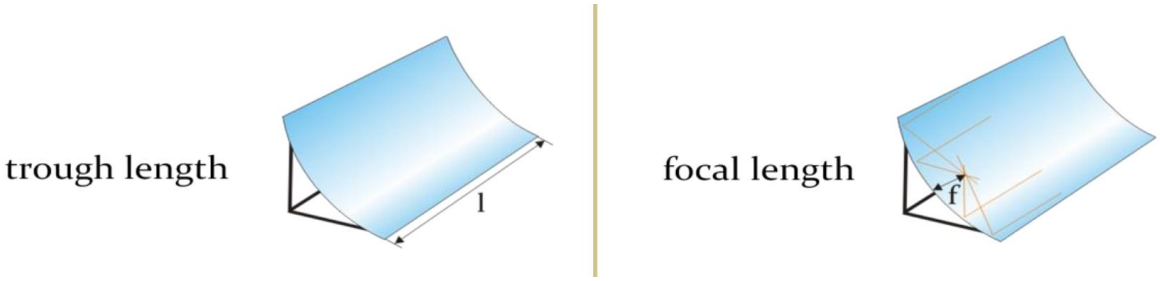

Figure 13. Trough length and focal length of parabolic trough [41].

In order to demonstrate that for axially parallel radiation a parabola has a focal point. A cross section through a parabolic mirror located in a coordinate system, as indicated in Figure 14, it can be represented mathematically as the graph of the function $y = px^2$ [41].

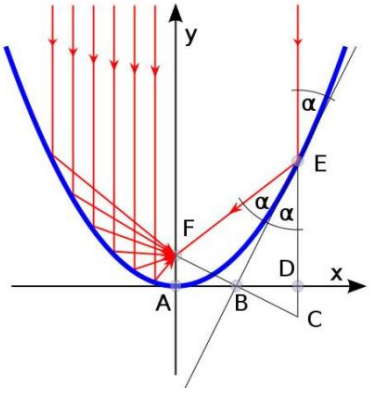

Figure 14. Path of parallel rays at a parabolic mirror [41].

The red lines represent the light that enters the mirror in rays parallel to the parabola's axis and crosses the axis, after reflection, at the focal point *F*. The ray that hits the mirror (the tangent) at the point *E* under the incident angle α, leaves *E* under the same angle. The *E* point is on the graph of the function ($y = px^2$) therefore the coordenates of it can be determined as (x_E ; $p(x_E)^2$). EB vector has the analytical form of $y=2px_Ex+b$ and by filling (x_E ; $p(x_E)^2$) in this equation, we get $y=2px_Ex- p(x_E)^2$. By drawing the line through *F* and *B* and get the point *C* the ΔABF and ΔBCD are congruent and moreover these triangles are similar to ΔBDE. Due to this similarity $AF/AB=BD/DE$. Therefore, $AB=BD=x_E/2$ and $DE=p(x_E)^2$ [41].

The point of intersection of the reflected ray with the x-axis is independent from the incident point *E*. In other words, there is a focal point (*F*) where all incident rays, that enter the mirror parallel to its axis, meet. The distance of the focal point from the vertex (*AF*) is called focal length of a parabola and defined by equation (1). Figure 15 shows the effect of focal length on the shape of parabola [41].

$$f = \frac{1}{4p} \tag{1}$$

Thus, the parabola's analytic representation can be expressed by equation (2).

$$y = \frac{1}{4f}x^2 \tag{2}$$

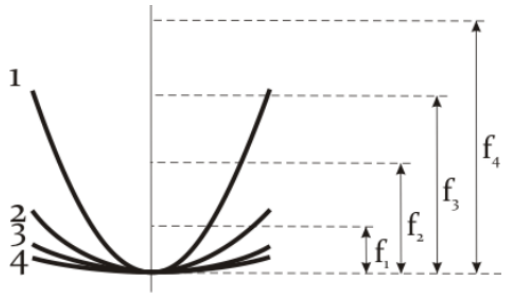

Figure 15. Variation in the shape of parabola by focal length [41].

The angle between the optical axis and the line between the focal point and the mirror rim is called the rim angle. The rim angle can determines the shape of the cross-section of a parabolic trough by itself. In other words, the cross-sections of parabolic troughs with the same rim angle are geometrically similar (If only the shape of a collector cross-section is of interest, but not the absolute size).

The rim angle should neither be too small nor too large. Lower rim angle results in more extended aperture area and higher focal length, which make trough structure large, heavy and costly. While a higher value of rim angle results in lower aperture area and lower focal length. It also results in higher parabolic radius, which is increases the cost of the mirror. Figure 16 shows the relation between the focal length and the rim angle for a constant trough aperture width. The rim angle is a very important constructive feature of collectors. For example, it has an effect on the total irradiance per meter absorber tube [W/m] and on the concentration ratio. There are several principles, which together define the proper rim angle for each application [40,41].

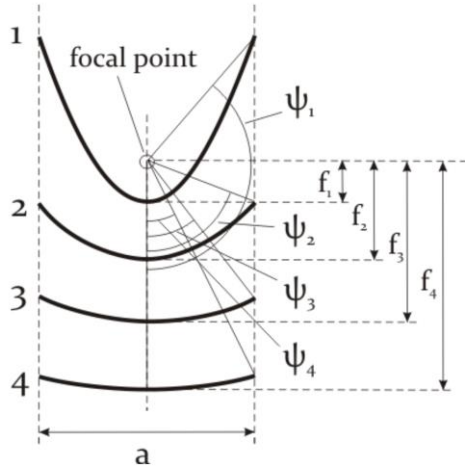

Figure 16. Relation between the focal length and the rim angle for a constant trough aperture width [41].

In addition to the mentioned linear measures, also surface area measures are important. The aperture area is a key constructive measure because it determines the radiation capture at a given

DNI and a given Sun position. The product of the aperture width (a) and the collector length (l) defines the aperture area (A_{ap}) can be expressed by equation (3).

$$\boldsymbol{A_{ap} = a \cdot l} \tag{3}$$

The surface area (A_s) of a parabolic trough also an important factor in order to determine the material need for the trough and can be expressed as follows:

$$\boldsymbol{A_s = S \cdot l}$$

Where S is the length of the parabola that is the cross-section of the trough and l is the collector length. A parabola with the focal length of f is represented analytically by the function $f(x) = x^2/4f$ and S can be calculated as follows:

$$\boldsymbol{S = \int_{-a/2}^{a/2} \sqrt{1 + (f'(x))^2}\, dx}$$

With $a/2$ as the half aperture width, the surface area (A_s) can be determined by equation (4).

$$\boldsymbol{A_s = \left(\frac{a}{2}\sqrt{1 + \frac{a^2}{16f^2}} + 2f \cdot ln\left(\frac{a}{4f} + \sqrt{1 + \frac{a^2}{16f^2}}\right)\right) \cdot l} \tag{4}$$

The concentration ratio (C) is defined by equation (5) as the ratio of the radiant flux density at the focal line (or at the Sun image) (G_{im}) to the direct irradiance at the aperture of the collector ($G_{b,ap}$).

$$\boldsymbol{C = \frac{G_{im}}{G_{b,ap}}} \tag{5}$$

The concentration ratio is one of the fundamental parameters of the collector and it is importat for defining the possible operating temperatures of the parabolic trough power plant. However, it is not the easiet way to report. The irradiance is different in different points of the Sun image and G_{im} has to be determined at a point within the focal line in order to determine the concentration ratio in relation to that specific point.

The useful approximation and easier way to specify the concentration ratio without any measurement is defined by the geometrical concentration ratio (C_G) and can be determined by equation (6).

$$\boldsymbol{C_G = \frac{A_{ap,c}}{A_{ap,r}}} \tag{6}$$

Where the $A_{ap,c}$ is the collector aperture area and $A_{ap,r}$ is the receiver aperture area. By taking the irradiated absorber surface area as the receiver aperture area. In real parabolic troughs, the whole absorber tube surface area ($A_{ap,r} = \pi \cdot d \cdot l$) is the receiver aperture area. Because of the fact that the

absorber tube is not only irradiated by the reflected radiation but also by the radiation that reaches the tube directly. Equation (7) shows the geometrical concentration ratio based on this assumption [41].

$$C_G = \frac{a \cdot l}{\pi \cdot d \cdot l} = \frac{a}{\pi \cdot d} \tag{7}$$

This assumption would results in a lower geometrical concentration ratio. However, the concentration ratio according to the projected areas ($A_{ap,r} = d \cdot l$) is also commonly used.

A.V. Arasu designed and manufactured fiberglass reinforced PTC by hand lay-up method for hot water generation system. The rim angle of the proposed PTC was 90° and an overall thickness of trough was about 7 mm [42].

Schweitzer et al. [43], represented the development of Ultimate Trough (UT) solar collector in order to reduces the solar field cost by 20 to 25%. The UT solar collector by having 247 m length and 7.5 m aperture width was the largest collector up to the date (2014).

Montes et al. [44] reported the design and construction of a PTC for process heat production by applying a series of innovations in the structural layout, the material selection and the adoption of new manufacturing processes. In order to achieve a faster erection on installation site and reduction in production costs. The new tracking system was adopted by using the traction wheel. Peak temperature noted to be 80°C with a volume flow of 0.5 litres/second and moderate thermal efficiency of 60%.

O. Behar et al.[45], developed and validated a novel PTC model. Validation was performed by comparing the results of past studies. The comparisons and evaluations with the code of Engineering Equation Solver (EES) developed by NREL, the authors reported that the novel model found better in the prediction of the accuracy of thermal performance.

Zou et al. [46], represented the optical performance of PTCs under zero incident angles conditions. Effect of geometrical parameters like focal length, absorber diameter and aperture width on the optical performance of the PTC was studied. Monte Carlo Ray Tracing Method (MCRT) on the AZTRAK rotating test platform at Sandia National Laboratory (SNL) was used for a study on the SEGS LS-2 PTC module. They results showed that the maximum of local concentration usually increases with an increase of aperture width.

B.H. Upadhyay et al. [47], studied a PTC with a flexible, compact and novel design in order to test various parameters like different receiver materials, different reflective materials, different receiver diameters, various HTFs, different focal length, width and apertures length.

B. Agagna et al. [48], reported experimental and numerical study on a proto-type parabolic trough power plant, named MicroSolR. They conducted preliminary tests in order to evaluate the optical and thermal performance of PTC.

The aperture width of most actual collectors amounts to approximately 6m, the focal length is approximately 1.75m (correspondingly to the rim angle and aperture width values), and the module length is between 12 and 14m. There are some collectors that have smaller (Solarlite) or larger aperture widths (Skyfuel, Heliotrough) with corresponding different focal lengths [49].

1.2.2.1.2 Heat Transfer Fluid

The heat transfer fluid (HTF) is the fluid circulating between the solar field cycle and the power block cycle. It is used to transfer the thermal energy received by solar receiver to the storage block or power block. The type of HTF defines the operational temperature range of the solar field and consequently can enhance the efficiency of the PTC [40,50].

The operational temperatures are limited by the freezing and decomposition temperature of the medium. The maximum theoretical efficiency of the power cycle can be described by equation (8) with the Carnot-efficiency formula.

$$\eta_{Carnot} = 1 - \frac{T_L}{T_H} \tag{8}$$

Where the T_L and T_H are the lowest and highest temperature of the thermodynamic cycle, respectively. Therefore, when the highest temperature of the thermodynamic cycle rises, a higher heat to work energy conversion can be reached. Therefore, thermal stability for a HTF is an important principle that should be fulfilled. Other requirements on HTFs are listed in Table 3 [41].

Table 3. Heat transfer fluid requirements [41].

HTF Requirement	Motive
High eveporation temperature	The HTF must be liquid and operated under manageable pressure. The HTF cannot evaporate at the high temperatures in the solar field
Low freezing temperature	No freezing protection measures are necessary, if temperatures in the solar field drop.
Thermal stability	The HTF needs to withstand operation temperatures and avoid thermal cracking. Operating temperatures are constrained to this requirement.
High heat capacity	To favor the storage and transportation of high amounts of thermal energy
Low viscosity	Reduces important pumping energy
Low investment cost & Availability	Cost savings of the final LCOE and of logistic efforts
Environmental compatibility	Common responsibility
Low inflammability	Reduction of operational fire hazards

In HTF selection procedure, some criteria are more significant than others depends on the system configuration and general properties. For instance in solar systems with thermal storage, it could be an advantage to use the HTF also as storage medium due to the no requirement for additional heat transfer step between HTF and storage medium and priority of economic criteria in comparison to the other factors as a result of the requirement for large quantities of the HTF [41].

In addition, thermal stability and evaporation temperature are significant factor since they determine the maximum steam cycle temperature, which on its part determines the power block efficiency. In contrast, low inflammability is not always considered a significant selection criterion [41].

Pressurized water and synthetic oil are commonly used as a heat transfer fluid for low and medium temperature (100- 250°C) applications. Table 4 illustrates some important properties of some possible HTFs [41].

Table 4. Important properties of some possible HTFs [41].

HTF Medium	Maximum Temperature [°C]	Heat Capacity [J/kg/K]	Heat Conductivity [W/m/K]	Cost Estimation
Mineral oil	300	2600	0.12	Low
Synthetic oil	400	2300	0.11	High
Silicon oil	400	2100	0.1	High
Nitride salt	450	1500	0.5	Moderate
Nitrate sallt	565	1600	0.5	Low
Carbonate salt	850	1800	2.0	High
Sodium (liquid)	850	1300	71.0	Moderate

First power plants at Solar Electric Generating Systems (SEGS) in California, which started operation in 1985 used mineral oil as HTF in the solar field and also as storage fluid. However, due to the high flammability and operation temperature (at temperatures above 300°C mineral oil gets unstable) of this medium, it was substituted by synthetic oil (thermo oil) enabling a higher thermal stability [41].

Synthetic thermo oils are a eutectic mixture of biphenyl ($C_{12}H_{10}$) and diphenyl-oxide ($C_{12}H_{10}O$) and they are the most frequented HTFs with over 25 years of experience. In addition, they are available in large amounts and almost all parabolic trough power plants use synthetic thermo oil as HTF. This medium satisfy the majority of the aspects listed in Table 4 starting with a high heat capacity and maximal operating temperatures at 400°C and a low freezing temperature at about 12°C. However, the cost of synthetic thermo oils are high. They are not environmentally friendly like other possible media and deficient in flammability. Existing synthetic oils remain under study to improve the thermal stability at higher temperatures and for more affordable prices [41].

The application of molten salts as HTF is still under study and Archimede Solar Energy (ASE) company from Italy is pioneer in this field [51,52]. In this medium the salt mixtures are heated up to their liquid temperature. Molten salts as HTS can increase the output temperature of the solar field up to 450-550°C, which allows a higher Rankine cycle efficiency than in thermos oil systems. Aside of being accessible and available (due to the lower price than thermos oils), molten salts have high density, high thermal stability, good thermal/electric conductivity, non-toxic, non-flammable and relative low viscosity. A long-term concept of using molten salts as a HTF has been demonstrated on a 5 MW_{el} solar plant by Archimede Solar Energy (ASE) at Priolo Gargallo, Sicily [41]. However, due to their high freezing point further large commercial power plant has not been developed up to date. For binary molten salt mixture (two-part mixture of some substance) and ternary mixture (three-part mixture of some substance) the freezing point are 120°C and 220°C, respectively [41,53].

Now a day's researchers are working on different HTF like nano-fluid particles and molten salt to enhance the efficiency of the PTC [40]. F. Zaversky et al. [54], studied the transient modelling of PTC with molten salt as an HTF replacing the conventional thermal oil by 'Open Modelica'. The maximum temperature achieved was 520°C, and the average minimum temperature was 352°C.

The transient model was validated by data obtained by 'SOLTERM' facility located in Casaccia, Rome, Italy.

A.K. Hussein [55], published a detailed review of recent developments with the application of nanotechnology in different kinds of solar collectors. Al_2O_3/synthetic oil, SiO_2-H_2O, multi-walled carbon nanotubes (MWCNT)/ mineral oil nanofluid and gas-based nanofluids are listed. By using MWCNT/ mineral oil nanofluid instead of pure oil the efficiency of a parabolic trough collector enhanced by up to 5%.

Wang et al. [56], studied the performance of the PTCs using nanofluid as HTF and a three-dimensional optic-thermal-stress coupling model was carried out. The performances study on the PTC system with nonuniform heat flux distributions using Al_2O_3/synthetic oil as HTF showed that the deflection of receiver decreases from 2.11 to 0.54 mm and the volume fraction rises from 0 to 0.05. S.E. Ghasemi and A. Ranjbar [57], studied the numerical simulation of forced convection heat transfer flow in the receiver with various nanofluid as HTF. Results revealed that by adding CuO nanoparticles (3%) and Al_2O_3 nanoparticles to water, the heat transfer in increases by 35 and 28%, respectively.

E. Bellos et al. [58], examined seven working mediums energetically and exergetically in a commercial PTC. Water, therminol VP-1, molten salt, sodium liquid, air, carbon dioxide and helium are studied as working fluids. Their results showed that pressurized water is the optimum solution for moderate temperatures while Helium and carbon dioxide are better solutions for higher temperatures. E. Bellos published another study in 2019 and investigated six different nanoparticles including Cu, CuO, Fe_2O_3, TiO_2, Al_2O_3 and SiO_2 dispersed in thermal oil (Syltherm 800). Effect of varying concentration ratio, solar intensity and flow rate were studied using Engineering Equation Solver (EES). Cu concentrations of 6% were reported to give a maximum thermal efficiency of 0.74% [59].

1.2.2.1.3 Reflector (Mirror Material)

The mirror composition and its reflective material are key elements for the optical performance of a parabolic trough. Over 90% of the incident solar radiation (sunlight) has to be concentrated on the absorber tube in solar application. Which requires high geometrical precision and have a very high specular reflection of the solar spectrum by the mirror. In order to achieve these specific properties, a highly reflective material with a very smooth mirror surface such as silver or aluminum is required. Reflector materials should have a reasonable manufacturing and maintenance cost in addition to the long time durability in concerning resistance against UV-radiation, abrasion, soiling and breakage [60].

Figure 17 shows schematic of reflection and definitions for reflectivity characterization. The optical reflectance (ρ) of a surface is a parameter, indicating the amount of incident solar irradiation that is reflected by this surface. They are two extreme types of reflection according to physical law: the diffuse scattering reflection in the whole hemisphere (ρ_{hem}) and the specular reflection (ρ_{spec}). The specular reflection obeys the law of reflection, according to which the incident angle (ε_i) equals the reflected angle (ε_r) of the light beam [60]. In CSP applications, only specular reflectivity is of interest, because the reflected radiation must have a defined direction [41]. A perfectly smooth mirror will collect all reflected light inside ρ_{spec} which therefore shows the same value as ρ_{hem} and produces a gloss of 1, when gloss is defined as the ratio of ρ_{spec} to ρ_{hem}. However, an irregular surface quality or microstructures in the surface of the mirror, results in a broadening

of the specular reflected beam profile by an angle defined as the offset half angle σ_{spec}. A certain range of tolerance is defined for this parameter. It is measured of with specular reflectometers, which allows an angle of acceptance at 25 mrad [60].

In general, the reflectivity varies depending on the wavelength. It has to be specified for a given wavelength or a given wavelength range [41]. For CSP applications, the parameter values are therefore weighted with the solar spectrum, which result in the Solar Weighted Hemispherical reflectance (ρ_{SWH}) and the Solar Weighted Direct reflectance (ρ_{SWD}). ρ_{SWD} indicates the expected amount of sunlight that can hit the absorber [60].

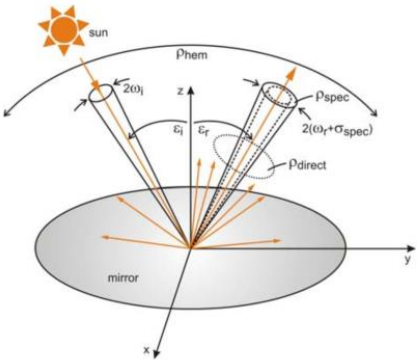

Figure 17. Schematic of direct and diffuse reflection on a mirror surface [60].

Table 5 indicates a summary of commercially available reflector materials for PTC. Back-silvered (silver coated) thick glass mirror is the first and most common parabolic mirrors today. The thickness of the complete mirror amounts to 4 to 5 mm. The mirrors have a multilayered structure. Manufacturing processes have been improved and industrialized over the last 30 years due to the increasing number of solar fields. As a result, their specific price per square meter has dropped up to 44%. In addition, measurement and practical experience have shown the high durability of silvered glass mirror reflectors compared to alternative materials [41].

Thin glass reflector derives from the optimization of thick glass mirrors and have showed good durability, excellent optical qualities, lighter weight and cost reduction potential. The material offers a higher degree of flexibility, but it also remains a sensitive material towards breakage and therefore requires a rigid structural surface onto which it can be embedded [61,62].

Alanod developed a front surface aluminized reflector based on an aluminum substrate, commonly applying high-purity aluminum as the reflective layer followed by a protective top coat. Aluminum reflectors are lighter and economical alternative to silver coated reflectors. However, for large-scale CSP application the durability and performance, need to be improved [41,63].

Silver coated polymer film as reflector material for PTC has been developed by National Renewable Energy Laboratory (NREL). This polymeric film reflector called ReflecTech and have been tested since 2002 in the SEGS plants in California. ReflecTech is made of multiple polymer layers with a reflective silver layer and can be applied to any smooth non-porous material by rolling on it [41,64].

Researches are being made to find alternative materials having a lower cost and good reflective properties. A.V. Arasu et al. [42], developed a smooth 90°rim angle fiberglass reinforced parabola trough for PTC. Instead of curved mirror, a flexible solar reflector material with a reflectance of 0.974 (SOLARFLEX foil) from Clear Dome Solar was used as a reflector.

A.A. Sagade et al. [65], studied the prototype line-focusing parabolic trough developed by composite material (fiberglass reinforced plastic). Aperture area of the collector was coated by aluminum foil with a reflectivity of 0.86. Mild steel receiver coated with black proxy material has been tested and the efficiency of 51% has been noted with glass cover. In another study by A.A. Sagade et al. [66], PTC made of mild steel and its surface coated with a aluminum foil of thickness 10 micron as a reflective surface. By using silver chrome selective coating and copper receiver, outlet temperature of 81.70°C was reported.

Table 5. Summary of current reflector materials for PTC.

<table>
<tr><th colspan="2">Thick Glass (thickness 4-5mm) [41]</th><th colspan="2">Thin glass (thickness 1-2mm) [67]</th></tr>
<tr><td colspan="2"> 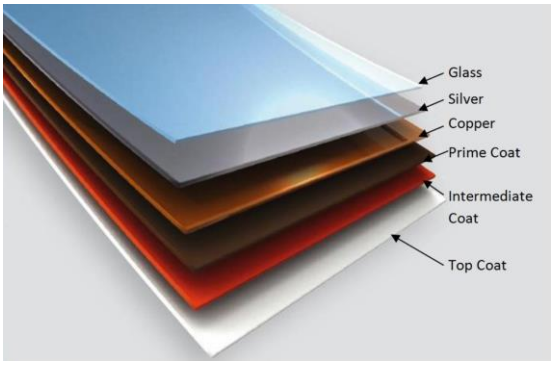
</td><td colspan="2"> 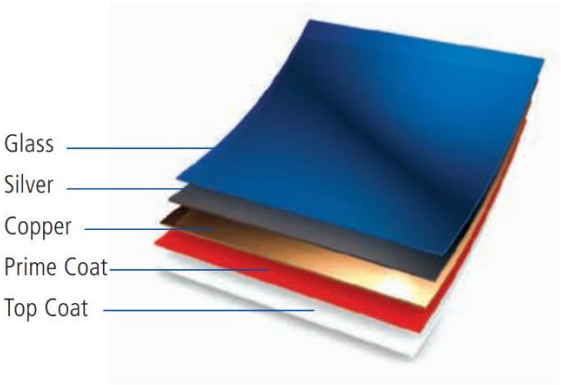
</td></tr>
<tr><td>ρ_{SWH}
ρ_{SWD}
Durability</td><td>93.5%
95.5%
Very good</td><td>ρ_{SWH}
ρ_{SWD}
Durability</td><td>93.0-96.0%
96.0%
Very good</td></tr>
<tr><td colspan="2">Disadvantage:
Breakage. Cost</td><td colspan="2">Disadvantage:
Breakage, Handling</td></tr>
<tr><th colspan="2">Aluminized reflector [41]</th><th colspan="2">Polymeric film reflector [41]</th></tr>
<tr><td colspan="2"> 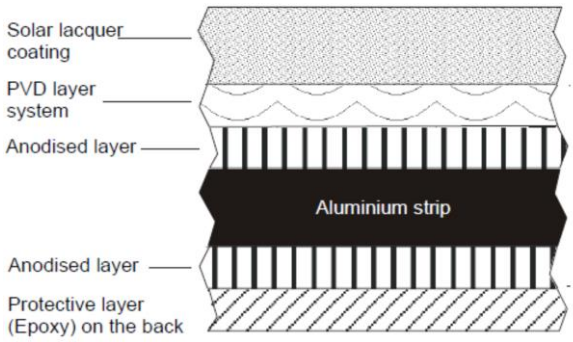
</td><td colspan="2">  </td></tr>
<tr><td>ρ_{SWH}
ρ_{SWD}
Durability</td><td>86.0-90.0%
79.0-92.3%
To be improved</td><td>ρ_{SWH}
ρ_{SWD}
Durability</td><td>92.5-94.0%
87.4-95.0%
To be improved</td></tr>
<tr><td colspan="2">Disadvantage:
Hemispherical and direct reflectance</td><td colspan="2">Disadvantage:
Direct reflectance</td></tr>
</table>

1.2.2.1.4 Receiver

Receivers have the task to convert the incident radiation into useful thermal energy and transports it to the tube. Figure 18, shows Schott PTR 70 receiver tube developed by German Schott Solar. The receiver material should have high absorptance (radiation absorption) and low heat losses. A constructive challenge is the heat expansion of the in temperatures between non-operating and operating conditions [40].

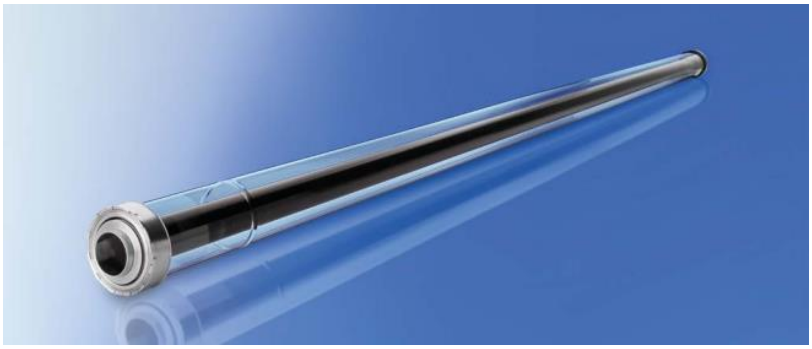

Figure 18. Schott PTR 70 receiver tube[68].

Several physical and geometrical factors are required for the receiver. Related to the geometric constraints, the reflected radiation has to hit the absorber surface. In addition, the radiation has to be converted as completely as possible into heat and the optical and thermal losses at the surfaces of the receiver components should be as small as possible. Coating and thermal insulation are applied to minimize thermal loss and optical loss at the surface of the absorber [41].

The main requirements for receivers are high absorption of the light and low thermal losses (low radiative losses as well as low convective and conductive losses). In order to achieve this, specific treatments are essential for the single elements of receiver. Typically, the receiver components are absorber tube, the evacuated glass tube and a group of further specific constructive elements (such as bellows for thermal expansion, glass-to-metal joints and getter) [41]. Figure 19 shows, components of a receiver tube at the example of a Siemens UVAC 2010 receiver.

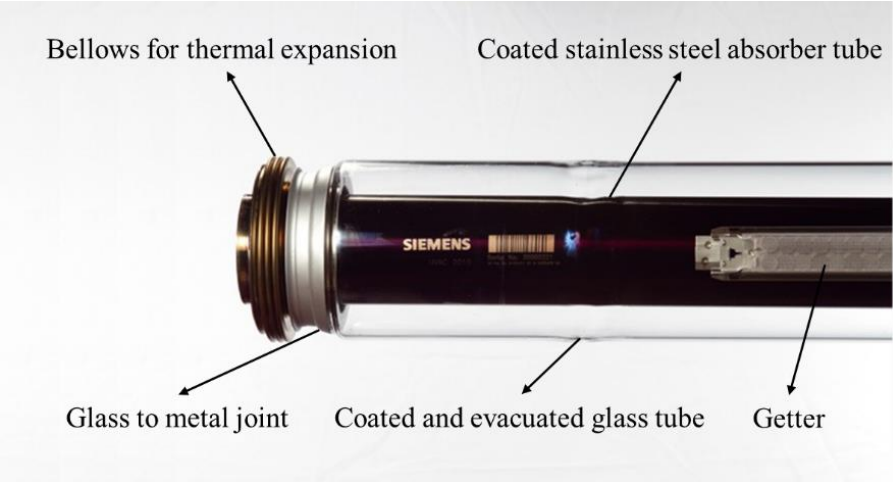

Figure 19. Components of parabolic trough receiver [69].

1.2.2.1.4.1 Evacuated and Non-evacuated receiver tube

In the early years, during the development of PTC technology, plain tubes were used as receivers. Since plain tubes are directly exposed to the ambient, large amount of concentrated heat is lost by convection. Hence PTC with plain receiver had very less thermal efficiency. With the advancement of solar thermal technologies, evacuated receivers were developed which improves the thermal efficiency of the system.

The typical PTC receiver tube is in fact composed of two concentric pipes, an inner steel pipe containing the working fluid and an outer glass tube surrounding the steel pipe. The glass tube is usually provided with an anti-reflective coating to achieve a higher solar transmittance and better annual performance. The glass tube is made of low-iron borosilicate glass to increase its transmittance for solar radiation. The outer surface of the steel pipe has an optically selective surface with a high solar absorptance and low emittance for thermally generated infra-red radiation [70,71].

Receivers for parabolic-trough collectors can be classified as either evacuated or non-evacuated. Evacuated receivers are commonly used for temperatures above 300°C because they have a high vacuum (i.e., 10^{-5} mbar) between the steel pipe and the glass cover, thus reducing thermal losses and increasing the overall efficiency of the PTC, especially at higher operating temperatures [71].

A PTC was tested with two separate evacuated receivers of different diameters by Li et al. [72] to determine thermal efficiency and temperature variation with time and solar insolation for water and N2 gas. The thermal efficiency of PTC was observed to be in the range of 68.4–76% for water when flow rate was increased from 0.0046 kg/s to 0.0342 kg/s in both the tubes.

In other case, N_2 gas as HTF, the thermal efficiency drops from 40.2–28% for the flow rate of 0.0024 kg/s to 0.0012 kg/s under the temperature range of 320-463 °C. Also, the fluid behavior in the evacuated receiver was further numerically analyzed with varying solar irradiation and aperture area. This study is useful for further research on PTC with thermo-chemical energy storage of ammonia for continuous power generation [72].

Daniel et al. [73]have numerically studied the performance of vacuum shell, non-evacuated and evacuated receivers in a PTC by simulating a one-dimensional numerical model of the system using Matlab. The vacuum shell without a selective coating was found to perform better by 10% compared to the non-evacuated receiver with selective coating. However, the evacuated receiver with selective coating gave the best performance amongst all the configurations.

Kasaeian et al. [74] have designed and manufactured a standard pilot model of PTC in order to investigate different methods for enhancing its performance characteristics. The optical and thermal performance, and the transient heat transfer characteristics of the system was compared using receivers as follows, black painted vacuumed steel tube, bare copper tube with black chrome coating, glass enveloped non-evacuated copper tube with black chrome coating and vacuumed copper tube with black chrome coating. MWCNT/mineral oil based nanofluids with volume fraction of 0.2% and 0.3% was used for testing different receivers. The vacuumed receiver gave on an average 11% higher efficiency than bare tube due to the reduced convection and radiation losses. The maximum optical and thermal efficiencies of the system with vacuumed copper receiver was found to be 61% and 68% respectively due to high absorptivity of 0.98. In general, the global efficiency of PTC was enhanced by 4–5% for 0.2% concentration and 5–7% for 0.3% concentration of nanofluid compared to base fluid for the defined working conditions.

Figure 20 shows a typical evacuated receiver. The glass cover of these receivers is connected to the steel pipe by means of stainless-steel expansion bellows which not only compensate for the different thermal expansion of glass and steel when the receiver tube is working at nominal temperature, but also provide a tight annular gap between both tubes to make the vacuum. One end of these expansion bellows is directly welded to the outer surface of the steel pipe, while the other end is connected to the end of the glass cover by means of a glass-to-metal welding [71].

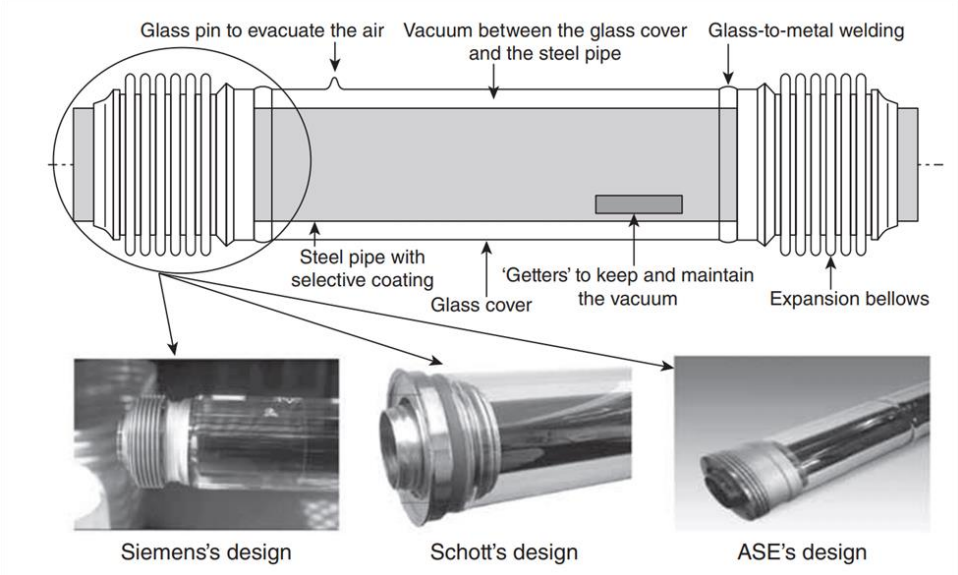

Figure 20. A typical evacuated receiver for parabolic trough collectors [71].

Shown in Figure 20 are chemical 'getters' placed in the gap between the steel receiver pipe and the glass cover to absorb gas molecules passing from the fluid to the annulus through the steel pipe wall. Since the evacuated receivers are expensive (about 850 €/unit in 2010) due to their technical complexity, they are used only for higher temperatures, when good thermal efficiency is required and the high cost is compensated by a higher thermal output [71].

At the end of 2010, there were only three manufacturers of evacuated PTC receivers: Schott, Siemens and ASE. Most of the parabolic-trough solar thermal power plants implemented around the world until 2009 had receivers manufactured by Solel (purchased in 2009 by Siemens, www.energy.siemens.com), or the German company, Schott (www.schottsolar.com). In 2009, a third manufacturer, the Italian company, Archimede Solar Energy (ASE, www.archimedesolaenergy.com), announced that they were launching a new receiver tube called HEMS08, suitable for fluids up to 550°C. The first plant using HEMS08 receivers was the Archimede Plant, located in Syracuse (Italy) and ready to operate in 2010 using molten salt (a mixture of sodium and potassium nitrate) as the receiver working fluid [68,71,75].

Figure 20 shows how these three manufacturers join the glass cover and the inner steel pipe by means of flexible bellows. The glass-to-metal welding used to connect the glass cover to the flexible bellows is a weak point in the receiver tube and has to be protected from the concentrated solar radiation to avoid high thermal and mechanical stress that could cause the welding to crack. An aluminum shield is therefore usually placed over the flexible bellows to protect the welding. Table 6 shows the technical parameters of the receivers manufactured by the Schott, Siemens and ASE companies [71].

Table 6. Technical parameters of the receivers commercialized by Schott, Siemens and ASE.

Parameter	Schott PTR-70	Siemens UVAC-2010	ASE HEMS08
Solar absorptance	≥ 0.95	≥ 0.96	≥ 0.95
Solar transmittance	≥ 0.96	≥ 0.96	n.a.
Thermal emittance	≤0.1 at 400°C	≤0.09 at 400°C	≤0.1 at 400°C
Steel pipe inner/outer diameters	70/65 mm	70/65 mm	70/65 mm
Thermal losses at 400°C	250 W/m	n.a.	230 W/m
Glass cover	Borosilicate	Borosilicate	Borosilicate
Active length ratio at 350°C	> 96%	96.4%	n.a.
Maximum fluid temperature	400°C	400°C	550°C

Non-evacuated receivers are suitable for applications with a working temperature below 300°C, because thermal losses are not so critical at these temperatures. Although non-evacuated receivers are also composed of an inner steel pipe and a glass cover, they have neither vacuum between the steel pipe and its glass cover nor glass-to-metal welds. Selective coatings used for non-evacuated receivers are simpler than those used for evacuated receivers. Black-chrome or black nickel coatings are commonly used because they are cheap and easy to produce. Due to manufacturing constraints, maximum receiver tube length is usually less than 5 m, so they are connected in series up to the total length of the PTC. Evacuated receivers are usually welded, while non-evacuated receivers are usually connected by special threaded joints [71].

During operation of solar thermal parabolic trough plants, using oil as HTF, the heat loss caused by hydrogen in the receiver vacuum is one major factor reducing the overall yield of the plant. The hydrogen originates from the cracking of the hydro carbon molecules at high temperatures (300°C – 400°C). The other products of the cracking process will be transported to the power block and could be extracted from HTF with different methods, but hydrogen will permeate into the annulus. Because hydrogen molecules are excellent heat conductors the heat loss will increase by the factor of 5 – 8, nearly eliminating the heat contribution of this receiver. Moderating the movements of hydrogen with a heavy mass noble gas (for instance Xenon) the heat loss can be reduced to a level 30% - 40% above the vacuum ($p < 10^{-3}$ mbar) [76].

In order to overcome this so-called ‘hot tube phenomenon’, SCHOTT introduced the premium receiver with a capsule containing noble gas placed in the evacuated annulus. The receiver operates after installation with the performance of the standard receiver (PTR 70), until the ‘hot tube phenomenon’ is detected. The encapsulated noble gas will be released via laser drilling the capsule, without further interruption of the plant operation. The opening process utilizes a fiber coupled laser and an alignment tool that is adapted to the conditions in the solar field. The drilling process is optimized for low impact on the receiver components and affordable equipment. Extensive tests confirm the sustained reliability of the receiver components after gas release. SCHOTT has developed a unique solution which is able to improve the receiver’s lifetime and performance significantly with low maintenance and low additional costs. This additional feature allows operation at high performance for a significantly longer period than the vacuum lifetime of the product, lowering the LCOE in that way [76].

In addition to the PTC, there are a number of different possibilities for developing flat-plate collectors that could be used in applications between 80°C and 120°C. In the first instance, it is necessary to reduce the thermal losses of the collectors without losing too much optical efficiency.

This can be achieved, for example, by using multiply glazed flat-plate collectors with antireflective glass, or using a hermetically sealed flat-plate design where the collector is filled with a noble gas, or by the development of evacuated flat-plate collector designs [77].

1.2.2.1.4.2 Absorber tube

In the visible light range absorptance of absorber tube must be high and its emissivity must be low in the infrared range to achieve high radiation absorption and a low radiative heat loss. Kirchhoff's law of thermal radiation refers to equality of the absorptance and the emissivity of a body for a specific spectral range ($\alpha_\lambda = \varepsilon_\lambda$). For different spectral ranges, absorptance and emissivity are different. In the case of absorber tubes, the absorptance α must be high for one spectral range, namely the solar spectral range ($0.25\ \mu m \leq \lambda \leq 2.5\ \mu m$), and its emittance ε must be low for another spectral range, namely the infrared range ($3\ \mu m \leq \lambda \leq 50\ \mu m$) to reduce thermal radiation losses [41]. Therefore, special coatings for absorber tubes have been developed and named selective coating, since optical behavior parameters on the surface can be selected (or manipulated).

Figure 21 shows the layer structure on an absorber surface. Selective coatings for the absorber tubes consist of different layers. The first layer is metallic and high reflective in the infrared range. It is typically made of Aluminum (Al), Copper (Cu) or Molybdenum (Mo). The following layer consists of a Cermet[1] material (such as Mo-Al_2O_3 or Mo-Si_2O). On top the antireflection ceramic layer consists of oxides like Al_2O_3 or Si_2O [41,78].

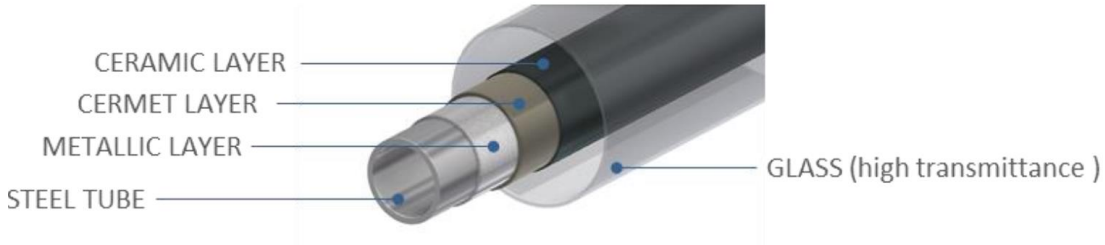

Figure 21. Multi-layer coating of the absorber tube.

Current receivers achieve absorptance values of the solar radiation between 0.95 (Schott, Archimede) - 0.96 (Siemens) and lower values of 0.09 (Siemens) -0.10 (Schott, Archimede) in emissivity of the thermal radiation at 400°C. These results correspond to receivers dimensioned for thermo-oils. In the case of molten salt receivers surface emissivity values of 0.10 can be attained at operational temperatures of 600°C. A selective coating is more difficult to design once temperatures rise, since there is a larger overlap between the thermal emission spectrum and the solar spectrum [41].

The intercept factor (γ) is the ratio of the reflected radiation to the reflected radiation hitting the absorber. Therefore, the diameter selection has an influence on γ and thermal losses of the system. A big diameter can increase γ , but it possesses at the same time a larger surface area. This would subsequently increase thermal losses at high temperatures. That is why smaller diameters have an advantage regarding thermal performance [41].

[1] Cermet: name derived from the materials composition ceramic and metal. Composed of a ceramic matrix and embedded metallic nano-particles.

The solar beam angle (α_D) is the opening angle of the direct solar radiation and it is equal to the 32° (due to the extension of the Sun disc it is not zero). By considering mirror imperfections that widen the beam beyond the solar beam angle by an additional dispersion angle (δ). The total beam spread after the reflection on the mirror is $\alpha_D + \delta$. The absorber diameter ($d_{absorber}$) can be described by equation (9) [41].

$$d_{absorber} = \frac{a \cdot sin\frac{\alpha_D + \delta}{2}}{sin\psi} \quad (9)$$

Where a is the aperture width and ψ is the rim angle. Absorber diameters vary between 70, 80 or 90 mm with a glass diameter of 115-125 mm. The new PTR 80 and PTR 90 have an absorber diameter of and respectively.

Many studies have been carried out on the receiver tubes. A. Valdés et al. [79] studied the angular distribution of temperature obtained from the water flow in order to evaluate the magnitude of deformation of the absorber of a direct steam generation unit. Distortion was found to occurs only for very low mass fluxes.

S. Khanna et al. [80], published a paper on PTC and an analytical expression is derived for checking the deflection in the central axis of absorber tube from the focal line of trough. For this study the dimensions of LS3 parabolic trough with Schott 2008 PTR70 receiver was taken and the results showed that the receiver tube would deflect during non-zero angles of incidence.

W. Fuqiang et al. [81], investigated the effects of a glass cover on heat flux distribution on the receiver tube by Monte Carlo Ray Tracing approach. For circular cross-section, numerical results showed that magnitude and distribution of heat flux are slightly affected when concentrated sunlight passes through the glass cover.

M. Bortolato et al. [82] studied a novel flat aluminum receiver for process generation in small linear concentrating collectors. They reported an optical efficiency of 82% and an overall thermal efficiency of 64% at 0.160 Km^2w^{-1} with negligible pressure drop.

L.S. Conrado et al. [83], published a review in order to study the main thermal aspects that need to be considered in future developments by review of experimental setups of PTC, thermal performance, numerical and simulation methods and different types of mathematical models.

C. Prahl et al. [84], presented a comprehensive review on the cause and effect of absorber tube misalignment for PTC and highest development in measurement techniques. They reported that to harness solar radiation with efficiency, proper mirror shape and receiver tube alignment is necessary and knowledge about the absorber tube position in different operation conditions is essential for prediction and optimization.

M. Potenza et al. [85], experimentally studied a novel high-temperature PTC with transparent receiver tube and gas phase nano-fluid as HTF (q mixture of CuO nano-powder and air). In their report two axes solar tracking PTC, with 4 m^2 reflecting surface was studied. Temperature range of greater than 145°C was controlled for 10 h and reached a maximum temperature of 180°C with a mean efficiency of 65%.

Gong et al. [86], introduced a new absorber tube using pin fin arrays inserted in the receiver tube of PTC to enhance overall heat transfer efficiency. In order to evaluate the flow characteristics and

heat transfer performance of the receiver, Monte Carlo Ray Tracing method coupled with the Finite Volume Method, was adopted. By using pin fin arrays the overall heat transfer factor can be increased to 12%.

M.T. Jamal-abad et al. [87], published an experimental study on a solar receiver filled with copper foam with a porosity of 0.9 and pore density of 30 PPI to enhance the heat transfer and raise the performance of PTC. Tests were performed in various volume flow rates and enhancement in performance was observed by increasing mass flow. However, they reported that the copper foam slightly improves the performance.

Y. Demagh et al. [88] proposed a numerical approach to analyze the heat flux density in a novel PTC S-curved tube receiver (conventional straight tube absorber was restored by a novel sinusoidal tube). Figure 22Shows a 3D schematic view of the novel S-curved tube receiver. This design could positively reduce both thermal stress and losses. The moderate Nusselt number[2] was raised to 45%–63%.

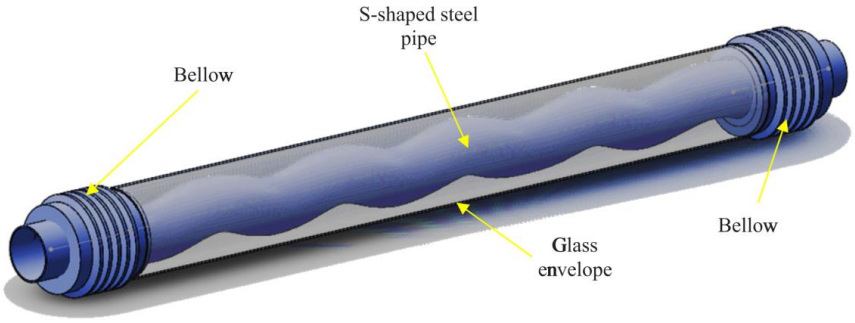

Figure 22. 3D schematic view of the novel S-curved tube receiver [88].

R.K. Donga et al. [89], studied concentration ratio of PTC using rhombus tube as a receiver. They developed an analytical method to determine the optimal size of a rhombus tube receiver for any PTC. They showed that For LS3 trough (without a change in intercept factor), the optimum size of the rhombus tube absorber is 13.8% smaller than the circular tube absorber. For the troughs with rim angle 90°, the maximum improvement in the concentration ratio was reported to be 31.5%. In addition, they reported that the rhombus tube absorber can be employed for various rim angles (70 to 90°).

1.2.2.1.4.3 Glass Tube

The receiver usually includes a tubular glass sheath transparent to the solar spectrum, useful to reduce convective (and also conductive) heat losses from the absorber to the environment. Moreover, the glass body is evacuated with different pressure level so that the convective and conductive heat loss is reduced further. The gas pressure level in Archimede and Schott receivers are less than 10^{-4} and 10^{-3} mbar, respectively. The glass tube usually made out of borosilicate glass due to their low coefficients of thermal expansion. The transmittance of the glass tube should be

[2] Nusselt number: The ratio of convective to conductive heat transfer at a boundary in a fluid.

at least 0.96 for the solar radiation and transmittance in the infrared range should be quite low. In order to obtain low reflectivity of the glass sheath a special antireflective coating is used. An antireflective coating increases the transmittance by 0.04 from 0.92 to 0.96 (reported by Archimede) [41].

1.2.2.1.4.4 Other components of the receiver

In order to control the thermal expansion due to the temperature changes of the absorber tube, bellows at the receiver ends are used to connect the absorber tube in a flexible way with the glass tube. To maintain the durability of the vacuum in the glass tube and reduce tension forces due to the temperature changes of the metallic elements and the glass tube at the receiver ends, a specific constructive consideration including matching of the thermal expansion coefficients of the glass near the compensator and the compensator itself have to be considered [41].

A getter is a deposit of reactive material that is placed inside a vacuum system, for the purpose of completing and maintaining the vacuum. Because of the cracking processes in the thermo oils the hydrogen can appears and traverse the absorber tube. Therefore, a getter is placed into the receiver to maintain the vacuum by absorbing the hydrogen in order to avoid the deterioration of the thermal insulation properties of the receiver due to the vacuum losses [41].

1.2.2.1.5 Tracking System

PTC is a line focusing concentrated device, so it needs a minimum one-axis tracking system like any other collector of a CSP system in order to obtain a continuous concentration of the direct solar radiation. The rotational axis is normally at the vertex line of the parabolic trough or in a parallel position slightly below it. North–south alignment with east–west tracking is preferred for general use while east-west alignment is generally used only for experiment purpose. Figure 23 presents the schematics of north–south alignment with east–west tracking [40,41].

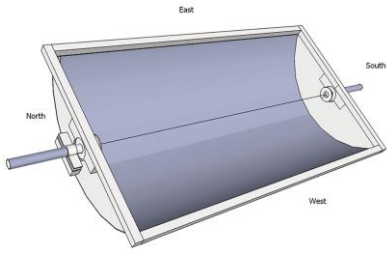

Figure 23. Schematics of north-south Alignment with east-west tracking [40].

Solar Zenith angle (θ_z) is the angle between the center of the Sun's disc and the line to the zenith. Solar azimuth angle (γ_s) defined as the angle between the projection of suns center onto the horizontal plane and due south direction [41,90]. Solar azimuth angle (γ_s) is defined as 0° at solar noon and increases thereafter, when the sun position goes toward west. Before noon towards east it is negative reaching 0° at solar noon as the day progresses [90,91]. Figure 24 illustrates the solar position viewed from a point *P* on the earth's surface in a local coordinate system [90]. Azimuth

angle (γ) indicates the orientation of the mirror aperture in relation to the horizon, where south=0° and west=90°.

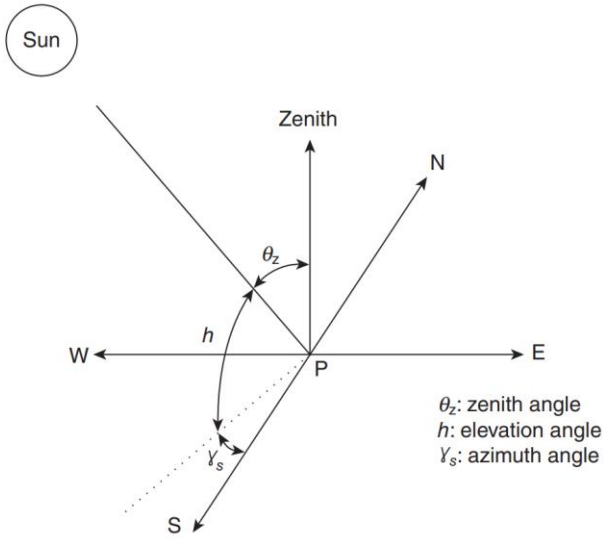

Figure 24. Representation of azimuth and zenith angles [90].

For north-south alignment, γ can have only two values equal to -90° or 90° when $\gamma_s<0°$ and $\gamma_s>0°$, respectively. In the other words, the mirror aperture is oriented to the east in the morning and to the west in the afternoon. For east-west alignment, γ can have only two values equal to 0° or 180° when $|\gamma_s|<90°$ and $|\gamma_s|>90°$, respectively. In the other words, the mirror aperture is oriented to the south if the Sun is south of the east-west line and to the north if the Sun is north of the east-west line [41]. Table 7, indicates the schematics of north-south and east-west alignments with related tracking angles (s).

Table 7. Tracking angles at parabolic trough systems.

North-South alignment	East-West alignment
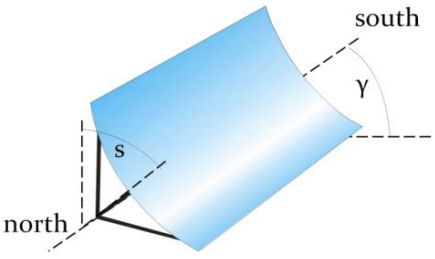	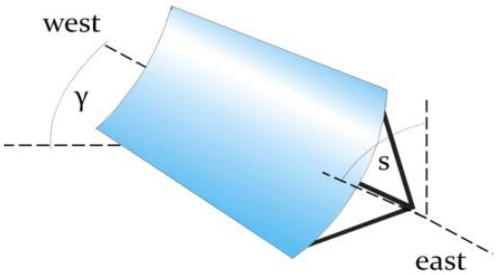
$\tan(s) = \tan\theta_z \lvert\cos(\gamma - \gamma_s)\rvert$	$\tan(s) = \tan\theta_z \lvert\cos(\gamma_s)\rvert$

The collector tracking movement is performed by a drive unit that moves a collector assembly mechanically or in electro-hydraulic way. In order to control the collector tracking it requires information about the Sun position, which can be provided by exact mathematical algorithm or sun positioning sensor [41]. Various researches have been carried out on the tracking system of PTC. Gama et al. [92] studied the design and realization of a new single axis sun tracking system with a portable receiver, in order to reduce the optical losses caused by the cosine effect in PTC.

For theoretical studies and simulations, they used TRNSYS software and their obtained experimental results are in a good agreement with those obtained by simulation.

D. Kumar et al. [93], Studied thermal performance of the solar PTC prototype with different mass flow rate and tracking systems. They used non-evacuated tube as a receiver in PTC with tracking system at east–west and without tracking system at south–north alignments. They showed that for small sized PTC the performance in system without tracking system at south–north alignments is higher.

W. Qu et al. [94], studied a solar PTC with rotatable axis tracking. During the summer the north–south axis tracking is adopted while in winter season due to the large solar incidence angle, the rotatable axis tracking permits more irradiation to be collected. By adopting a rotatable axis tracking, they enhances average collector efficiency by 5.0%.

G. Mageshwaran et al. [95], designed and tested a tracking system suitable for helical coiled receiver tube type PTC in order to increase the efficiency. Improved thermal stability and uniform circumferential temperature distribution can potentially be reached by helical coiled receiver tube design. However, this geometry decreases efficiency due to the drops in value of concentration ratio. Five different tracking modes were tested by authors and their results showed that north–south axis of rotation horizontally with the continuous adjustment is most effective and implemented design.

1.2.3 - Collector Efficiency

Figure 25 shows a general overview of the parameters that influence the collectors and therefore the solar fields' performance in form of Sankey diagram. In the solar field, optical and thermal losses occur in general.

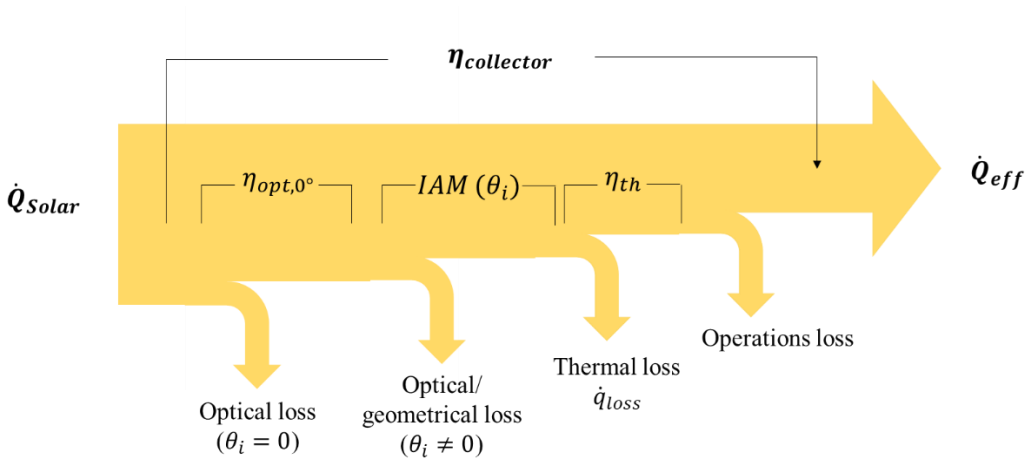

Figure 25. Calculation of the effective thermal energy in a PTC.

The effect of components of PTC regarding the collectors' performance is underlined in this section. PTC only use a fraction of the incident solar energy for heat production due to the energy losses during the solar-to-heat conversion ((10)).

$$\dot{Q}_{eff} = \dot{Q}_{solar} - \dot{Q}_{loss} \tag{10}$$

Where $\dot{Q}_{eff}$ is the effective thermal energy, $\dot{Q}_{solar}$ is concentrated solar energy and $\dot{Q}_{loss}$ thermal losses [96–98].

Equation (11) shows the collector efficiency as the ratio between the gained to the effective thermal power, derived from the general efficiency equation of collectors (equation ((12)).

$$\eta_{coll} = \frac{\dot{Q}_{eff}}{A_{eff} \cdot DNI} \tag{11}$$

$$\eta_{coll} = \eta_{opt,0°} - c_1 \frac{(T_m - T_{amb})}{DNI} - c_2 \frac{(T_m - T_{amb})^2}{DNI} \tag{12}$$

Where η_{coll} is the collector efficiency, A_{eff} is effective aperture area [m^2], *DNI* is direct normal irradiance [W/m^2], $\eta_{opt,0°}$ is peak optical efficiency, c_1 is linear loss coefficient [W/m^{2}K], c_2 is quadratic loss coefficient [W/m^{2}K^2], T_m is average temperature [°C] and T_{amb} is ambient temperature [°C] [96–98].

In order to describe the effective values on collector efficiency, additional parameters have to be specified. Particularly parameters regarding receiver losses and optical losses, which are empirically estimated. Figure 26 shows an example of efficiency curve related to the LS-2 solar collector and its empirical parameter values. The graph shows that by assuming ideal operational losses (such as perfectly clean mirrors, no shades on the aperture and no end losses), the optical losses fraction remains theoretically constant. However, the efficiency of the collector significantly drops, mainly due to thermal losses as ΔT increases [99].

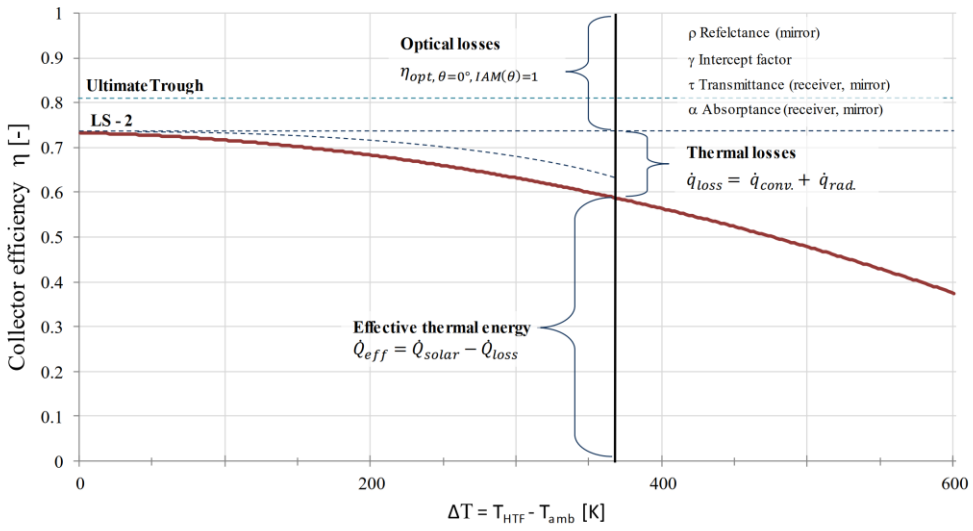

Figure 26. Collector efficiency curve at the example of an LS-2 collector with empirical parameter values and DNI= 800 W/m^2 [99].

For an incident angle of 0° (θ_i = 0°), the experimental thermal efficiency of the collector can be described by equation (13). It is defined as the ratio of useful power absorbed by the fluid that flows in the receiver and incident solar power on the area of the collector.

$$\eta_{th} = \frac{\dot{m} \cdot C_p \cdot (T_{out} - T_{in})}{A_{eff} \cdot DNI} \quad (13)$$

Where $\dot{m}$ is the mass flow rate and C_p is the specific heat capacity of HTF at medium temperature of the fluid [41].

1.2.3.1 Optical losses

Optical losses are caused, first, by geometrical inaccuracies such as macroscopic errors (slope and form) and microscopic errors (local roughness areas). Another group of geometrical errors are positioning errors caused by the position of the mirror and receiver. Tracking error also included in geometrical inaccuracies caused by collector torsion. Intercept factor (γ) is a measure of the reflected radiation that gets lost because it does not hit the absorber and all these errors cause the reduction of the intercept factor. For commercially available parabolic trough the intercept factor are between 0.96 and 0.97 and it is a result of an economic optimization and thermal loss consideration. Optical losses are caused, second, by the variance of the angle of the direct radiation incidence on the collector Optical losses are caused, third, by the limited reflectivity, absorptance or transmittance of the optical components due to their material properties and characteristics in addition to the their dependency on the soiling conditions. Finally, mutual shading of the collector rows also causes optical losses [41].

Direct sunlight or beam irradiance is the key resource for any concentrating solar system and its defined as a solar radiation that arrives on earth directly from the sun disc, without being scattered by the atmosphere. The fraction of the sun radiation that has undergone scattering processes through the atmosphere and so it has no defined directions is called diffuse irradiance. The sum of the beam irradiance and the diffuse solar irradiance is called global irradiance. To calculate the irradiance on a collector plane, direct, diffuse, and global irradiance must be calculated on a horizontal surface every short period. The amount of solar radiation received per unit area by a surface is called Direct Normal Irradiation (*DNI*) and it is always held perpendicular (or normal) to the rays that come in a straight line from the direction of the sun at its current position in the sky. If θ is, the incidence angle between the normal of the surface and the direction of sun rays. Global horizontal irradiance (G_H) can be defined by equation (14) where $G_{d,H}$ is diffuse horizontal irradiance [100].

$$G_H = DNI \cdot cos\theta + G_{d,H} \quad (14)$$

1.2.3.1.1 Peak optical efficiency

Optical losses occur even at optimal direct normal irradiance when the incidence angle (θ_i) is 0°. It means the sun is perpendicular with respect to the collecting surface. The losses affected by the optical properties of the mirrors and receivers including the absorptance (α) behavior, total specular reflectance (ρ_{total}), the transmittance (τ) of the glass materials and intercept factor (γ) of the collector-to-receiver light beam concentration which can causes optical deviations. Intercept factor is affected by qualitative inaccuracies of the mirrors. The maximal efficiency of the collector is constrained by peak (maximal) optical efficiency ($\eta_{opt,0°}$) and can be described by equation (15) [101].

$$\eta_{opt,0^\circ} = \alpha \cdot \rho_{total} \cdot \tau \cdot \gamma \quad (15)$$

In Figure 26 the peak optical efficiency for Ultimate Trough® (UT) collector in California and LS-2 collector are 0.82 and 0.73, respectively. Commercially available collectors for electricity production, have a peak optical efficiency of 78% to 82%. If ΔT= 0 K and no thermal losses are considered this value can be identify in a graphical representation of a collectors efficiency [99].

1.2.3.1.2 Incident angle modifier IAM(θ_i) and cosine losses cos(θ_i)

The ratio of the optical solar field efficiency at a given incidence angle ($\theta_i \neq 0$) to the optical solar field efficiency at $\theta_i = 0$ is called Incident Angle Modifier (IAM(θ_i)) and can be described by equation (16). It is the variance in output performance of a solar collector as the angle of the sun changes in relation to the surface of the collector. Since the sun position varies from east to west each day and the tracking angle over the seasons. For each specific collector measurements are used for correlations of the IAM [97].

$$IAM(\theta_i) = \frac{\eta_{SF,opt(\theta)}}{\eta_{SF,opt(\theta=0)}} \quad (16)$$

Figure 27 shows the optical parameters for an east-west alignment of parabolic trough with the tracking angle of $\rho \neq 0°$.

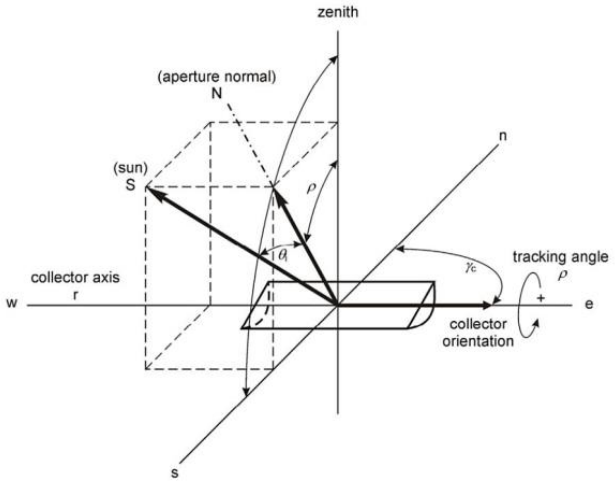

Figure 27. Representation of tracking case for an east-west oriented PTC [99].

When DNI on the aperture area is taken as the initial value of the power flow, cosine losses are also considered as an optical loss mechanism. For incident angles $\theta_i \neq 0°$ the radiation does not hit the aperture area with its maximal intensity, but it does with the DNI times the cosine of the incident angle (cos(θ_i)) [41].

The optical losses due to the losses of the reflected light beam at each collector end that do not hit the receivers due to the sun inclination called end effects ($\eta_{endloss}$). In addition, frequent cleaning of mirrors and receivers is very important therefore cleanliness factor (η_{clean}) describes the degree of cleanness of the mirrors and receivers. The optical losses caused by the shading of adjacent components on the aperture of the collector defined as shading (η_{shad}). The amount of solar energy that is concentrated onto the receivers is called concentrated solar energy and can be described by equation (25).

$$\dot{Q}_{solar} = A_{eff} \cdot DNI \cdot cos(\theta_i) \cdot \eta_{opt,0^\circ} \cdot IAM(\theta_i) \cdot \eta_{shad} \cdot \eta_{endloss} \cdot \eta_{clean} \quad (17)$$

Where A_{eff} is effective aperture area [m^2], *DNI* is direct normal irradiance [W/m^2], $cos(\theta_i)$ is the cosine losses, $\eta_{opt,0^\circ}$ is peak optical efficiency, $IAM(\theta_i)$ is incident angle modifier [102].

1.2.3.2 Thermal losses

Thermal losses occur in the absorber tubes and in the HTF pipes. These losses depend on the temperature difference between the heat transfer fluid and the surrounding. The thermal balance on a receiver is delimited by a glass envelope to the air and the heat losses from a warmer surface to the ambient occur because of convection heat transfer ($\dot{q}_{conv\rightarrow air}$) and to the sky by radiation ($\dot{q}_{rad\rightarrow sky}$). (equation (18)) [99,102].

$$\dot{q}_{loss} = \dot{q}_{conv\rightarrow air} + \dot{q}_{rad\rightarrow sky} \quad (18)$$

Convection heat transfer grows proportionally with ΔT and can be described by equation (19).

$$\dot{Q}_{conv} = h \cdot A \cdot \Delta T \quad (19)$$

Where *A* is the heat transfer surface area and *h* is the heat transfer coefficient which is not constant (depends on the wind conditions and on air humidity) and describes the heat transfer from the receivers and pipes to the surrounding air [99,102].

The radiative heat loss grows more than proportionally with ΔT (Figure 28). Due to the radiation losses that increment the losses to the forth power of the temperature difference value. The radiant emittance at the surface temperature of the considered heat transfer element (HTE) and the absorption of the thermal radiation at ambient temperature are considered as the radiation balance and can be described by equation (20).

$$\dot{Q}_{rad} = \alpha_{T_{amb}} \cdot \sigma \cdot A \cdot T_{amb}^4 - \varepsilon_{T_{HTE}} \cdot \sigma \cdot A \cdot T_{HTE}^4 \quad (20)$$

Where T_{amb} and T_{HTE} are the ambient air and the surface temperature of the considered heat transfer element (receiver or tube), respectively. α_T and ε_T are weighted average radiant absorptance and emissivity for the thermal radiation spectrum at the temperature *T*. σ is the Stefan-Boltzmann constant [41].

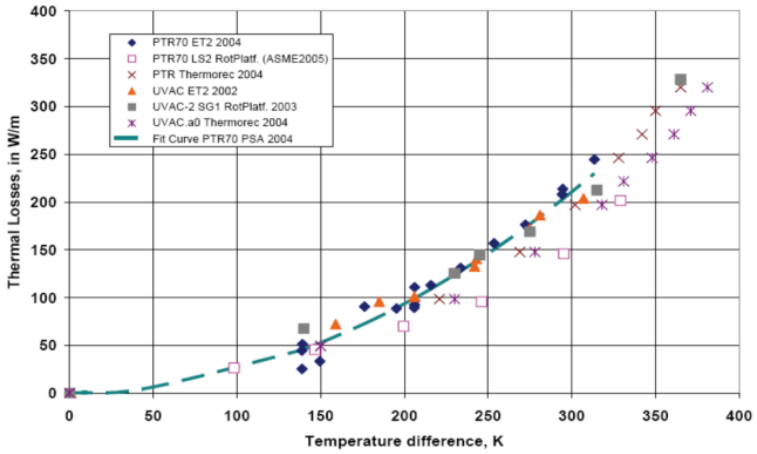

Figure 28. Heat loss measurements for different receiver types [41].

Generally, radiative heat loss dominates at high temperatures and convective heat loss dominates at low temperatures. Therefore, the mean heat loss mechanism at the absorber tube is thermal radiation and at the glass tube is convection. The convective heat loss is reduced by an evacuated glass tube that covers the absorber tube. In addition, the radiant heat loss from the absorber tube to the ambient air is reduced by means of a selective coating that reduces considerably the radiant emittance at common absorber operation temperatures (high absorptance for the solar spectrum and low emissivity for the thermal radiation at absorber operation temperature)[41].

In order to reduce the heat loss at the HTF transport pipes, a thermal insulation is used. Due to the small temperature difference between the pipe surface and the ambient air, radiation heat transfer plays a minor role. Therefore, the heat flows by conduction from the HTF to the outer surface and from there to the ambient air by convection. The conductive heat transfer grows proportionally with ΔT and can described by equation (21).

$$\dot{Q}_{cond} = \frac{\lambda}{b} \cdot A \cdot \Delta T \tag{21}$$

Where ΔT the temperature difference between the inner absorber tube surface (approximately the HTF temperature) and the outer tube surface. A, λ, b are the heat transfer surface area, the thermal conductivity of the insulation material and the insulation thickness, respectively [41]. Figure 29 shows a one dimensional receiver heat balance including convective, radiative and conductive transfers.

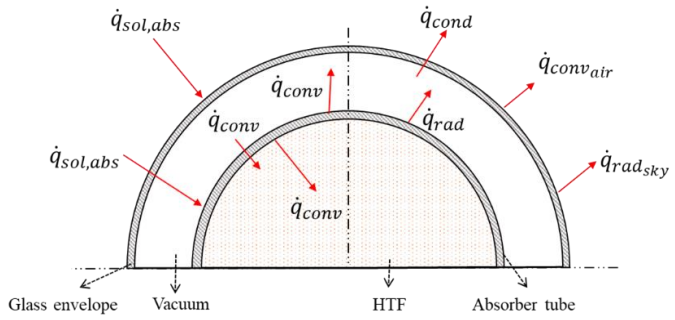

Figure 29. One-dimensional heat balance on a receiver cross-section.

1.2.3.3 Parasitic Energy Losses in Solar Field

Parasitic energy losses appear at the power plant level and constitute the required electrical power to operate the plant in operative or offline condition. This electrical power is mainly used by tracking drives of the collectors or the pumping of the heat transfer fluid trough the extensive collector rows or through the storage tanks. A fraction of the parasitic consumptions is also related to further electrical components, valves, ventilators and other similar components. About 2% of the input power or around 6-8% of the generated power is related to the parasitic energy consumption [41,102].

Figure 30 shows the energy flow in a parabolic trough power plant. The input power is the direct irradiance on the aperture. Solar field losses (optical and thermal losses) reduce the power by around 40%. More than the same power share gets lost in the power block, especially because of the heat rejection in the condenser. About 18% of the power input is transformed into electric power and about 16% is the useable electric output. This value indicates approximately the average overall efficiency of Andasol Solar Power Station I [41].

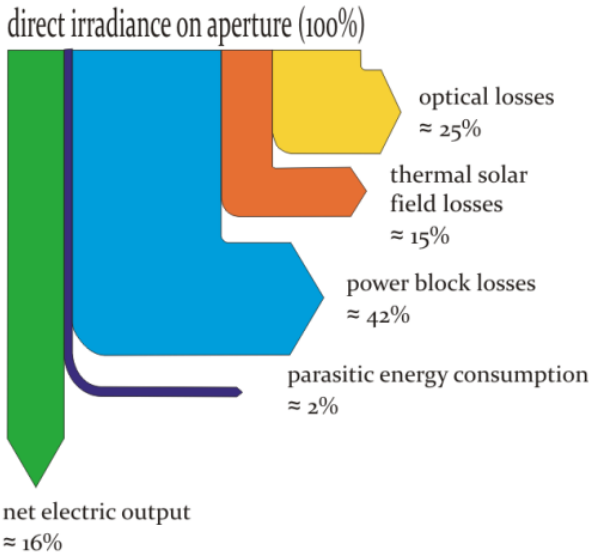

Figure 30. Estimated energetic flow in a parabolic trough power plan [41]

2 - Indoor Thermal Loss Test on Receiver

As yet, the majority of concentrating solar technologies had been limited to large installations in order to produce power [103]. For standard size receivers (absorber tube outer diameter of 70 mm) indoor test stands have been developed at several institutions with the aim of studying thermal loss. The evaluation of the heat loss can be performed in various modes such as steady-state equilibrium, quasi-steady-state equilibrium and surface temperature measurements [104].

Vernon E. et al. [105], published a comprehensive technical report on SEGS LS-2 solar collector efficiency and thermal losses. The tests were done as a function of the operating temperature for different selective coatings and vacuum level in the receiver annulus. . The absorber diameter of SEGS LS-2 receiver was 70 mm and the length was 4 m. The measurements were set up in off-sun mode, i.e. the collector was defocused and the receiver was shaded from direct sunlight. At 180°C above the ambient temperature, the thermal loss is around 13 W/m^2 with Cermet selective coating.

F. Burkholder et al. [106], from NREL fabricated a test stand to evaluate thermal loss of Solel UVAC2 and Schott PTR70 receivers in steady-state equilibrium condition. In this paper, three internal electric resistance heaters were used. Solel UVAC 2 and Schott PTR70 receivers showed a similar thermal loss value of 370 W/m at operating temperatures of 400°C. Another study from NREL on UVAC3 parabolic trough receiver was published as a technical report and UVAC3 parameters results were compared to UVAC2 results. The output values were 310 and 380 W/m at 400°C, respectively [107]. Two Schott's 2008 PTR70 parabolic trough receivers with 70 mm absorber diameter were also tested on NREL rig with three internal electric resistance heaters and heat loss correlation coefficients were derived from laboratory experiments. The heat loss value at an average absorber temperature of 320°C above ambient temperature was 140 W/m [108].

J. M. Márquez et al. [109], from PSA (Plataforma Solar de Almería), introduced a new test bench called HEATREC to study the receiver tubes in a chamber with vacuum and atmospheric pressure conditions. Eight internal electric resistances of ~6.3 Ω/m were used as heaters. The heat loss value at 360°C average absorber temperature above the ambient temperature for vacuum and atmospheric pressure condition inside the test chamber was 220 and 227 W/m, respectively.

S. Dreyer et al. [110] from DLR propose a test rig in order to investigate the behaviour of a receiver comparing the results with the heat loss predictions from optical measurements. For an absorber with an emissivity of 7%, 9.3% and 11.4% at 400°C, the heat loss values were about 189, 237 and 272 W/m, respectively. G. Hoste and N. Schuknecht from SkyFuel studied thermal efficiency of parabolic trough receiver for large-aperture collector, based on Joule effect heating in a steady-state condition [111]. J Pernpeintner et al. [112], studied systematic temperature deviations due to overheating by the cartridge heaters. This study presents the measurement of absorber temperature over- prediction as function of heating power and the results showed that absorber temperature over-prediction is at a relevant order of magnitude for heat loss measurements of parabolic trough receivers (with 70 mm absorber) . Also M. Sanchez et al. [113] from CENER reported a testing facility for the calculation of optical and thermal properties of receivers: the stand uses two electrical heating to reach the desired operating temperatures.

As mentioned before, all the cited studies are referred to standard receivers for parabolic trough collectors. Measurement methods and facilities need to be improved for smaller size receivers.

2.1 - Preliminary Indoor Test Stand Set-up

The receiver tube is a key component of parabolic trough collectors. The one considered in this study has a specific design, being formed by two coaxial tubes so that the fluid inlet and output are at the same side. It was properly developed to scale the PTC technology toward smaller size (chord length from 6-8 meters to around 0.5 m): the purpose is the installation in urban context and the application in industrial process. The outer absorber tube is made of steel and has a diameter of 10 mm (1 mm thickness) for a length of 1860 mm; the smaller coaxial tube is made of steel and has an internal diameter of 6 mm (0.5 mm thickness). Furthermore, a selective coating (Cermet coating, α=0.94 for λ<2.5 μm and ε=0.12 for λ>2.5 μm at ambient temperature) has been selected to reduce the emission in infrared range and increase the energy absorption in solar spectral range. The absorber tube is covered by a glass envelope with AR layer to prevent reflection of solar radiation by the glass surface. Inside, a vacuum level is fixed at 10^{-4} mbar to reduce the heat losses to the radiative ones. In order to keep the absorber tube aligned in the reflector focus, four springs support are inserted. A small cylinder of Kovar is used as a junction between metal and glass tubes (see Figure 31). This is to compensate the different thermal expansion coefficients of the two materials and to avoid the glass break. The steel outlet tube is then welded on a plug.

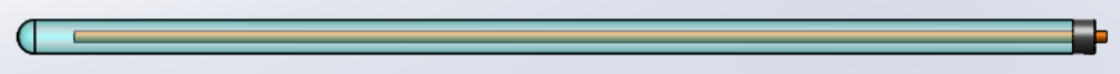

Figure 31. The scheme of the One-End receiver tube for m-PTC.

The thermal loss measurement is set up under indoor test without Sun irradiance, imposing a controlled internal heating. This process is based on the Joule effect, feeding electric heaters with current to obtain a steady state condition at different reference temperatures. A cartridge heater (Q_L) is inserted along the length of absorber tube (Figure 32). In order to increase the uniformity of temperature along the tube and to eliminate the axial temperature gradient, a second shorter cartridge heater (Q_S) is placed inside with a length of 250 mm from the outlet section of receiver tube.

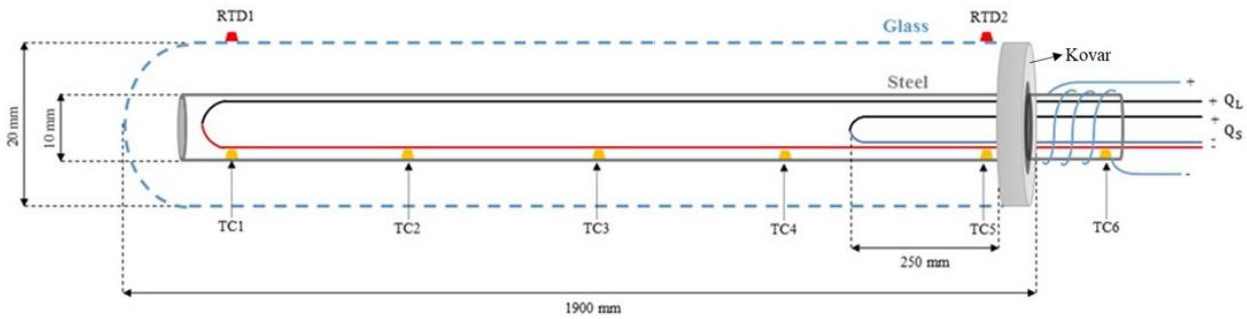

Figure 32. Scheme of the One-End receiver tube for m-PTC and the set-up layout.

An additional external heater (Figure 33) is placed before the Kovar part to meet the adiabatic condition, minimizing the temperature gradient between the portion of the metallic tube which is covered by glass and the one that stands in air. The cartridges are made of a nickel-chrome wire (electrical resistance of 5 Ω/m) covered by polymeric shield and they are fed with three different DC supplier up to 30 volts.

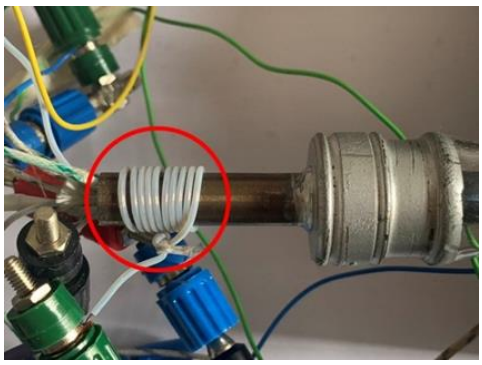

Figure 33. External heater.

Six thermocouples are used to measure the temperature along the absorber (Type T with accuracy of ±1 °C). TC1-TC5 are placed uniformly along the tube (fixed to the heater to slide inside the tube Figure 34a); TC6 is positioned outside to check the temperature gradient along the outlet section. Furthermore, the temperature of the glass envelope is evaluated by the placement of two 1/3 DIN class RTDs at the beginning and at the end of tube: Figure 34b shows their placement on glass. Another RTD monitors the ambient temperature. Figure 35 shows an overall schematic of the experimental apparatus.

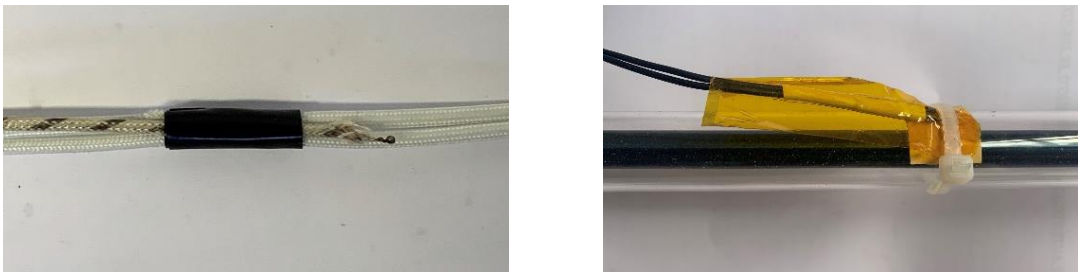

(a) (b)

Figure 34. (a) TC placement on the heater inside the absorber, (b) RTD placement on the glass tube of receiver.

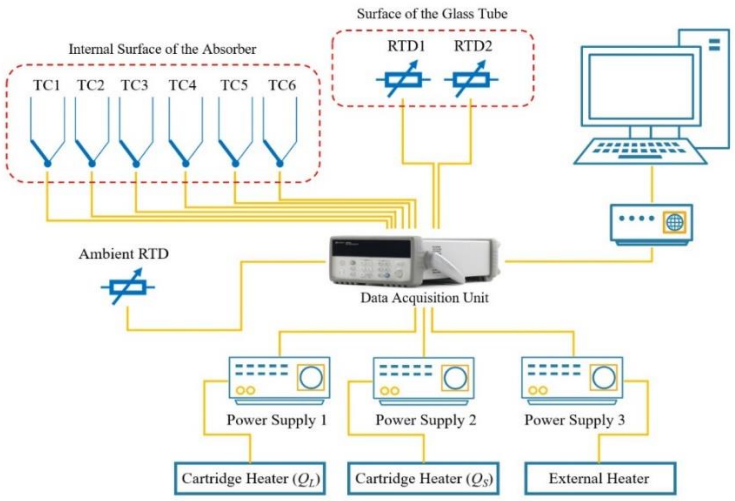

Figure 35. Schematic of the experimental apparatus.

2.1.1 - Procedure of Preliminary Indoor Test

Sensors are connected to the data acquisition unit and in this case Agilent 34970a has been used to reading and recording the values of TC1-TC6, RTD1, RTD2, RTDs related to ambient temperature and voltage of the heater. Furthermore Agilent 34401a digital multimeter has been used in order to record the direct current related to the heater (see Figure 36). Related errors caused by data acquisition units including measurement error, switching error, and transducer conversion error are reported in Table 8. The data acquisition unit has been programmed by with LabVIEW environment to manage all the acquisition and data recording process.

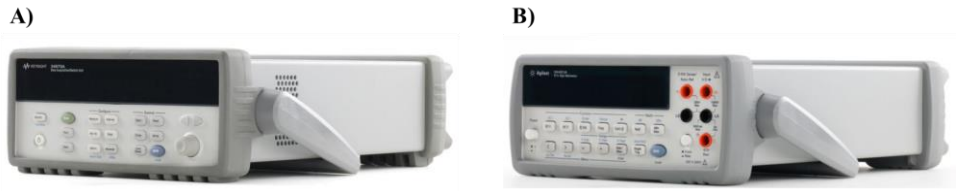

Figure 36. A) Agilent 34970a B) Agilent 34401a [114].

Table 8. Accuracy specifications for Agilent 34970a and 34401a [115].

Type	Parameter	Range	Accuracy specifications * ± (% of reading + % of range)
Agilent 34970a	DC voltage	100.0000 mV*	0.0050 + 0.0040
		1.000000 V*	0.0040 + 0.0007
		10.00000 V*	0.0035 + 0.0005
		100.0000 V*	0.0045 + 0.0006
		300.000 V*	0.0045 + 0.0030
	Thermocouple Type T	–100 to 400 °C	1.0 °C
	RTD	–200 to 600 °C	0.06 °C
Agilent 34401a	DC current	10.00000 mA*	0.050 + 0.020
		100.0000 mA*	0.050 + 0.005
		1.000000 A*	0.100 + 0.010
		3.00000 A*	0.120 + 0.020

A customized graphical user-interface (Figure 37) has been developed properly and used to real time monitoring sensors with the display of the main parameters such as voltage, current and power of heaters.

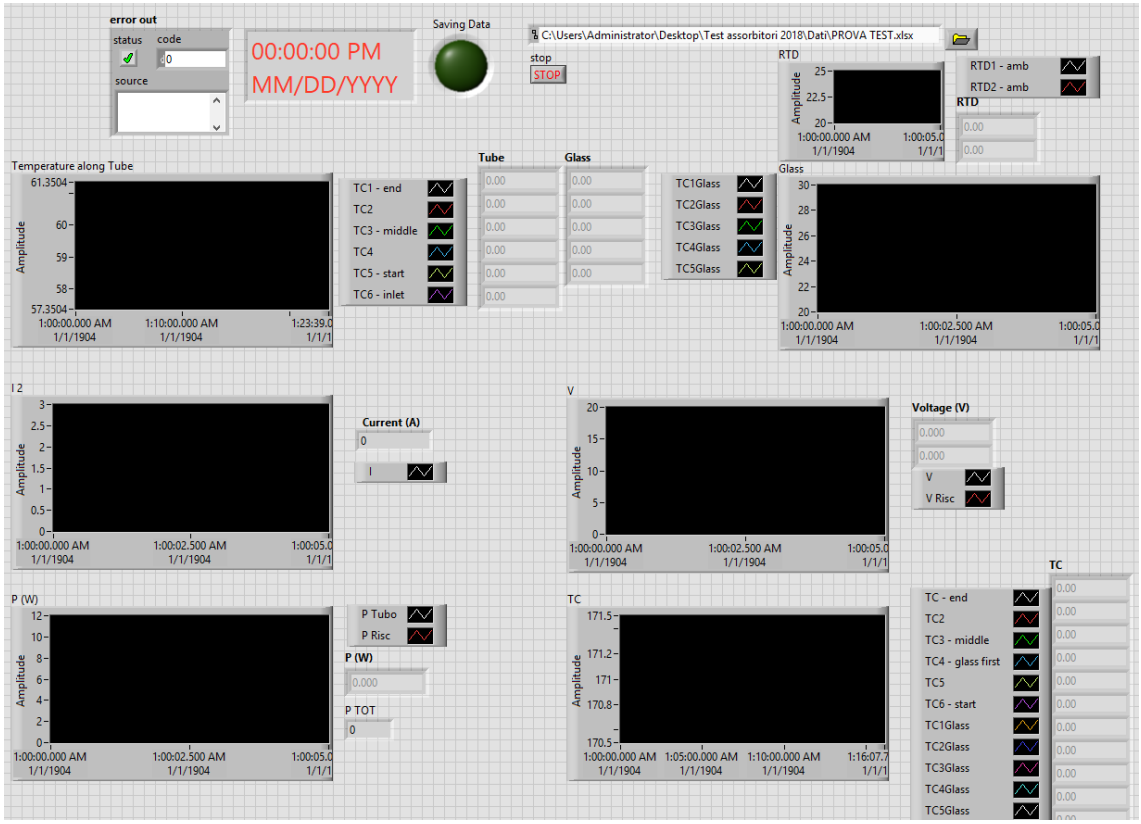

Figure 37. The graphical user-interface for monitoring test values developed in LabVIEW.

In order to achieve a desired uniform temperature along the receiver tube, some preliminary test should be conducted on the heating supplier parameters. However, the size of tube could not permit to check the precise position of sensors and the real surface contact among them, the heaters and the absorber tube.

Once the heating devices are placed in the test stand, electrical supply is increased step by step for all of them separately, until reaching steady-state condition at different temperature levels. This procedure is a slow process, taking also hours, in which every change causes an unbalancing of the temperature gradient along the tube. The input power P_{in} due to Joule effect is derived thanks to voltage (U) and current (I) for each heater with equation (22).

$$P_{in} = U \cdot I \text{ [W]} \tag{22}$$

The test procedure was repeated for 28 cases in the range of interest. For instance, in test 9, an average temperature of 88°C was reached along the tube and Figure 38 shows that the temperature stability was kept for over 20 minutes under the uncertainty of thermocouples. Furthermore, the maximum temperature difference is limited at 9°C with the exception of the final part of the receiver tube (TC1) which got colder than 23°C in respect to the higher value.

For the other tests, the equilibrium temperature increased with higher electrical power, finding similar behavior of the rig and the values in Table 9 at stable conditions. Table 10 shows temperature variation along the receiver tube among the 28 tests at stable conditions.

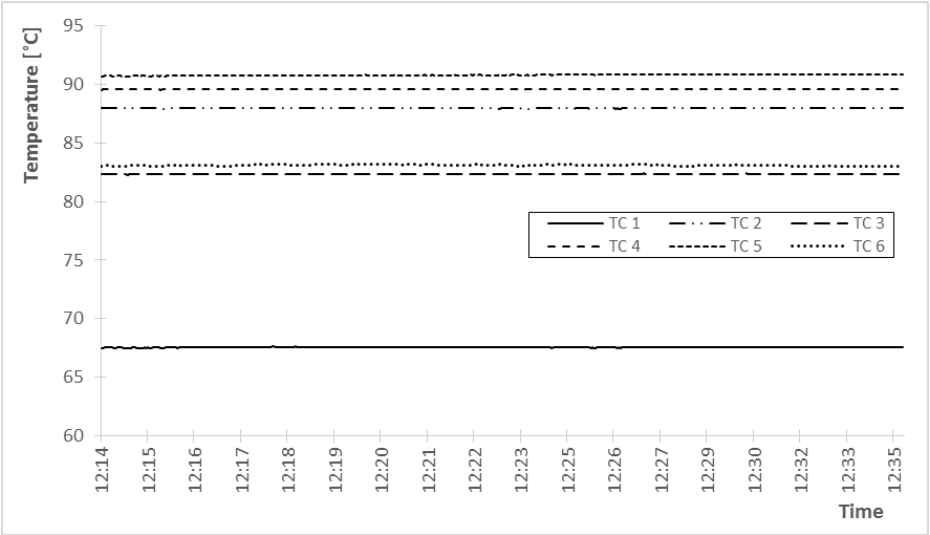

Figure 38. Temperature variation along the absorber tube in Test 9.

The overall evaluation and comparison of recorded data showed that TC1 values are never in match with the others. This is mainly attributable to a displacement of the thermocouple in the end of tube. The lack in the contact between Q_L heater and the tube is less probable: they have a similar diameter and the tolerance is small while inserting the heating device. In any case, it is not possible to verify the real internal configuration because there is no access in that side of the absorber. For these reasons, the authors decided to calculate and report heat loss for a reference average temperature T_{ave} excluding TC1 values. TC6 was also not taken into account since it is not under vacuum conditions (it is in contact with the outlet part of the tube beyond the Kovar cylinder.

Table 9. Main test parameters.

Test	Q_L Voltage (V)	Q_L Current (A)	Q_L Power (W)	Q_S Voltage (V)	Q_S Current (A)	Q_S Power (W)	Total Power (W)
1	2.755	0.126	0.346	0.489	0.154	0.076	0.422
2	2.884	0.131	0.379	0.456	0.144	0.066	0.445
3	4.275	0.195	0.832	0.445	0.139	0.062	0.894
4	4.275	0.195	0.832	0.439	0.137	0.060	0.893
5	6.949	0.316	2.195	0.600	0.187	0.112	2.307
6	6.949	0.316	2.195	0.600	0.187	0.112	2.307
7	8.125	0.369	2.998	0.671	0.209	0.140	3.139
8	8.123	0.369	2.997	0.671	0.209	0.140	3.138
9	10.452	0.476	4.977	1.693	0.592	1.001	5.978
10	10.419	0.473	4.927	1.148	0.356	0.414	5.340
11	10.418	0.473	4.925	1.255	0.390	0.489	5.414
12	11.191	0.526	5.887	1.790	0.292	0.523	6.409
13	13.510	0.612	8.262	1.258	0.390	0.491	8.753
14	13.510	0.611	8.261	1.259	0.390	0.491	8.752
15	14.236	0.644	9.167	1.216	0.377	0.459	9.626
16	14.236	0.644	9.169	1.214	0.377	0.458	9.627
17	14.835	0.674	9.999	2.185	0.759	1.659	11.658
18	15.776	0.713	11.252	1.219	0.376	0.458	11.710
19	17.180	0.776	13.331	1.509	0.465	0.701	14.032
20	17.180	0.776	13.329	1.508	0.464	0.700	14.029
21	19.825	0.894	17.720	2.065	0.633	1.308	19.030
22	19.825	0.894	17.718	2.045	0.628	1.284	19.002
23	20.228	0.912	18.444	2.369	0.728	1.725	20.170
24	20.229	0.912	18.439	2.365	0.727	1.718	20.158
25	21.033	0.948	19.939	1.985	0.611	1.213	21.151
26	21.019	0.947	19.905	1.996	0.614	1.226	21.132
27	21.509	0.969	20.834	2.220	0.681	1.513	22.347
28	21.847	0.985	21.529	2.870	0.936	2.686	24.215

Table 10. Temperature variation along the receiver tube during 28 tests.

Test	TC1 (°C)	TC2 (°C)	TC3 (°C)	TC4 (°C)	TC5 (°C)	TC6 (°C)	RTD 1 (°C)	RTD 2 (°C)	T_{amb} (°C)
1	32	33	32	33	34	33	20	23	21
2	31	32	32	33	34	32	20	23	21
3	34	41	39	40	41	40	20	23	21
4	35	40	39	40	41	40	20	23	20
5	48	60	57	61	60	59	20	24	19
6	48	59	57	60	60	59	20	24	19
7	52	67	64	67	67	66	20	24	19
8	53	67	64	68	67	66	20	24	19
9	68	88	82	90	91	83	20	20	18
10	68	88	82	88	91	82	22	25	21
11	68	88	83	89	91	83	22	25	21
12	83	108	105	107	105	106	22	22	21
13	86	116	106	117	117	116	24	31	21
14	86	116	106	117	117	116	24	32	21
15	88	122	111	122	120	120	25	32	21
16	88	122	111	123	121	120	25	34	21
17	94	128	115	129	128	128	24	24	19
18	96	136	122	136	130	130	26	34	21
19	105	147	131	148	144	144	27	37	21
20	105	147	148	148	144	144	28	37	21
21	119	169	148	170	169	168	29	31	21
22	119	169	148	170	170	168	29	36	21
23	123	171	151	173	174	173	29	31	21
24	123	171	151	173	174	171	29	31	21
25	125	177	155	179	169	169	30	30	21
26	125	177	155	179	169	168	30	31	21
27	125	182	158	183	182	182	31	41	21
28	128	183	159	185	192	166	28	28	19

It is also important to remark that test need a very long time (at least 5 hours for low power) to get stable conditions and a small increment/decrement in the power supply for one of the heater causes a non-negligible but slow change in the temperature distribution. In these operating settings, a maximum standard deviation of 14.3°C was accepted for the highest average temperature (test 28 at 180°C) while, for lower values such as 40, 59, 88, 106, 119, 143, 164 and 176°C it drops down to 0.8, 1.6, 3.7, 1.7, 5.5, 7.8, 10.7 and 12.2°C, respectively. A specific constraint was fixed as necessary condition: time intervals were chosen for processing data only when each temperature resulted constant with a variation inside sensor's accuracy (±1°C). The stable part of test lasted more than 1:30 h on average.

As mention before, the UF-RT01 was developed aiming at scaling solar concentrating technology towards small dimension to integrate them in urban context. Some considerations could arise in the comparison with receivers for standard PTC systems. In the market two tubes have been selected as a reference for UF-RT01 even the application is different such as working conditions and purpose (Schott and Archimede Solar Energy). In order to address the issue of space limitation in urban-industrial areas, UF-RT01 has been developed with much lower diameter (10 mm compared as 70 mm of the commercial absorbers [75,116]).

Table 11, indicates the design parameters of above-mentioned receiver tubes. The thermal loss of SCHOTT, Archimede and UF-RT01 receiver tubes at 130°C (difference between operating conditions and ambient temperature) are 5.75, 9.30 and 8.28 W/m, respectively. It should be noted that the comparison of systems with a temperature difference of 130°C - operating temperatures of 150-160°C - is intended precisely to refer to the most critical urban or industrial applications for the PTC technology competing with collectors without tracking with vacuum tubes such as CPCs.

By considering the mentioned receiver tubes in a solar system unit with a length of 1 m (in similarity with the other geometric dimensions), overall efficiency of 0.5, irradiation of 800 W/m2 and local concentration ratio of 13.1 (indicative value for small systems), the gross collected power is 1148 W for SCHOTT and Archimede, 164 W for UF-RT01. The proposed methodology is based on local concentration ratio (LCR) distribution obtained for a part of the SCHOTT and Archimede absorber perimeter since the number of ray intersections allows calculating the solar radiation flux superficial distribution and thus the local concentration ratio [117].

With modules in similarity at 130°C, almost eight meters UF-RT01 receiver are required to gain a comparable amount of power from one meter of the commercial tubes, including heat loss. In detail, 1142 W, 1139 W and 1246 W comes out from SCHOTT, Archimede and UF-RT01s, respectively. Practically, a hypothetical solar field that exploits UF-RT01 would have the same potential as current commercial ones: it is just a matter of making sure that the construction of the solar field (easier, with greater flexibility, increased modularity, etc.,) does not lead to higher costs.

For this purpose, it is important to note that a CR of 13.1 with commercial tube means a parabolic mirror of aperture 2.88 m which becomes 0.41 m for the UF-RT01. Consequently, it can be derived that if, with the same collecting radiation surface, the systems using SCHOTT solutions rise to almost the same input energy (1142 W vs. 1246 W) as the one using the UF-RT01s. In consideration of the fact that the cost of these small-size collectors, based on UF-RT01, are certainly lower (for instance, a major part of components could be prefabricated), the solar field would be significantly less expensive overall.

We can conclude that probably the direction aiming at trying to reduce the specific costs of thermal kWh by increasing the dimension of collectors should perhaps be revised. From what has been produced and experimentally detected, it is evident that the winning strategy should be instead reducing the size so much that a pushed high standardization would lead to a greater drop of specific cost such as it has happened for the photovoltaic technology of photovoltaic.

On the other hand,

Table 11 is reporting the reliable cost per meter of the different technologies. For the reference length of the systems the lower performance of UF-RT01s are compensated by a much lower specific cost per meter. Then, the UF-RT01 receiver layout results the 60% cheaper than commercial solutions at the same collected power.

Table 11. Design parameters of solar systems with UF-RT01 and two receiver tubes available in the market (Schott and Archimede Solar Energy).

Receiver	Diameter [mm]	Specific heat loss [W/m]	CR [-]	Gross Power [W]	Relative heat loss [%]	Net Power [W]	Specific Cost [€/m]
SCHOTT	70	5.7	13.1	1148	0.5%	1142	400
Archimede	70	9.3	13.1	1148	0.8%	1139	400
UF-RT01	10	8.3	13.1	164	5.0%	156	30

Receiver	Reference receiver's length [m]	Net Power [W]	Cost [€]
SCHOTT	1	1142	400
Archimede	1	1139	400
UF-RT01	8	1246	240

2.1.2 - Experimental Results of Preliminary Indoor Test

The measurement set-up lets to find the correlation between thermal loss and average temperature for a solar receiver in the range of interest (up to about 180°C). Since among 28 tests many of them are related to the same interval, the temperatures along the absorber tube during the campaign is summarised for 8 tests (Figure 39). Excluding TC1, the reference stable temperature is 40, 59, 88, 106, 119, 143, 164, 167, 176°C in ascending order. For each value, the supply power for heaters (Q_S and Q_L) were evaluated and the same amount of power is assumed to be dissipated to the external ambient mainly due to irradiation (vacuum between absorber and glass limits convection and conduction phenomena). Another contribution for heat transfer comes at the outlet portion of the tube where the steel-Kovar junction creates a thermal bridge. Then heat loss could be derived thanks to equation (23):

$$Q_{loss} = Q_L + Q_S - Q_{ad} = a_1 \Delta T^2 - a_2 \Delta \mathrm{T}\ [\mathrm{W}] \quad \textbf{(23)}$$

$$Q_{ad} = \frac{kA}{\Delta x}(\mathrm{TC5} - \mathrm{TC6})\ [\mathrm{W}] \quad \textbf{(24)}$$

Where Q_S and Q_L are the heaters power, k is the thermal conductivity of steel, A is the steel pipe cross-section area, TC5 and TC6 are temperature values and Δx is the distance between them. The parameters k, A and Δx are 13 W/(m°C), 28.27 mm^2 and 40 mm, respectively. Receiver thermal loss coefficients can be described by a_1 and a_2 where ΔT is the difference between average absorber temperature and ambient temperature.

Therefore, equation (24) represents the conductive dissipation (or contribute depending on the sign of the temperature difference) through the absorber section area at the tube outlet (Q_{ad}). Despite of the controlled heating device showed in Figure 38, the gradient between TC5 and TC6 was not zeroed during test.
In Figure 40 and Table 12, the evaluated heat loss power is reported as a function of the difference between average absorber temperature and ambient temperature (ΔT). A maximum value of 23.98 W is found when ΔT is 161°C (tube average temperature of 180°C). The fitting quadratic curve results equation (25):

$$Q_{loss} = 0.00078\Delta T^2 - 0.02291\Delta T\ [W] \quad \textbf{(25)}$$

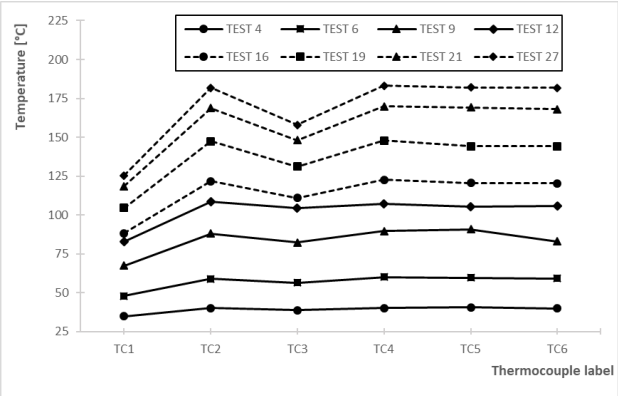

Figure 39. Temperatures distribution along the absorber tube during main tests.

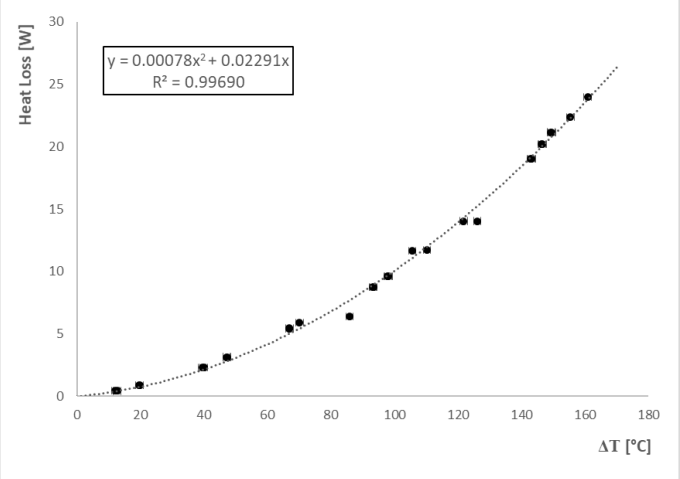

Figure 40. Heat loss as a function of the difference between the average absorber temperature and the ambient temperature

Table 12. Test values for temperatures and heat loss with errors.

Test	T_{ave} [°C]	ΔT [°C]	ΔT error [°C]	Q_{loss} [W]	Q_{loss} error [W]	Test	T_{ave} [°C]	ΔT [°C]	ΔT error [°C]	Q_{loss} [W]	Q_{loss} error [W]
1	33	12.7	0.8	0.4352	0.0009	15	119	97.9	0.8	9.6288	0.0007
2	33	12.1	0.8	0.4589	0.0002	16	119	98.1	0.8	9.6289	0.0007
3	40	19.6	0.8	0.9003	0.0003	17	125	105.6	0.8	11.6571	0.0012
4	40	19.8	0.8	0.90018	0.00011	18	131	110.3	0.8	11.7103	0.0009
5	59	40.0	0.8	2.3107	0.0002	19	143	121.8	0.8	14.0333	0.0009
6	59	39.5	0.8	2.3110	0.0002	20	147	126.1	0.8	14.0309	0.0009
7	66	47.1	0.8	3.1452	0.0003	21	164	143.1	0.8	19.039	0.002
8	66	47.3	0.8	3.1455	0.0003	22	164	143.2	0.8	19.0167	0.0013
9	88	70.1	0.8	5.9070	0.0007	23	167	146.7	0.8	20.1839	0.0013
10	88	66.9	0.8	5.424	0.007	24	167	146.5	0.8	20.1854	0.0014
11	88	67.0	0.8	5.4872	0.0004	25	170	149.4	0.8	21.154	0.004
12	106	85.9	0.8	6.415	0.019	26	170	149.6	0.8	21.142	0.013
13	114	93.2	0.8	8.7661	0.0006	27	176	155.5	0.8	22.3472	0.0015
14	114	93.5	0.8	8.7657	0.0007	28	180	160.9	0.8	23.978	0.004

Uncertainty is evaluated for all the measured values taking into account Type A errors for experimental data measurement and Type B errors for instrument characteristics and equipment uncertainty [118]. Combined standard uncertainty is used for error propagation in the derived parameters, based on the sum-of-the-squares method [119].

Two types of uncertainty are evaluated separately, in relation to an experimental and non-experimental data; Type A for repeated experimental measurement of a quantity and Type B for instrumental characteristics and equipment uncertainty, provided by calibration certificate. Equation **(26)** shows the Type A uncertainty ($u_A(x_i)$) for *n* repeated measurements under the same test conditions [118].

$$u_A(x_i) = \sqrt{\frac{\sum_{i=1}^{n}(x_i - \bar{x})}{\frac{n-1}{n}}} \quad \textbf{(26)}$$

Where x_i is the observed values of a sample item and $\bar{x}$ is the mean value if the observation.

Equation **(27)**(29) shows the Type B uncertainty ($u_B(x_i)$) for rectangular distribution of frequency distribution of values within the stated bounds [a_- , a_+] [118].

$$u_B(x_i) = \sqrt{\frac{(a_+ - a_-)^2}{12}} \quad \textbf{(27)}$$

The reported expanded uncertainty is based on a standard uncertainty multiplied by a coverage factor k=2, providing a level of confidence of approximately 95%. For instance, the error u_{loss} associated to thermal power could be calculated with equation (28):

$$u_{loss} = \sqrt{\left(\frac{\partial Q_{loss}}{\partial Q_S}u_S\right)^2 + \left(\frac{\partial Q_{loss}}{\partial Q_L}u_L\right)^2 + \left(\frac{\partial Q_{loss}}{\partial Q_{ad}}u_{ad}\right)^2} \quad \textbf{(28)}$$

where u_S, u_L, u_{ad} are the errors related to the different heating contributes. The total uncertainty values for the thermal loss in tests are under 0.1W. In relation to these quantities, it means that relative errors are less than 1.7%. For temperature difference, the necessity to use thermocouples bring a maximum absolute error of 0.8 °C.

2.2 - Improved Indoor Test Stand Setup

In order to obtain more uniformity of temperature along the absorber tube a new test set up has been developed for thermal loss measurement. The concept is similar to the previous test set up and it is based on the Joule effect, feeding electric heaters with current to obtain a steady state condition at different reference temperatures. Figure 41 shows the improved indoor test stand setup. A long cartridge heater (Q_{Main}) is inserted along the length of absorber tube after removing the smaller coaxial steel tube. Instead of nickel-chrome wire heater, an industrial cartridge heater made of resistance wire (NiCr20/80) as a core covered with stainless steel 304 as a sleeve (sheath)

has been used. The cartridge heater with electrical resistance of 4.6 Ω/m supplied by a direct current supplier up to 40 volts.

In order to minimize the temperature gradient between the portion of the metallic tube covered by glass and the one that stands in air, an additional external heater is placed before the Kovar part to meet the adiabatic condition. The external heater is made of a nickel-chrome wire (electrical resistance of 5 Ω/m) covered by polymeric shield and it is fed by direct current supplier up to 15 volts.

Instead of RTD thermocouples, the temperature of the glass envelope is measured by the placement of five type T thermocouples with accuracy of ±1 °C. TC-G1 – TC-G5 are placed uniformly along the glass envelop of the receiver tube. Similar to the previous setup, in order to measure the temperature along the absorber tube six thermocouples are used (Type T with accuracy of ±1 °C). Thermocouples are fixed to the heater to slide inside the tube and placed uniformly along the tube (TC1-TC5). In order to check the temperature gradient along the outlet section of the tube, TC6 is placed outside of it. The ambient temperature are measured by two RTD.

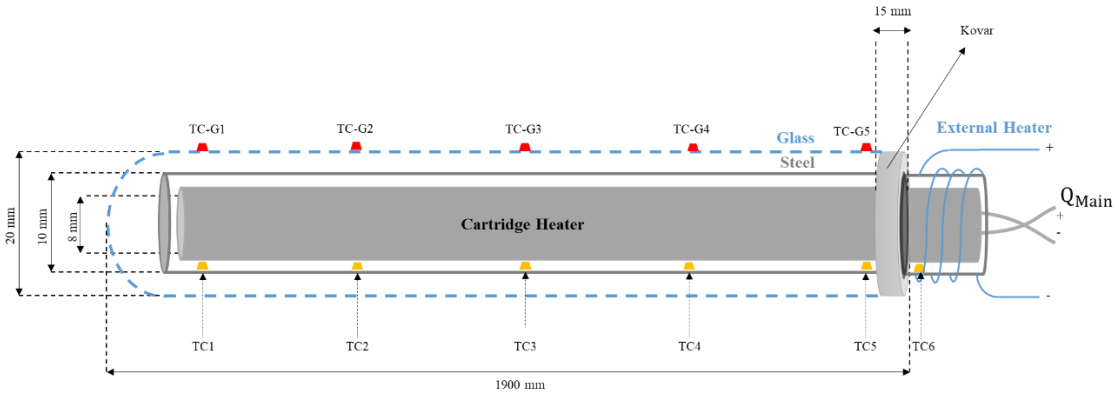

Figure 41. Scheme of the improved indoor test stand set-up for one-end receiver tube for m-PTC.

2.2.1 - Procedure of Improved Indoor Test

Similar to preliminary test set-up a similar procedure has been implemented and Agilent 34970a has been used for reading and recording the direct voltage, TC1-TC6 values, TC-G1 – TC-G6 values and ambient temperature value obtained by two RTDs. In addition, the Agilent 34401a has been used for measurement of direct current value of the main heater.

The data acquisition units has been programmed by with LabVIEW and used to real time monitoring sensors with the display of the main parameters such as voltage, current and power of heaters.

Similar to previous test procedure preliminary tests have been conducted in order to evaluate the uniformity of temperature along the tube and estimate the heating supplier parameters. An overview on precise position of sensors and their surface contact with the heaters and the absorber tube is permitted due to the dimension of the absorber tube.

In order to reach the steady-state condition at different temperature levels the progress is gradually and carefully from one stage to the next. An electrical supply related to the main cartridge heater

(Q_{Main}) is increased. After reaching the uniformity in temperature along the tube based on data obtained from TC1-TC4, electrical supply related to the external heater is also increased slowly until the uniformity in temperature can be followed by TC5 and TC6. Due to the sensitivity of the system, ununiformed variety in temperature gradient along the tube could cause by any small change in electrical supply values. For the main heater, the input power P_{in} can be described by equation (22) based on the Joule effect.

Three different tube from same type have been tested. The first, second and third receiver tubes are named as RT01, RT02 and RT03, respectively. In the range of interest, for RT01 the test procedure was repeated for 50 cases, RT02 was tested for 40 cases and RT03 was tasted for 34 cases. During the tests, the temperature stability was kept for over 10 minutes under the uncertainty of thermocouples (see Figure 42, Figure 43 and Figure 44).

In order to calculate the input power (P_{in}) due to Joule effect for each test on RT01, RT02 and RT03, voltage (U) and current (I) values for the main heater (Q_{Main}) were measured and reported in the Appendix A.

For TR01 the difference between the maximum temperature and the average temperature inside the tube is limited at 10°C. Difference between max and minimum temperature inside the tube is less than 20°C. Mentioned values are similar for TR02. For instance, the difference between the maximum temperature and the average temperature inside the tube is limited at 10°C. Difference between max and minimum temperature inside the tube is less than 23°C. Interestingly, in the range of interest temperature distribution inside the absorber of the TR03 tube is more uniform than the other tubes. For this receiver tube, the difference between the maximum temperature and the average temperature inside the tube is less than 6°C and the difference between max and minimum temperature inside the tube is less than 11°C.

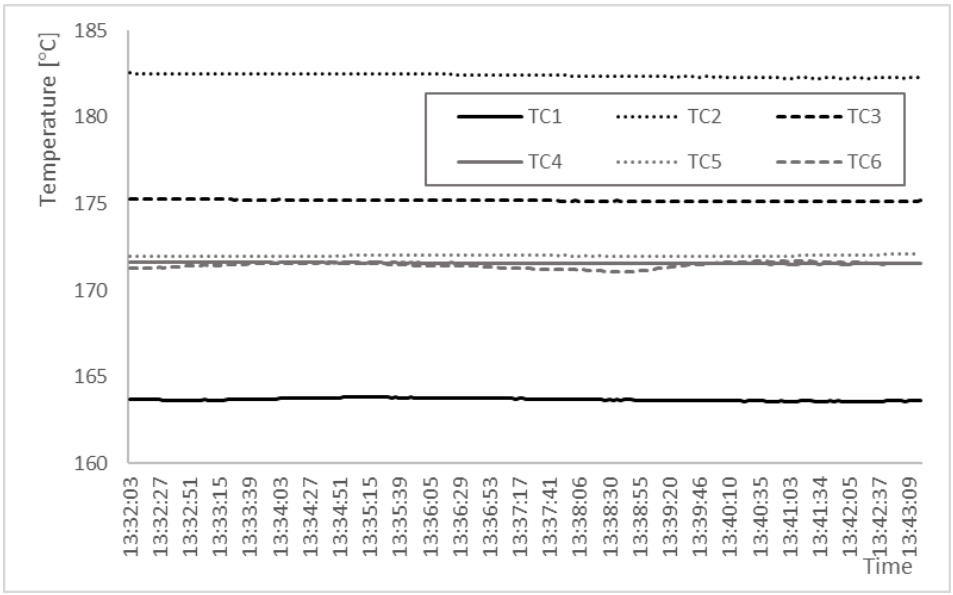

Figure 42. Temperature variation along the absorber tube in Test 45 (ΔT=145°C) for RT01.

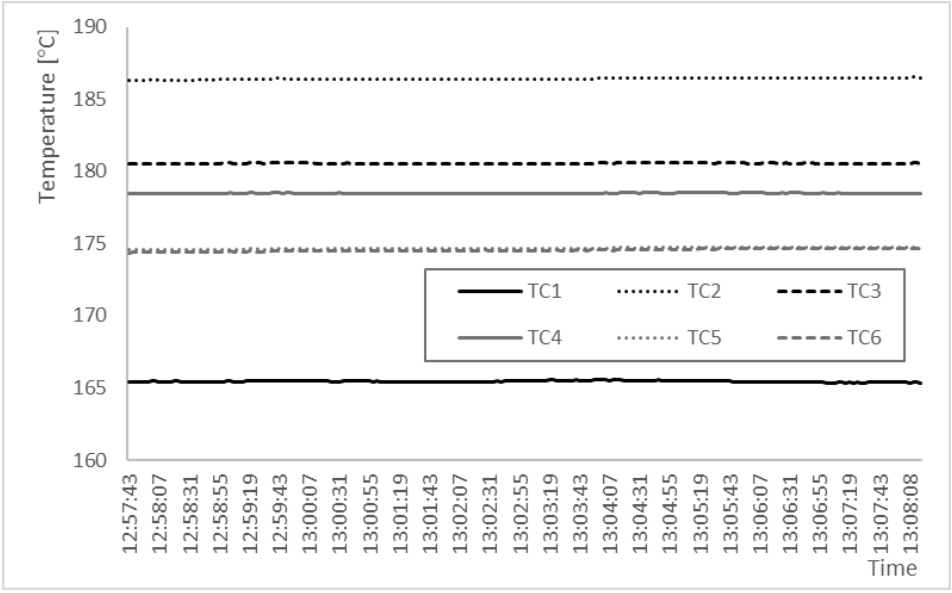

Figure 43. Temperature variation along the absorber tube in Test 32 (ΔT=150°C) for RT02.

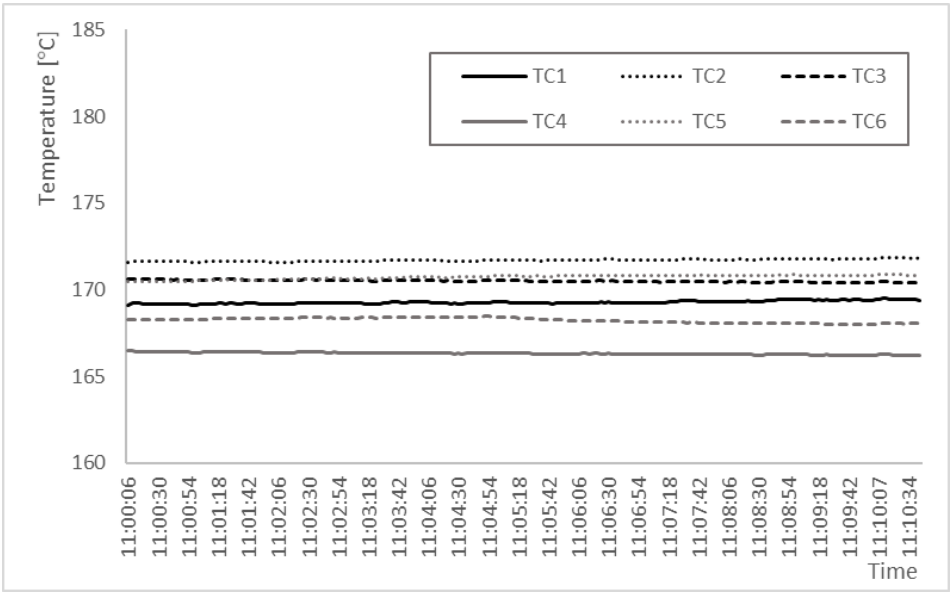

Figure 44. Temperature variation along the absorber tube in Test 30 (ΔT=145°C) for RT03.

Temperatures distribution along the absorber tube during the tests for RT01, RT02 and RT03 are presented in Figure 45, Figure 46 and Figure 47, respectively. In comparison to preliminary test results obtained from test set-up with two nickel-chrome wire heaters (Figure 39), improved test stand shows more uniformity in temperature distribution along the tube. This improvement is more noticeable in values related to the TC3. However, due to the possible displacement of the thermocouples in the end of tube, TC2 values are not in match with the others in RT01 and RT02. It is not possible to verify exactly the reason behind this difference due to the unapproachable side of the tube and internal configuration. Nevertheless, it is less likely to be resulted by the lack in the contact between main cartridge heater and the tube due to small difference in their diameter.

Consequently, reference average temperature (T_{ave}) calculations for heat loss are based on excluding TC2 values. Moreover, the TC6 is in contact with the outlet part of the tube beyond the

Kovar cylinder and it is not under vacuum conditions. Therefore, its value is also excluded from T_{ave} calculations.

However, due to the uniformity of temperature inside the receiver tube in RT03, all the data from TC1-TC5 are included in average temperature (T_{ave}) calculations. Once more, the TC6 is in contact with the outlet part of the tube beyond the Kovar cylinder and it is not under vacuum conditions. Consequently, it is not included in T_{ave} calculations.

Temperature distribution in receiver tube including TC1-TC6 values for each test on RT01, RT02 and RT03 are reported in the Appendix B.

The improved test set-up took shorter time to reach overall stability compared with preliminary test set-up. The required time is reduced from 5 hours for low power to about 2 hours for the same value of power. However, similar to the preliminary test set-up a small increment/decrement in the power supply for the heaters (especially in external heater) causes a non-negligible but slow change in the temperature distribution.

Similar to preliminary test, a specific constraint was also followed as necessary condition in developed test set-up: time intervals were chosen for processing data only when each temperature resulted constant with a variation inside sensor's accuracy (±1°C).

For the highest average temperature (test 50 at 181°C) in test of RT01, a maximum standard deviation of 7.5°C was obtained. While, for lower values such as 55, 85, 98, 107, 119, 133, 149 and 171°C it drops down to 4.2, 4.3, 4.8, 4.2, 5.1, 5.3, 5.8 and 6.7°C, respectively. Similar values were recorded for RT02. A maximum standard deviation of 8.9°C was obtained for the highest average temperature of 184°C (test 35). While, for lower values for average temperature such as 51, 78, 98, 115, 136, 146, 154 and 175°C it drops down to 4.1, 3.3, 4.4, 5.8, 6.2, 6.4, 7.7 and 7.8°C, respectively. Because of the high uniformity in temperature distribution in RT03, results are more interesting. For the highest average temperature (test 34 at 190°C) a maximum standard deviation of 3.1°C was obtained. While, for lower values such as 30, 82, 101, 111, 130, 151, 170 and 180°C it drops down to 1.2, 2.9, 2.9, 2.9, 2.7, 2.5, 2.1 and 2.8°C, respectively.

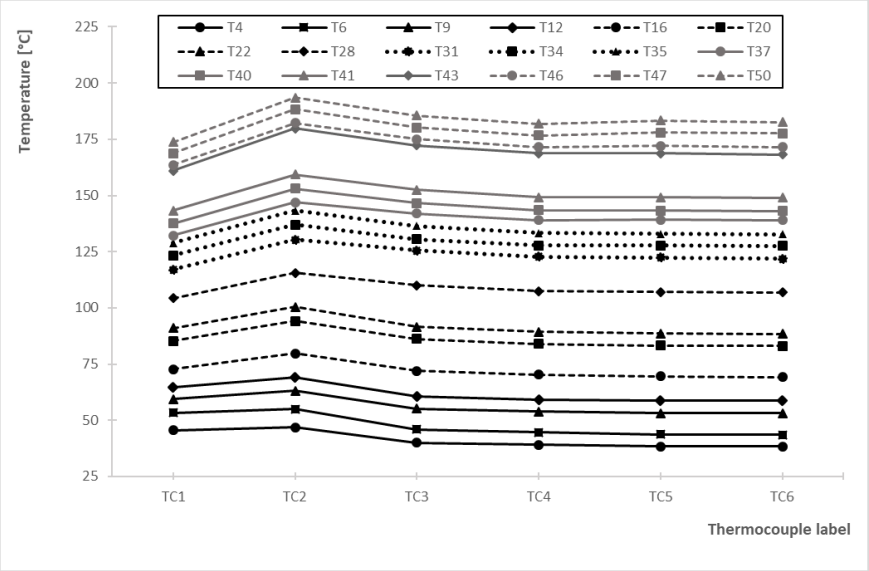

Figure 45. Temperatures distribution along the absorber tube during some tests for RT01.

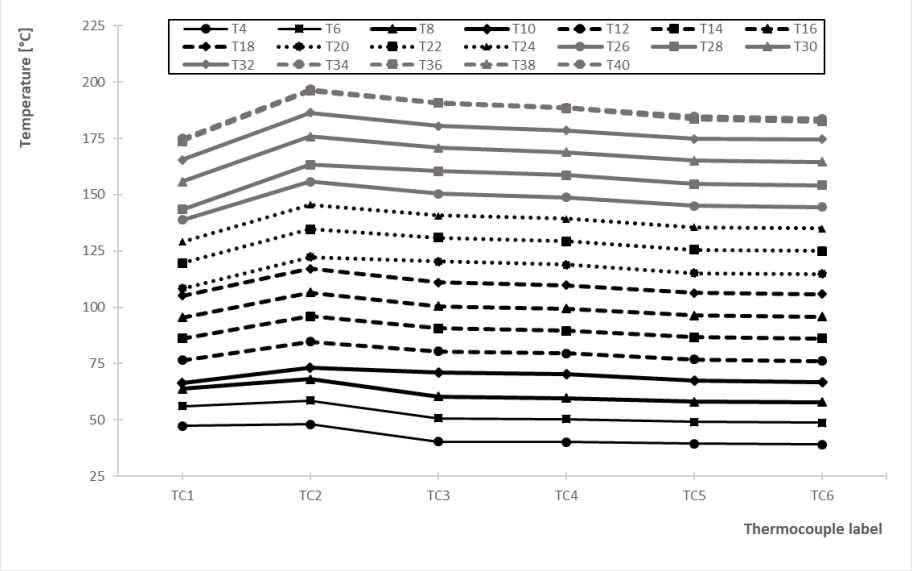

Figure 46. Temperatures distribution along the absorber tube during some tests for RT02.

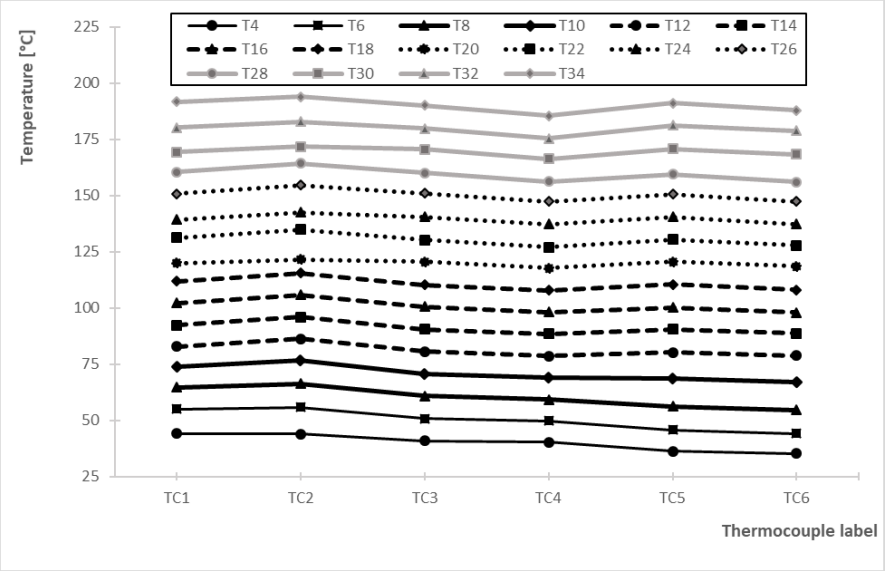

Figure 47. Temperatures distribution along the absorber tube during some tests for RT03.

2.2.2 - Experimental Results of Improved Indoor Test

Similar to the preliminary test set-up, various tests on RT01, RT02 and RT03 have been conducted in order to drive the equation between thermal loss and average temperature for them in the range of interest (up to about 190°C). As mentioned before in average temperature (T_{ave}) calculation for RT01 and RT02 the values related to TC2 are excluded. However, for RT03 is included.

Due to the vacuum between absorber and glass, convection and conduction heat transfer is limited in receiver tube. Therefore, the supply power for main heater (Q_{Main}) was evaluated and it is almost equal to the same amount of heat loss to external ambient. In addition a small, but not negligible heat loss source comes at the outlet portion of the tube where the steel-Kovar junction creates a thermal bridge (Q_{ad}). The heat loss can be described by equation (29).

$$Q_{loss} = Q_{Main} - Q_{ad} \text{ [W]} \quad \textbf{(29)}$$

Where Q_S is the main heater power. During the tests, despite the existence of the external heater the thermal gradient between TC5 and TC6 was not equal to zero. Therefore, conductive heat transfer through the absorber section area at the tube outlet can be described by adiabatic heat (Q_{ad}) based on equation (24).

Similar to the preliminary test, a comprehensive uncertainty analysis have been conducted for RT01, RT02 and RT03 based on Type A errors for experimental data measurement and Type B errors for instrument characteristics and equipment uncertainty. Combined standard uncertainty is also used for error propagation in the derived parameters, based on the sum-of-the-squares method. The reported expanded uncertainty is based on a standard uncertainty multiplied by a coverage factor k=2, providing a level of confidence of approximately 95%.

For RT01, the total uncertainty values for the thermal loss in tests are under 0.01W. In relation to these quantities, it means that relative errors are less than 0.05%. For temperature difference, the necessity to use thermocouples bring a maximum absolute error of 0.8 °C. Table 13 shows test values of RT01 including average temperature of absorber tube, difference between average absorber temperature and ambient temperature and heat loss with related errors for each test point.

The fitting quadratic curve for RT01 can be described by equation (30) and showed in Figure 48. A maximum value of 21.92 W is found when ΔT is 154°C (tube average temperature of 181°C).

$$Q_{loss} = 0.000736\Delta T^2 - 0.026\Delta T\ [W] \quad \textbf{(30)}$$

For RT02, the total uncertainty values for the thermal loss in tests are under 0.01W. In relation to these quantities, it means that relative errors are less than 1.2%. For temperature difference, the necessity to use thermocouples bring a maximum absolute error of 0.8 °C. Table 14 shows test values of RT02 including average temperature of absorber tube, difference between average absorber temperature and ambient temperature and heat loss with related errors for each test point.

The fitting quadratic curve for RT02 can be described by equation (31) and showed in Figure 48. A maximum value of 23.26 W is found when ΔT is 158°C (tube average temperature of 185°C).

$$Q_{loss} = 0.000703\Delta T^2 - 0.035\Delta T\ [W] \quad \textbf{(31)}$$

Table 13. Test values of RT01 (temperatures and heat loss with related errors).

Test	T_{ave} [°C]	ΔT [°C]	ΔT error [°C]	Q_{loss} [W]	Q_{loss} error [W]	Test	T_{ave} [°C]	ΔT [°C]	ΔT error [°C]	Q_{loss} [W]	Q_{loss} error [W]
1	32	9.8	0.8	0.29067	0.00005	26	103	79.3	0.8	6.8276	0.0005
2	32	9.8	0.8	0.29066	0.00006	27	107	79.3	0.8	6.8294	0.0005
3	37	13.8	0.8	0.63695	0.00008	28	107	83.5	0.8	7.4436	0.0006
4	41	18.4	0.8	0.72052	0.00008	29	119	83.3	0.8	7.4399	0.0006
5	47	24.1	0.8	1.13108	0.00011	30	119	94.6	0.8	9.0889	0.0007
6	47	24.1	0.8	1.13025	0.00012	31	122	94.6	0.8	9.0866	0.0007
7	50	27.7	0.8	1.33810	0.00013	32	122	97.8	0.8	9.767	0.004
8	50	27.6	0.8	1.33777	0.00013	33	127	98.0	0.8	9.7779	0.0011
9	55	32.8	0.8	1.76184	0.00016	34	127	103.5	0.8	10.5173	0.0008
10	55	32.6	0.8	1.76194	0.00016	35	133	103.4	0.8	10.478	0.0011
11	61	38.1	0.8	2.2930	0.0002	36	133	109.0	0.8	11.3715	0.0009
12	61	38.0	0.8	2.2823	0.0004	37	138	108.9	0.8	11.3605	0.0009
13	66	43.1	0.8	2.8312	0.0002	38	138	113.5	0.8	12.4946	0.0011
14	66	43.2	0.8	2.8307	0.0002	39	143	113.5	0.8	12.4943	0.0011
15	71	48.4	0.8	3.2549	0.0003	40	143	117.8	0.8	13.2275	0.0009
16	71	48.2	0.8	3.2550	0.0003	41	149	117.7	0.8	13.2282	0.0009
17	78	54.7	0.8	4.0103	0.0003	42	149	123.2	0.8	14.3092	0.0013
18	78	54.7	0.8	4.0103	0.0003	43	168	123.3	0.8	14.295	0.006
19	85	61.4	0.8	4.6635	0.0004	44	168	141.7	0.8	18.6601	0.0014
20	85	61.4	0.8	4.6655	0.0004	45	171	141.8	0.8	18.6532	0.0013
21	89	66.3	0.8	5.3836	0.0004	46	171	144.5	0.8	19.2395	0.0013
22	90	66.7	0.8	5.3843	0.0004	47	176	144.5	0.8	19.2326	0.0014
23	98	74.3	0.8	6.2450	0.0005	48	176	149.8	0.8	20.578	0.002
24	98	74.2	0.8	6.2449	0.0005	49	181	149.7	0.8	20.577	0.004
25	103	9.8	0.8	0.29067	0.0005	50	181	154.4	0.8	21.9175	0.0018

Table 14. Test values of RT02 (temperatures and heat loss with related errors).

Test	T_{ave} [°C]	ΔT [°C]	ΔT error [°C]	Q_{loss} [W]	Q_{loss} error [W]	Test	T_{ave} [°C]	ΔT [°C]	ΔT error [°C]	Q_{loss} [W]	Q_{loss} error [W]
1	32	6.7	0.8	0.234	0.003	21	126	99.9	0.8	10.5593	0.0008
2	33	6.8	0.8	0.17896	0.00003	22	126	100.3	0.8	10.526	0.004
3	42	15.7	0.8	0.67657	0.00008	23	136	109.9	0.8	12.2269	0.0009
4	42	15.7	0.8	0.67606	0.00008	24	136	110.0	0.8	12.2193	0.0009
5	51	25.2	0.8	1.41118	0.00014	25	145	119.2	0.8	13.9026	0.0011
6	52	25.4	0.8	1.41047	0.00014	26	146	119.4	0.8	14.176	0.004
7	60	34.1	0.8	2.15339	0.00019	27	154	128.5	0.8	16.1702	0.0016
8	61	34.1	0.8	2.15323	0.00019	28	154	128.7	0.8	16.152	0.003
9	69	42.6	0.8	3.0840	0.0003	29	165	139.4	0.8	18.3153	0.0014
10	69	42.7	0.8	3.0821	0.0003	30	165	139.3	0.8	18.2951	0.0019
11	78	52.0	0.8	4.0104	0.0003	31	175	148.7	0.8	20.7038	0.0014
12	78	52.2	0.8	4.0097	0.0003	32	175	148.7	0.8	20.6973	0.0017
13	88	61.9	0.8	5.0634	0.0004	33	184	158.3	0.8	23.3344	0.0016
14	88	61.9	0.8	5.0631	0.0004	34	185	158.5	0.8	23.3201	0.0016
15	98	71.4	0.8	6.2060	0.0005	35	184	157.5	0.8	23.2764	0.0016
16	98	71.6	0.8	6.2056	0.0005	36	184	158.0	0.8	23.2634	0.0017
17	107	81.4	0.8	7.6659	0.0006	37	184	158.3	0.8	23.249	0.002
18	108	81.7	0.8	7.5138	0.0006	38	184	158.4	0.8	23.2520	0.0019
19	115	89.6	0.8	8.850	0.003	39	185	158.5	0.8	23.2481	0.0017
20	116	89.8	0.8	8.8679	0.0009	40	185	158.5	0.8	23.2558	0.0018

For RT03, the total uncertainty values for the thermal loss in tests are under 0.01W. In relation to these quantities, it means that relative errors are less than 0.05%. For temperature difference, the necessity to use thermocouples bring a maximum absolute error of 0.7 °C. Table 15 shows test values of RT03 including average temperature of absorber tube, difference between average absorber temperature and ambient temperature and heat loss with related errors for each test point.

The fitting quadratic curve for RT03 can be described by equation (32) and showed in Figure 48. A maximum value of 17.89 W is found when ΔT is 163°C (tube average temperature of 190°C).

$$Q_{loss} = 0.000566\Delta T^2 - 0.0146\Delta T\ [W] \quad \textbf{(32)}$$

Table 15. Test values of RT03 (temperatures and heat loss with related errors).

Test	T_{ave} [°C]	ΔT [°C]	ΔT error [°C]	Q_{loss} [W]	Q_{loss} error [W]	Test	T_{ave} [°C]	ΔT [°C]	ΔT error [°C]	Q_{loss} [W]	Q_{loss} error [W]
1	30	4.7	0.7	0.12394	0.00002	18	111	84.3	0.7	5.3976	0.0004
2	30	5.0	0.7	0.12393	0.00002	19	120	93.7	0.7	6.5142	0.0005
3	40	14.8	0.7	0.57552	0.00007	20	120	93.9	0.7	6.5058	0.0006
4	41	15.4	0.7	0.57543	0.00007	21	130	104.0	0.7	7.7006	0.0006
5	51	25.2	0.7	1.00889	0.00011	22	131	104.1	0.7	7.7016	0.0006
6	51	25.4	0.7	1.00839	0.00011	23	140	113.6	0.7	9.2037	0.0007
7	61	35.4	0.7	1.48624	0.00014	24	140	113.7	0.7	9.2083	0.0008
8	61	35.4	0.7	1.48616	0.00014	25	151	124.0	0.7	10.7364	0.0011
9	72	45.4	0.7	2.19733	0.00019	26	151	124.2	0.7	10.7308	0.0009
10	72	45.5	0.7	2.19667	0.00019	27	160	133.2	0.7	12.0993	0.0009
11	81	55.2	0.7	2.8850	0.0002	28	160	133.2	0.7	12.0919	0.0011
12	82	55.3	0.7	2.8845	0.0002	29	170	143.0	0.7	13.9324	0.0015
13	91	64.9	0.7	3.6713	0.0003	30	170	143.0	0.7	13.9061	0.0013
14	91	65.0	0.7	3.6705	0.0003	31	180	153.1	0.7	15.5825	0.0018
15	101	74.6	0.7	4.4887	0.0004	32	180	152.9	0.7	15.676	0.007
16	101	74.7	0.7	4.4882	0.0004	33	190	163.3	0.7	17.9029	0.0017
17	111	84.2	0.7	5.3982	0.0004	34	190	163.2	0.7	17.8859	0.0014

The receiver thermal loss parameters (coefficient of a_1, a_2 in equation (23)) result from fitting a model equation to the experimental data. Weighted Least Squares (WLS) method has been used for fitting the measurement data and determine the values of coefficients. In WLS method measurement points with higher uncertainty have less impact on the obtaining fit than those with lower uncertainty. Table 16 shows the regression parameters and their associated errors based on LS and WLS methods for RT01, RT02 and RT03 receiver tube.

Table 16. Regression of RT01, RT02 and RT03 thermal loss parameters based on LS and WLS methods and associated errors.

Method		**LS**		**WLS**	
Tube		a_1	a_2	a_1	a_2
RT01	Estimate	0.000715	0.030	0.000736	0.026
	Uncertainty	-	-	0.000014	0.002
RT02	Estimate	0.000691	0.037	0.000703	0.035
	Uncertainty	-	-	0.000011	0.002
RT03	Estimate	0.000539	0.0200	0.000566	0.0146
	Uncertainty	-	-	0.000009	0.0016

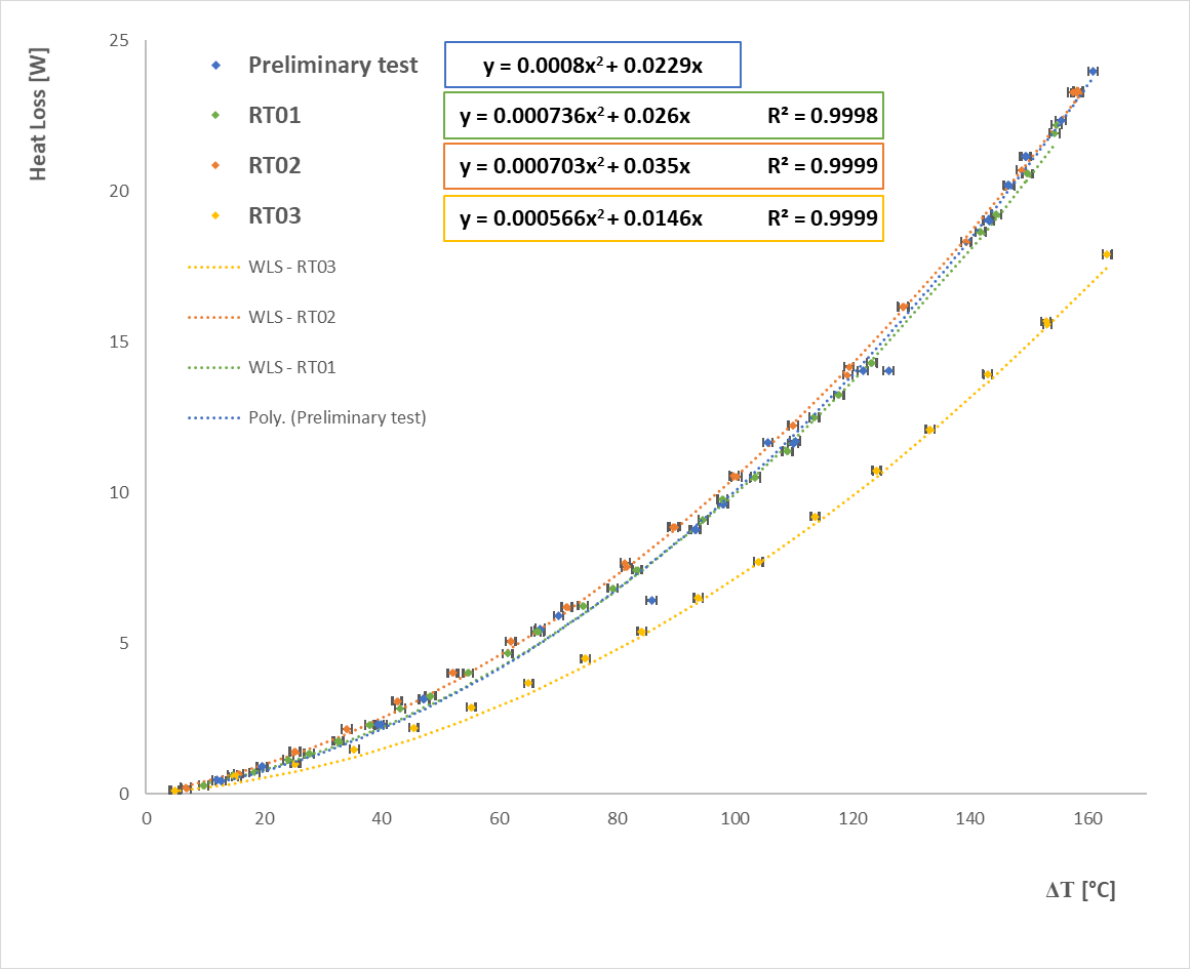

Figure 48. Heat loss as a function of the difference between the average absorber temperature and the ambient temperature for preliminary test, RT01, RT02 and RT03.

2.3 - New Results of Improved Indoor Test Stand Setup

After the individuation of the different results related to the RT03, new tests have been conducted on additional tubes in order to obtain production assurance and have more clear vision about the results. Similar setup and test procedure have been conducted in order to evaluate the uniformity of temperature along the tube and estimate the heating supplier parameters in additional tubes.

Seven different tube from same type have been tested and labeled as RT04-RT10. In the range of interest, for RT04 the test procedure was repeated for 11 cases, RT05 was tested for 11 cases, RT06 was tested for 15 cases, RT07 was tested for 13 cases, RT08 was tested for 12 cases, RT09 was tested for 14 cases and RT10 was tested for 15. During the tests, the temperature stability was kept for over 10 minutes under the uncertainty of thermocouples. In order to calculate the input power (P_{in}) due to Joule effect for each test on RT04- RT10, voltage (U) and current (I) values for the main heater (Q_{Main}) were measured and reported in the Appendix A.

For RT04, RT05, RT06, RT07, RT08, RT09 and RT10 the difference between the maximum temperature and the average temperature inside the tube are limited at 9°C, 9°C, 8°C, 7°C, 12°C, 13°C and 8°C, respectively. Difference between max and minimum temperature inside the tubes are less than 23°C for RT04-RT10. Figure 49 shows the difference between max and minimum temperature obtained by TC1-TC5 inside the absorber tube. The reported expanded uncertainty in Figure 49 is based on a standard uncertainty multiplied by a coverage factor k=2, providing a level of confidence of approximately 95%. Temperature distribution in receiver tube including TC1-TC6 values for each test on RT01-RT10 are reported in the Appendix B.

For the highest average temperature (test 11 at 181°C) in test of RT04, a maximum standard deviation of 6.3°C has been obtained. While, for lower values such as 81, 119, 139 and 158°C it drops down to 3.4, 5.5, 5.6 and 5.8°C, respectively. Similar values have been recorded for RT05. A maximum standard deviation of 6.9°C has been obtained for the highest average temperature of 182°C (test 11). While, for lower values for average temperature such as 63, 84, 104, 118, 141 and 162°C it drops down to 4.5, 5.6, 5.9, 6.0 and 6.0°C, respectively. A maximum standard deviation of 8.4°C has been obtained for RT06 at the highest average temperature of 188°C (test 16). For lower values such as 62, 81, 121, 140, 159 and 178°C it drops down to 3.6, 4.2, 5.8, 6.7, 7.4 and 8.1°C, respectively. Similar values have been recorded for RT07-RT10 and maximum standard deviation for RT07, RT08, RT09 and RT10 are 8.0, 8.1, 7.5 and 7.7°C at the highest average temperature of 178, 180,180 and 177°C, respectively.

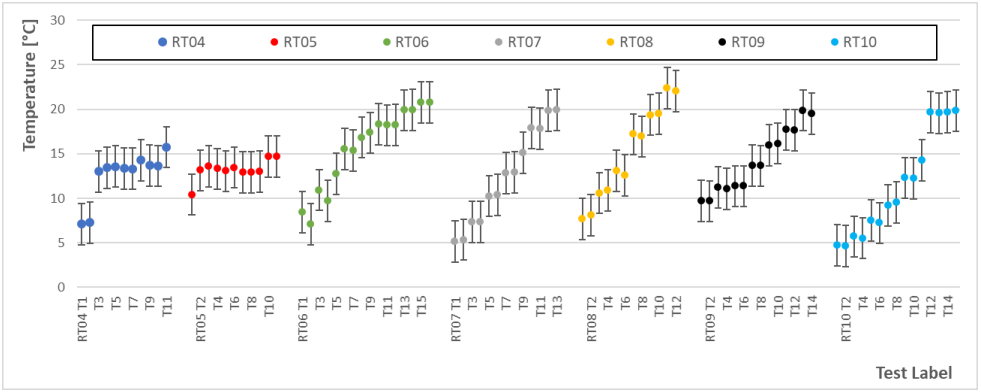

Figure 49. Difference between max and minimum temperature obtained by TC1-TC5 inside the absorber tube RT04-RT10.

The test set-up took about 2 hours to reach overall stability for the various values of power. However, similar to the tests on RT01-RT03 a small increment/decrement in the power supply for the heaters (especially in external heater) causes a non-negligible but slow change in the temperature distribution. Time intervals were chosen for processing data only when each temperature (recorded by TC1-TC5) resulted constant with a variation inside sensor's accuracy (±1°C).

Several tests on RT04-RT10 have been conducted in order to drive the equation between thermal loss and average temperature for them in the range of interest (up to about 190°C). The average temperature (T_{ave}) calculation for RT04-RT10 the values related to TC6 are excluded (TC6 is placed in outlet of the absorber tube) and values related to TC1-TC5 are included. Similar to previous tests on RT01-RT03) the heat loss can be described by equation (29).

A comprehensive uncertainty analysis have been conducted for RT04-RT10 based on Type A errors for experimental data measurement and Type B errors for instrument characteristics and equipment uncertainty. Combined standard uncertainty is also used for error propagation in the derived parameters, based on the sum-of-the-squares method. The reported expanded uncertainty is based on a standard uncertainty multiplied by a coverage factor k=2, providing a level of confidence of approximately 95%. For RT04, RT05, RT06 and RT07 the total uncertainty values for the thermal loss in tests are under 0.01W. In relation to these quantities, it means that relative errors are less than 0.05%. For temperature difference, the necessity to use thermocouples bring a maximum absolute error under 0.8 °C. Table 17, Table 18, Table 19 and Table 20 show test values of RT04, RT05, RT06 and RT07, respectively. Including average temperature of absorber tube, difference between average absorber temperature and ambient temperature and heat loss with related errors for each test point.

Table 17. Test values of RT04 (temperatures and heat loss with related errors).

Test	T_{ave} [°C]	ΔT [°C]	ΔT error [°C]	Q_{loss} [W]	Q_{loss} error [W]		Test	T_{ave} [°C]	ΔT [°C]	ΔT error [°C]	Q_{loss} [W]	Q_{loss} error [W]
1	81	59.7	0.7	4.5198	0.0005		7	139	118.1	0.7	12.6454	0.0009
2	81	59.8	0.7	4.5158	0.0004		8	140	120.3	0.7	12.8832	0.0011
3	119	97.9	0.7	9.3502	0.0007		9	158	137.1	0.7	16.4612	0.0014
4	119	98.0	0.7	9.3466	0.0007		10	158	137.1	0.7	16.4483	0.0015
5	119	98.0	0.7	9.3434	0.0007		11	181	161.4	0.7	22.0532	0.0015
6	139	118.2	0.7	12.6436	0.0009							

Table 18. Test values of RT05 (temperatures and heat loss with related errors).

Test	T_{ave} [°C]	ΔT [°C]	ΔT error [°C]	Q_{loss} [W]	Q_{loss} error [W]		Test	T_{ave} [°C]	ΔT [°C]	ΔT error [°C]	Q_{loss} [W]	Q_{loss} error [W]
1	63	44.0	0.7	2.7708	0.0002		7	162	142.8	0.7	17.6609	0.0012
2	84	64.8	0.7	4.8637	0.0004		8	162	142.8	0.7	17.6642	0.0012
3	104	84.8	0.7	7.3630	0.0005		9	162	142.9	0.7	17.6555	0.0013
4	118	98.3	0.7	9.2531	0.0007		10	182	163.0	0.7	22.6729	0.0018
5	118	98.1	0.7	9.2525	0.0007		11	182	163.1	0.7	22.6723	0.0016
6	141	121.4	0.7	13.2666	0.0010							

Table 19. Test values of RT06 (temperatures and heat loss with related errors).

Test	T_{ave}	ΔT	ΔT error	Q_{loss}	Q_{loss} error	Test	T_{ave}	ΔT	ΔT error	Q_{loss}	Q_{loss} error
	[°C]	[°C]	[°C]	[W]	[W]		[°C]	[°C]	[°C]	[W]	[W]
1	62	43.8	0.7	2.5567	0.0002	9	159	139.1	0.7	16.7510	0.0014
2	61	41.4	0.7	2.5222	0.0002	10	159	139.1	0.7	16.7478	0.0012
3	81	62.3	0.7	4.4227	0.0003	11	159	139.1	0.7	16.7430	0.0012
4	80	60.9	0.7	4.3849	0.0004	12	178	158.5	0.7	21.3339	0.0016
5	101	81.6	0.7	6.6829	0.0005	13	178	158.5	0.7	21.3313	0.0015
6	121	101.5	0.7	9.5392	0.0007	14	188	167.9	0.7	23.7909	0.0016
7	140	120.5	0.7	12.7264	0.0009	15	188	168.0	0.7	23.7884	0.0016
8	140	120.4	0.7	12.7264	0.0009						

Table 20. Test values of RT07 (temperatures and heat loss with related errors).

Test	T_{ave}	ΔT	ΔT error	Q_{loss}	Q_{loss} error	Test	T_{ave}	ΔT	ΔT error	Q_{loss}	Q_{loss} error
	[°C]	[°C]	[°C]	[W]	[W]		[°C]	[°C]	[°C]	[W]	[W]
1	62	41.9	0.7	2.7243	0.0002	8	119	99.8	0.7	9.8368	0.0007
2	62	42.1	0.7	2.7239	0.0002	9	139	119.6	0.7	13.2401	0.0013
3	81	61.6	0.7	4.7191	0.0004	10	158	138.7	0.7	17.2787	0.0014
4	81	61.6	0.7	4.7185	0.0004	11	158	138.7	0.7	17.2847	0.0013
5	101	81.7	0.7	7.0593	0.0005	12	178	157.9	0.7	21.8818	0.0015
6	101	81.6	0.7	7.0586	0.0005	13	178	157.8	0.7	21.8792	0.0015
7	119	99.9	0.7	9.8369	0.0007						

For RT08, RT09 and RT10 the total uncertainty values for the thermal loss in tests are under 0.01W. In relation to these quantities, it means that relative errors are less than 0.05%. For temperature difference, the necessity to use thermocouples bring a maximum absolute error under 0.8 °C. Table 21, Table 22 and Table 23 show test values of RT08, RT09 and RT10, respectively. Including average temperature of absorber tube, difference between average absorber temperature and ambient temperature and heat loss with related errors for each test point.

Table 21. Test values of RT08 (temperatures and heat loss with related errors).

Test	T_{ave}	ΔT	ΔT error	Q_{loss}	Q_{loss} error	Test	T_{ave}	ΔT	ΔT error	Q_{loss}	Q_{loss} error
	[°C]	[°C]	[°C]	[W]	[W]		[°C]	[°C]	[°C]	[W]	[W]
1	62	43.0	0.7	2.7778	0.0002	7	140	120.2	0.7	14.0318	0.0011
2	62	43.0	0.7	2.7777	0.0002	8	140	120.3	0.7	14.0362	0.0011
3	83	63.4	0.7	4.9181	0.0004	9	159	139.4	0.7	17.8320	0.0012
4	83	63.5	0.7	4.9175	0.0004	10	159	139.4	0.7	17.8261	0.0014
5	103	83.8	0.7	7.5647	0.0006	11	180	159.9	0.7	23.26	0.003
6	103	83.9	0.7	7.5639	0.0006	12	180	160.0	0.7	23.1337	0.0016

Table 22. Test values of RT09 (temperatures and heat loss with related errors).

Test	T_{ave}	ΔT	ΔT error	Q_{loss}	Q_{loss} error	Test	T_{ave}	ΔT	ΔT error	Q_{loss}	Q_{loss} error
	[°C]	[°C]	[°C]	[W]	[W]		[°C]	[°C]	[°C]	[W]	[W]
1	60	39.9	0.7	2.3820	0.0002	8	122	101.6	0.7	10.0153	0.0007
2	60	39.7	0.7	2.3818	0.0002	9	141	120.1	0.7	13.3062	0.0009
3	82	61.7	0.7	4.6201	0.0004	10	141	120.0	0.7	13.3049	0.0011
4	82	61.9	0.7	4.6181	0.0004	11	160	139.1	0.7	17.2963	0.0013
5	103	82.7	0.7	7.2861	0.0006	12	160	139.2	0.7	17.3026	0.0012
6	103	83.1	0.7	7.2827	0.0005	13	180	159.3	0.7	21.8986	0.0016
7	122	101.6	0.7	10.0116	0.0007	14	180	159.4	0.7	21.9046	0.0015

Table 23. Test values of RT10 (temperatures and heat loss with related errors).

Test	T_{ave} [°C]	ΔT [°C]	ΔT error [°C]	Q_{loss} [W]	Q_{loss} error [W]	Test	T_{ave} [°C]	ΔT [°C]	ΔT error [°C]	Q_{loss} [W]	Q_{loss} error [W]
1	41	21.2	0.7	1.06146	0.00011	9	119	98.7	0.7	9.7288	0.0007
2	41	21.2	0.7	1.06156	0.00011	10	119	98.5	0.7	9.7310	0.0007
3	61	40.8	0.7	2.6239	0.0002	11	138	117.9	0.7	13.0247	0.0009
4	61	40.8	0.7	2.6239	0.0002	12	160	138.2	0.7	18.0239	0.0016
5	80	60.0	0.7	4.5552	0.0005	13	160	138.5	0.7	18.0132	0.0016
6	80	60.0	0.7	4.5532	0.0004	14	177	156.1	0.7	21.9119	0.0015
7	100	79.2	0.7	6.8375	0.0005	15	177	156.1	0.7	21.9078	0.0016
8	100	79.3	0.7	6.8374	0.0005						

The receiver thermal loss parameters (coefficient of a_1, a_2 in equation (23)) result from fitting a model equation to the experimental data. Weighted Least Squares (WLS) method has been used for fitting the measurement data and determine the values of coefficients. Table 24 shows the regression parameters and their associated errors based on LS and WLS methods for RT04-RT10 receiver tube.

The fitting quadratic curve for RT04-RT10 can be described based on reported values in Table 24 and showed in Figure 50. For RT04, RT05, RT06, RT07, RT08, RT09 and RT10 a maximum value of 22.05, 22.67, 23.79, 21.88, 23.13, 21.90 and 21.91 W were obtained at ΔT (difference between tube average temperature and ambient temperature) of 161, 163, 168, 158, 160, 159 and 156°C, respectively.

Table 24. Regression of RT04-RT10 thermal loss parameters based on LS and WLS methods and associated errors.

Method		LS		WLS	
Tube		a_1	a_2	a_1	a_2
RT04	Estimate	0.000625	0.034	0.00064	0.032
	Uncertainty	-	-	0.00002	0.004
RT05	Estimate	0.00066	0.029	0.00068	0.027
	Uncertainty	-	-	0.00002	0.003
RT06	Estimate	0.000684	0.025	0.000708	0.021
	Uncertainty	-	-	0.000019	0.004
RT07	Estimate	0.000595	0.039	0.000677	0.031
	Uncertainty	-	-	0.000015	0.003
RT08	Estimate	0.00069	0.032	0.00071	0.031
	Uncertainty	-	-	0.00002	0.003
RT09	Estimate	0.000653	0.033	0.000659	0.032
	Uncertainty	-	-	0.000008	0.001
RT10	Estimate	0.00069	0.032	0.00071	0.028
	Uncertainty	-	-	0.00002	0.004

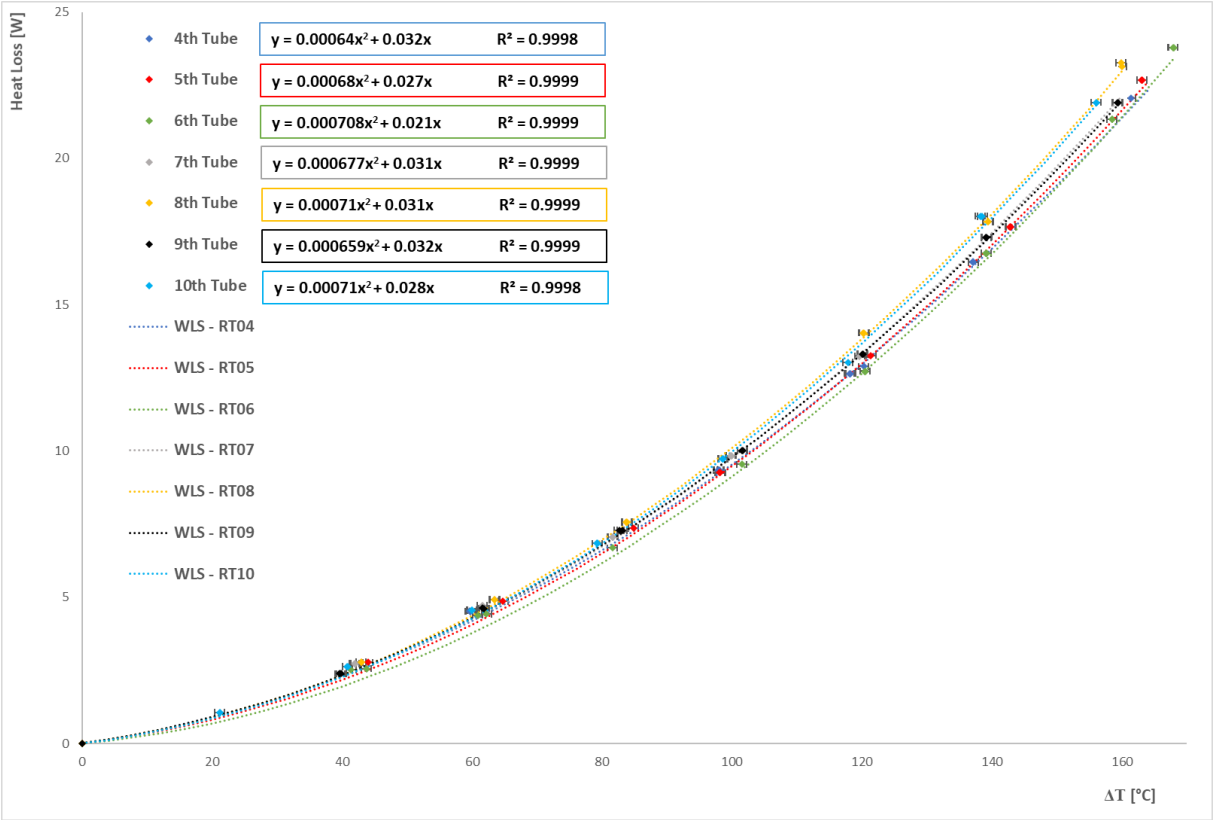

Figure 50. Heat loss as a function of the difference between the average absorber temperature and the ambient temperature for RT01-RT10.

Results from previous tests on RT01 and RT02 are in accordance with new results obtained from heat loss test on RT04-RT10. Therefore, the different results related to the RT03 are to be expected as a result of variation in production quality by manufacturer of receiver tube. Since the relative uncertainty values for the thermal loss in all tests is less than 0.05%.

Due to the similarity of RT01, RT02, RT04, RT05, RT06, RT07, RT08, RT09 and RT10 in terms of production quality, an overall estimation of receiver tube characteristics based on thermal loss can be described by the receiver thermal loss parameters (coefficient of a_1, a_2). Result from fitting a model equation to the experimental data on 181 test points lead to the receiver thermal loss parameters presented in Table 25. Weighted Least Squares (WLS) method has been used for fitting the measurement data and determine the values of coefficients. For overall estimation, the total uncertainty values for the thermal loss tests are under 0.01W. In relation to these quantities, it means that relative errors are less than 0.05%.

Figure 51 shows the heat loss as a function of the difference between the average absorber temperature and the ambient temperature for overall estimation (RT01, RT02 and RT04-RT10) and RT03 for comparison.

Table 25. Regression of RT04-RT10 thermal loss parameters based on LS and WLS methods and associated errors.

Method		**LS**		**WLS**	
Tube		a_1	a_2	a_1	a_2
Total	Estimate	0.000683	0.031	0.000702	0.027
	Uncertainty	-	-	0.000014	0.003

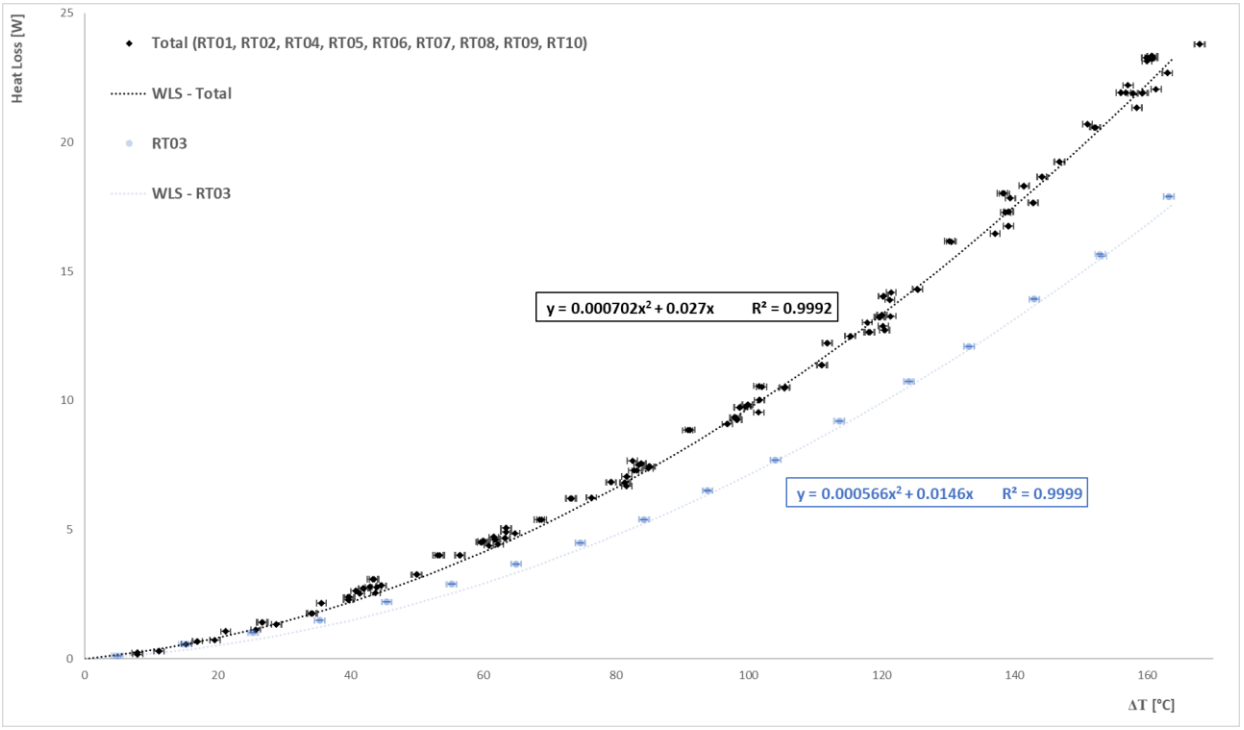

Figure 51. Heat loss as a function of the difference between the average absorber temperature and the ambient temperature for RT01-RT10.

3 - Thermal Loss Simulation of Receiver

3.1 - Introduction and Literature Review

As mentioned in previous chapters in general definition, parabolic trough collectors are typically made by bending a sheet of reflective material into a parabolic shape. The receiver tube is placed along the focal line of the collector and the concentrated radiation reaching the receiver tube heats the fluid that circulates through it, thus transforming the solar radiation into useful heat. The receiver tube consists of an absorber tube surrounded by a glass envelope. This absorber tube is typically stainless steel tube with a selective coating in order to provide the required optical and radiative properties. A high absorptance for solar radiation with low emittance for the temperature range in which the surface emits radiation are among the most important key features for good selective coating on absorber tube. The glass envelope is an anti-reflective evacuated glass tube which protects the absorber from degradation and reduces heat losses. The vacuum enclosure is used primarily to significantly reduce heat losses at high operating temperatures and to protect the solar-selective absorber surface from oxidation [50,120].

Parabolic trough collector (PTC) is the main and one of the most promising technologies available among medium-temperature solar collectors for commercial and industrial applications [121]. Heat collection element (HCE) also called receiver tube is located at the focal axis of the reflector (mirror). The heat transfer analysis of these HCEs is important for the evaluation of thermal losses and sizing of the solar power plant during initial design phase and also permits to evaluate the effect of collector degradation and heat transfer fluid flow rate control strategies on overall plant performance [122]. Therefore, the receiver tube of a PTC is a central and critical component. The heat transfer analysis of the PTCs mainly focused on the prediction of the thermal performance of the receiver tube.

Referred to the importance of heat transfer analysis in PTCs and HCEs, since 1970s several studies and models have been proposed [120]. In 1976, an early study published on performance analysis of a cylindrical parabolic focusing collector by Edenburn and reported the efficiency of PTC based on analytical heat transfer model for evacuated and non-evacuated case [123]. In 1979, Ratzel et al. [124] reported analytical and numerical study of the heat conduction and convective losses in an annular receiver for different geometries. Later in 1982, Clark [125] reported the effect of design and manufacturing parameters of PTC on economical and thermal performance of HCE. In the 90s, various studies published on numerical and analytical heat transfer model of PTC and HCE [126–128].

In 2003, R. Forristall reported a detailed on dimensional heat transfer and energy balance model of solar receiver in order to evaluate thermal performance of PTCs under different operating conditions [129]. Z.D. Cheng et al. [130], presented 3D numerical study of heat transfer characteristics in the receiver tube of PTC. Their study is mainly focused on the effect of large non-uniformity of the solar energy flux distribution on the outer surface of the inner absorber tube. This Non-uniform energy flux distribution could cause an asymmetrically flow heating. In order to, accurately predict the convective heat transfer rate for this type of flow, a three-dimensional computational fluid dynamics model proposed by mentioned authors. By combining the Monte Carlo Ray-Trace (MCRT) method and the FLUENT software, 3D numerical simulation of coupled heat transfer characteristics in the receiver tube is calculated and analyzed. It was obtained that the

average difference with test results from three typical testing conditions, is within 2%. In addition, the radiation loss should be as low as possible to improve the collector efficiency.

Ya-Ling He et al. [131], studied a coupled simulation method based on Monte Carlo Ray Trace (MCRT) and Finite Volume Method (FVM) on parabolic trough solar collector system in order to solve the complexity coupled heat transfer of radiation, heat conduction and convection. It was achieved that by increasing the concentration ratios, the shadow effect of absorber tube become weaker, the angle span of reducing area become larger, the heat flux distributions become gentler.

R.V. Padilla et al. [120], reported a detailed one dimensional numerical heat transfer analysis of a PTC by dividing the receiver and envelope into several segments. In their model, mass and energy balance were applied in each segment and the nonlinear algebraic equations and the partial differential equations were solved simultaneously. In order to validate the numerical results, the model was compared with experimental data obtained from Sandia National Laboratory (SNL). The authors proposed that, by reducing the overestimation of thermal losses by convection (about 41.8%) the model leads to more accurate results.

S.A. Kalogirou from Cyprus University of Technology is published a detailed thermal model of a PTC and the thermal analysis of the receiver including all modes of heat transfer. Mentioned model is developed in the Engineering Equation Solver (EES) and is validated with known performance of existing collectors. It was observed that thermal efficiency obtained from modeling is about 58% at 200 °C [132].

W. Huang et al. [133], studied a modified integration algorithm and a new analytical model for optical performance of PTC with vacuum tube receiver. In this study, the optical efficiency is simulated by numerical integration algorithm after derivation of analytical equation for optical efficiency of each point at reflector. As well as optical parameters, the effects of position error from installation of receiver, transmittance of receiver, absorptivity of receiver, tracking error, optical error and optical properties of reflector on system are simulated and analyzed. It was found that under normal incident, the tracking error leads to low optical efficiency and tracking error of 12 m rad leads to the optical efficiency of 53%.

A.A. Hachicha et al. [134], presented a heat transfer analysis of the heat collector element by numerical simulation based on the finite volume method. In their model, the different elements of the receiver were divided into several segments in both axial and azimuthal directions and energy balances were used for each control volume. It was achieved that the maximum deviation in glass temperature and heat loss value for UVAC3 and PTR70 collectors are 3.9 and 12%, respectively. Finally, their overall model showed an acceptable agreement with experimental and analytical results.

Zhiyong Wu et al. [135], studied a coupled transient model based on a MCRT code and FLUENT software for parabolic trough receiver and detailed temperature distribution of the receiver is simulated. In their model, the heat transfer fluid flow, radiation and conduction heat transfers are considered. In addition, the temperature difference in their model is changed inversely with heat transfer fluid velocity. Comparison with indoor experimental results are also reported and showed an average difference of maximum 6%. Furthermore, the transient behaviors of parabolic trough receiver under direct concentrated solar irradiance are reported. Results of this paper also showed that the stagnation temperature of parabolic trough receiver increase linearly with time and the heat loss through the bellows is around 7% of the total heat loss.

L.S. Conrado et al. [83], studied thermal performance of PTCs by reviewing several types of numerical and simulation methods, mathematical models and experimental studies in regard to temperature, environmental conditions, heat loss and heat flux. In addition, cost analysis and economic strategies used for PTCs are presented by considering initial investment, operation, maintenance and instrumentation cost. Furthermore, they reported that a limited number of commercial software have been used in order to analyses the thermal performance of a PTC. Based on their suggestions, simulations and numerical methods proposed in upcoming studies should not require large computation requirements, since the important point for an intelligent optimization is to obtain a solution within tactically-relevant time lines (hours) rather than weeks/months.

G. Kumaresan et al. [136], reviewed the experimental and numerical studies on heat transfer enhancement techniques in order to minimizing the heat loss by use of nanofluid as a HTF and selective coatings in the receiver tube of a solar PTC. Among the reviewed selective coatings, the black chrome coating showed higher absorbance and lower thermal emittance. In addition, in this study the main sources for heat loss in the receiver tube are presented and comparative study of various heat transfer enhancement techniques are mentioned.

İbrahim Halil Yılmaz et al. [121], reported a comprehensive review on modeling, simulation and performance analysis of PTC. Their paper is mainly focused on optical and thermal models of PTC presented by different authors and for optical modeling, analytical and ray-tracing approaches are investigated. In addition, steady and transient heat transfer conditions are studied for thermal modeling.

In this chapter a detailed heat transfer model based on in-door heat loss test set-up is presented and validated.

3.2 - Solar receiver FEM Model

A Finite Element Method (FEM) has been used in order to predict the thermal performance and analyze the relevant physical characteristics of the receiver tube (specially the value of emissivity at higher temperature). Heat transfer model using FEM simulation method has been realized with Comsol Multiphysics version 5.5.

The receiver tube have axisymmetric geometries and in order to limit the computation time a 2D axisymmetric stationary model has been developed. The main purpose of the model is focused on the thermal properties of the receiver tube in in-door test thereby the parabolic mirror and the support brackets of the receiver tube have been not modelled. The fluid flow inside the absorber tube has been excluded from modeling due to the small gap between the cartridge heater and absorber tube. The Joule Heating interface has been combined with the electric currents and heat transfer in solids interfaces with capabilities for modeling Joule heating (resistive heating). However, due to the uniformity of cartridge heater inside the absorber tube along the receiver, no noticeable difference has been observed for using Joule Heating interface instead of heat source interface. As a result, a fixed thermal flow and therefore the heat transfer inside the receiver has been modeled by heat source interface.

The basis of the Heat Transfer Module (HTM) is the study of the balance of energy in a system. The contributions to this energy balance originate from conduction, convection, and radiation, as well as from latent heat, Joule heating, heat sources, and heat sinks. The heat transfer equations

have been defined automatically by the dedicated physics interfaces for heat transfer. Physical properties such as thermal conductivity, heat capacity, density, and emissivity have been obtained from the built-in material library or from receiver tube producer. Values for emissivity, heat capacity, density and thermal conductivity related to the heater, glass envelop, Kovar and absorber are listed in Table 26.

Table 26. Physical properties related to the elements of receiver.

Element of Receiver	Heat capacity [J/(kgK)]	Density [kg/m^3]	Thermal conductivity [W/(mK)]	Emissivity at 25°C
Heater	440	7870	76.2	-
Glass Envelope	730	2210	1.4	0.85
Kovar	460	8300	17	0.3
Absorber	475	7850	15.1	0.2

The heat transfer model is based on an energy balance between the cartridge heater, HCE (receiver tube) and the surroundings. In practical outdoor condition, the solar energy reflected by the mirrors is absorbed by the glass envelope and the absorber tube surface. A part of energy absorbed into the absorber is transferred to the heat transfer fluid by forced convection and the remaining energy is transferred back to the glass envelope and Kovar part (small cylindrical part which is used as a junction between absorber and glass tubes) by radiation and lost through the support brackets by conduction as well. The heat loss coming from the absorber by radiation passes through the glass envelope by conduction and along with the energy absorbed by the glass envelope is lost to the environment by convection and to sky by radiation. Furthermore, conduction heat transfer occurs between glass envelop and Kovar part of the HCE. In addition, absorbed energy in Kavor part by radiation and conduction is lost to the environment by convection and to sky by radiation as well.

However, in in-door test set-up the heat source is cartridge heater inside the absorber tube instead of reflected solar energy by the mirrors. Figure 52 shows the heat transfer and thermal resistance model in a cross section at the HCE (receiver tube). Direct heating imposed to absorber tube by the means of Joule effect generated by a cartridge heater along the length of the absorber tube. The energy transferred to the absorber tube by convective and radiative heat transfer mechanism. Similar to outdoor condition, absorbed energy into the absorber is transferred to the glass envelope and Kovar part by radiation. Convection heat transfer cannot occur due to the high pressure vacuum (about 10^{-4} mbar) inside annulus of the receiver tube. The heat loss coming from the absorber by radiation is lost to the environment by convection and to surrounding (sky) by radiation. Transferred heat by conduction between glass envelop and Kovar part of the HCE and absorbed energy in Kavor part by radiation from absorber tube is lost to the environment by convection and radiation.

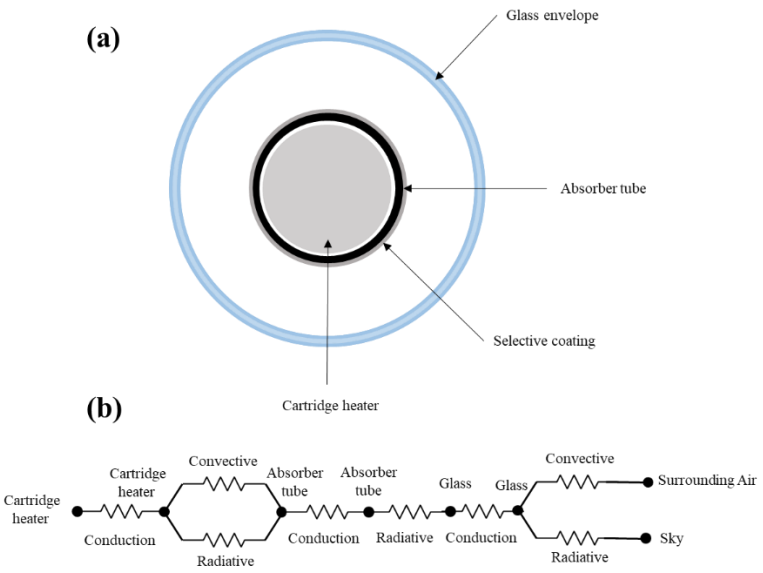

Figure 52. a) Cross section of the HCE b) Heat transfer mechanisms in cross section of the HCE.

Heat conduction (or diffusion) occurs as a consequence of different mechanisms in different media. Theoretically, it takes place in a gas through collisions of molecules; in a fluid through oscillations of each molecule in a "cage" formed by its nearest neighbors; in metals mainly by electrons carrying heat and in other solids by molecular motion, which in crystals take the form of lattice vibrations known as phonons [137].

In a continuous medium, Fourier's law of heat conduction states that the conductive heat flux (q) is proportional to the temperature gradient and can be described by equation (33).

$$q = -\mathcal{K} \cdot \nabla T \tag{33}$$

Where the k is the thermal conductivity (SI unit: W/(m·K)) and takes a positive value meaning that heat flows from regions of high temperature to low temperature and is the ∇T negative local temperature gradient [137].

Heat convection takes place through the net displacement of a fluid that transports the heat content with its velocity. The term convection (especially convective cooling and convective heating) also refers to the heat dissipation from a solid surface to a fluid, typically described by a heat transfer coefficient. Last but not least, Heat transfer by radiation takes place through the transport of photons. Participating (or semitransparent) media absorb, emit, and scatter photons. Opaque surfaces absorb or reflect them [137].

The Heat Transfer in solids interface solves for the equation (34) derived from equation (33).

$$\rho C_p \left(\frac{\partial T}{\partial t} + \boldsymbol{u}_{trans} \cdot \nabla T\right) + \nabla \cdot (\boldsymbol{q} + \boldsymbol{q_r}) = -\alpha T : \frac{dS}{dt} + Q \tag{34}$$

Where ρ is the density, C_p is the specific heat capacity, T is absolute temperature, $\boldsymbol{u_{trans}}$ is the velocity vector of translational motion, $\boldsymbol{q}$ is the heat flux by conduction and $\boldsymbol{q_r}$ is the heat flux by radiation, α is the coefficient of thermal expansion, S is the second Piola-Kirchhoff stress tensor

and Q contains additional heat sources. For a steady-state problem the temperature does not change with time and the terms with time derivatives disappear. Therefore the thermoelastic damping ($Q_{ted} = -\alpha T{:}dS/dt$) due to the thermoelastic effects in solids for a steady-state is equal to zero [137].

Surface to surface radiation (thermal radiation) takes place by the means of electromagnetic waves stream emitted from a body at a certain temperature. The total incoming radiative flux at point P located on a surface is called irradiation (G) and the total outgoing radiative flux is called radiosity (J). The body is assumed opaque, which means that no radiation is transmitted through the body. This is true for most solid bodies. The radiosity described by equation (35)(48) based on Stefan-Boltzmann law and is the sum of diffusively reflected and emitted radiation [137].

$$J = \rho_d G + \varepsilon e_b(T) \tag{35}$$

Where ε is the emissivity of the surface, ρ_d is diffuse reflectivity and $e_b(T)$ is the power radiated across all wavelengths. $e_b(T)$ is depends on the forth power of the temperature and can be described by equation (36) [137].

$$\varepsilon e_b(T) = n^2 \sigma T^4 \tag{36}$$

Where n is refractive index, T is temperature and σ is Stefan-Boltzmann constant equal to 5.67037442×10^{-8} $W{\cdot}m^{-2}{\cdot}K^{-4}$.

The convective heat transfer over the glass envelope can be described by equation (37).

$$Q_{Conv} = \pi D h_a (T_G - T_{amb}) \tag{37}$$

Where D is diameter of glass envelop, T_G is temperature of glass envelop, T_{amb} is ambient temperature and h_a is the convective heat transfer coefficient. h_a is defined as $Nu{\cdot}k_a/D$ and Nu is the Nusselt number (ratio of convective to conductive heat transfer at a boundary) and k_a is thermal conductivity of air [121,132].

The body is assumed opaque, which means that no radiation is transmitted through the body. This is true for most solid bodies. The net inward heat flux into the opaque body (q) based on G and T can be described by equation (38) [137].

$$q = (1 - \rho_s)G - J = \big(1 - (\rho_d + \rho_s)\big)G - \varepsilon e_b(T) \tag{38}$$

Where ρ_s is specular reflectivity. Most opaque bodies also behave as ideal gray bodies and for ideal gray bodies, q is given by equation (39).

$$q = \varepsilon(G - e_b(T)) \tag{39}$$

The heat transfer by radiation is combined with convective and conductive heat transfer through a source term added to the heat equation along with the other contributions from the heat flux and boundary heat source boundary conditions [137].

Recalling equation (38), this source account for the difference between incident radiation (irradiation G) and radiation leaving the surface (radiosity J). ε is a dimensionless number in the range $0 \leq \varepsilon \leq 1$. The diffuse-gray surface hypothesis corresponds to surfaces where ε is independent of the radiation wavelength. The irradiation (G), at a given point is split into three contributions according to equation (40).

$$G = G_m + G_{ext} + G_{amb} \quad \textbf{(40)}$$

Where G_m is the mutual irradiation, coming from other boundaries in the model, G_{ext} is the irradiation from external radiation sources and it is the sum of the products, for each external source, of the external heat sources view factor F_{ext} by the corresponding source radiosity and can be described by equation (41). Where The first term of the sum gathers radiation sources located on a point and the second term stands for directional radiative sources [137].

$$G_{ext} = \sum F_{ext} P_s + \sum F_{ext} q_{0,s} = \quad \textbf{(41)}$$

G_{amb} is the ambient irradiation and defined by equation (42).

$$G_{amb} = F_{amb} e_b(T_{amb}) \quad \textbf{(42)}$$

Where F_{amb} is an ambient view factor and its value is equal to the fraction of the field of view that is not covered by other boundaries. Therefore, by definition, $0 \leq F_{amb} \leq 1$ at all points. T_{amb} is the assumed far-away temperature in the directions included in F_{amb}[137].

Diffuse Surface (Surface-to-Surface Radiation interface) is the default radiation type. It requires accurate evaluation of the mutual irradiation (G_m). The incident radiation at one point on the boundary is a function of the radiosity (J) at every other point in view. The radiosity is a function of G_m, which leads to an implicit radiation balance (Equation (43))[137].

$$J = \rho_d(G_m(J) + G_{ext} + G_{amb}) + \varepsilon e_b(T) \quad \textbf{(43)}$$

In order to increase storage and computational savings, adaptive mesh refinement (AMR) with different mesh configurations for the model has been conducted. The parameters reported in Table 27 control the mesh element size (the parameters define a size use the geometry's length unit). Maximum element size limits the allowed element size, Minimum element size specifies the minimum allowed element size, maximum element growth rate determine the maximum rate at which the element size can grow from a region with small elements to a region with larger elements. The value must be greater or equal to one. For example, with a maximum element growth rate of 1.5, the element size can grow by at most 50%. Curvature factor determines the size of boundary elements compared to the curvature of the geometric boundary (the ratio between the

boundary element size and the curvature radius). The curvature radius multiplied by the curvature factor, which must be a positive scalar, gives the maximum allowed element size along the boundary. A smaller curvature factor gives a finer mesh along curved boundaries. The mesh quality gives an indication of the length to width ratio of specific mesh elements, for a homogeneous material and shape a regular mesh of quality close to 1 is mostly ideal. The solution time and memory requirements are strongly related to the number of degrees of freedom (DOFs) in the model. It is often desirable to be able to estimate the number of degrees of freedom based on the number of elements in the model. For most physics interfaces each dependent variable is present in all nodes in the mesh. This means that the number of degrees of freedom is given by the number of nodes multiplied by the number of dependent variables. The relation is only approximate since it depends on the ratio of the elements that lie on the boundary of the geometry [138]. Figure 53 shows two different configurations at inlet of the receiver tube based on reported parameters in Table 27. The model simulated with refined mesh having 77452 degrees of freedom (base mesh of C) showed more accurate temperature distribution along the absorber tube. The relative deviation in average temperature of the absorber tube from experimental result at low temperature (Tave = 30°C) for base mesh of A, B, C and D are 10.1%, 4.0%, 3.8% and 3.8%, respectively. Furthermore, main variables obtained from simulation including average temperature of absorber tube and the values of TC1-TC5 are stable and almost independent from mesh configurations between base mesh of C and D by imposing the above mentioned boundary conditions. The relative deviation in average temperature of absorber tube is small (0.02%) between base mesh of C and D. Therefore, due to the higher number of elements, lower minimum element quality, uniform results and higher average element quality base mesh of C has been used to solve the model.

The mesh element quality is a dimensionless quantity between 0 and 1, where 1 represents a perfectly regular element, in the chosen quality measure, and 0 represents a degenerated element. The skewness factors is the default quality measure in COMSOL Multiphysics and it is a measure of the equiangular skew is defined as the minimum of the quantity presented in equation (44) [138].

$$1 - \max\left(\frac{\theta - \theta_e}{180 - \theta_e}, \frac{\theta_e - \theta}{\theta_e}\right) \quad \textbf{(44)}$$

Where θ is the angle over a vertex (2D) or edge (3D) in the element, θ_e is the angle of the corresponding edge or vertex in an ideal element, and the minimum is taken over all vertices (2D) or edges (3D) of the element.

Table 27. Mesh refinement parameters for different mesh configurations.

Mesh	Maximum element size	Minimum element size	Maximum element growth rate	Curvature factor	Number of Elements	Minimum Element Quality	Average Element Quality	Degrees of freedom (DOFs)
A	127	0.57	1.3	0.3	29861	0.3024	0.7022	71136
B	38	0.143	1.2	0.25	30517	0.3105	0.6939	73114
C	19	0.038	1.1	0.2	32249	0.3071	0.7122	77452
D	8	0.001	1	0.15	1501512	0.6229	0.9407	83114

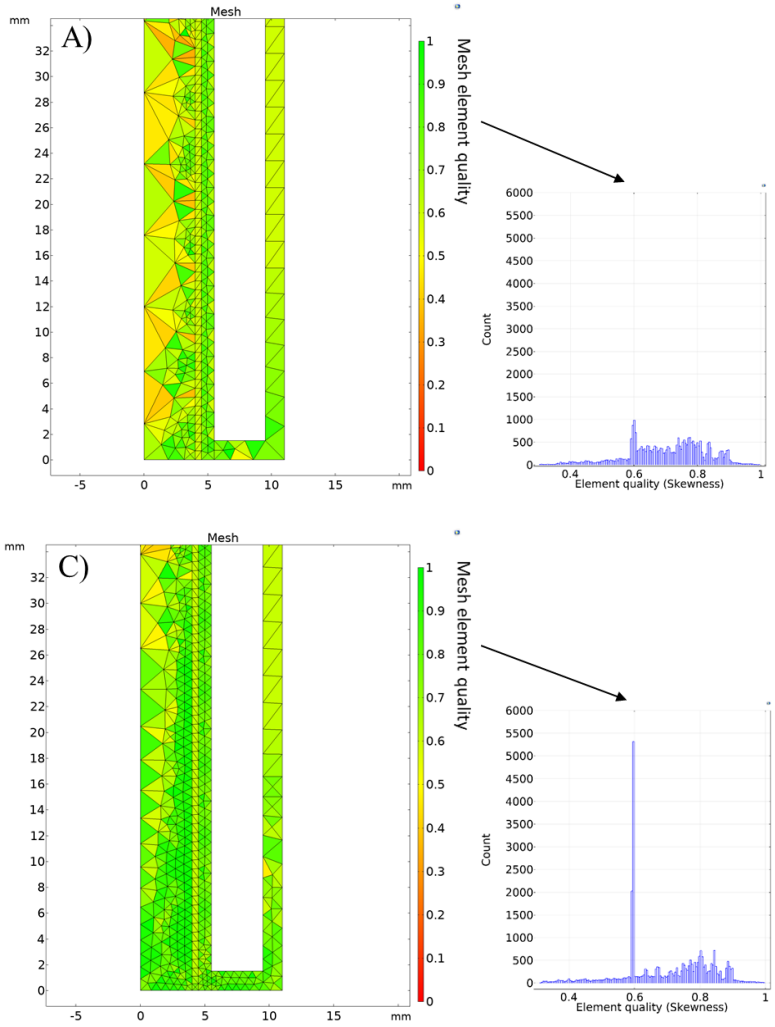

Figure 53. Base A and base C mesh configurations of the model based on Skewness quality measure and their related mesh element quality histogram.

3.3 - Emissivity Retrieval from FEM Model

The steel absorber tube with a selective Cermet coating has emissivity of 0.12 (provided by the manufacturer of the receiver and verified by the group of research with a spectrophotometer) for λ>2.5 μm at ambient temperature. The heat transfer model is able to precisely predict the heat losses at low temperature ($T_{ave} \leq 50°C$) of the absorber temperature with constant value of emissivity. Figure 54 shows comparison of temperature distribution along the absorber tube obtained by the simulation and by experiment at T_{ave} = 30°C. The results indicate that the difference of average temperature of absorber tube obtained by simulation and experiment is less than 1°C and obtained values for each thermocouple (TC1-TC5) from simulation are inside the uncertainty range of each sensor. Temperature contours of solar receiver in-door test is shown in Figure 55 for test at ambient temperature. In addition, Figure 56 shows average temperature inside the absorber tube obtained from experimental test points and related simulation results. For all points, the difference of average temperature of absorber tube in the model and during the test is less than 1.5°C and therefore simulation points are inside the error bar of the experimental points.

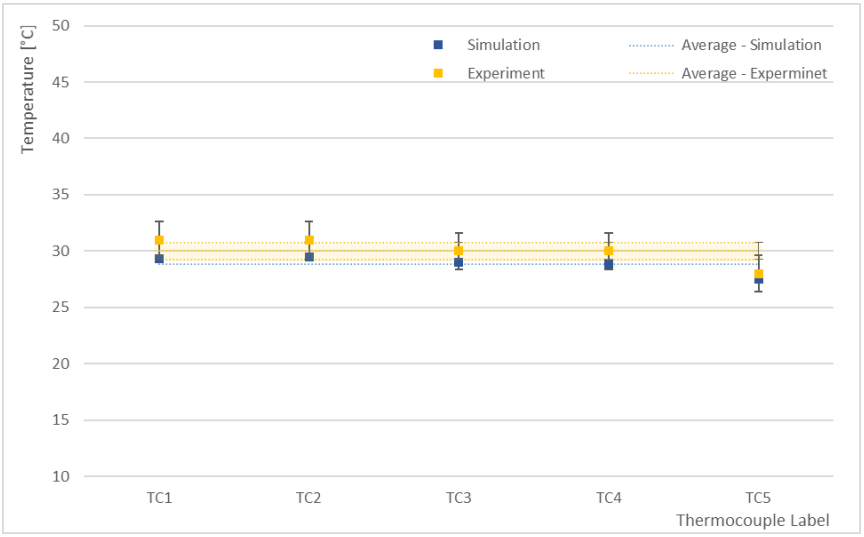

Figure 54. Comparison between experimental and simulation results for test at low temperature.

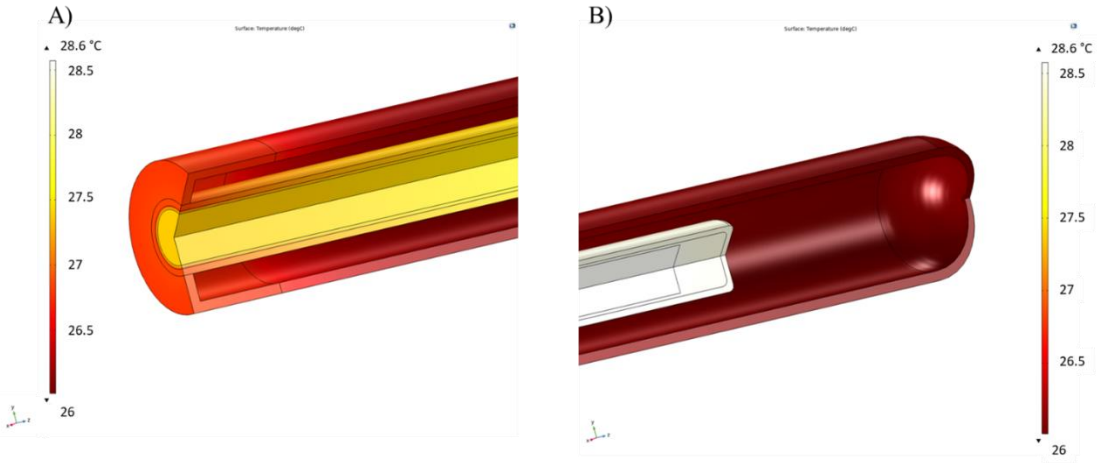

Figure 55. Temperature contours at A) inlet and B) end of the solar receiver in-door test.

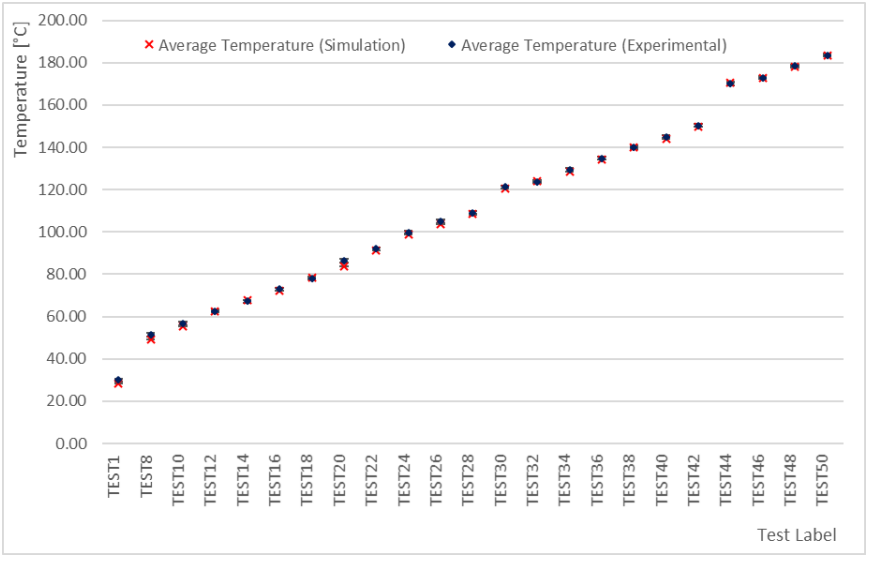

Figure 56. Average temperature inside the absorber tube obtained from experimental and simulation results.

The emissivity of coating on absorber tube rises with the temperature of the coating and this change is more noticeable in higher average temperature of the absorber coating. In order to obtain the estimation of emissivity at the higher temperature, the model has been solved with various emissivity values for each test at specific input power until the average temperature inside the absorber tube (T_{ave}) obtained by simulation were in agreement with experimental value. The maximum difference between these values is under 1.5 °C. Figure 57 shows the variation of emissivity with average temperature inside absorber tube obtained from simulation. As mentioned before, the emissivity at ambient temperature is 0.12 and the variation of emissivity with temperature can be described by equation (45). The R squared (R^2) vale is 0.95 and defined as the coefficient of multiple determination for multiple regression.

$$\varepsilon = 3.13 \cdot 10^{-4} \cdot T_{ave} + 1.095 \cdot 10^{-1} \quad \textbf{(45)}$$

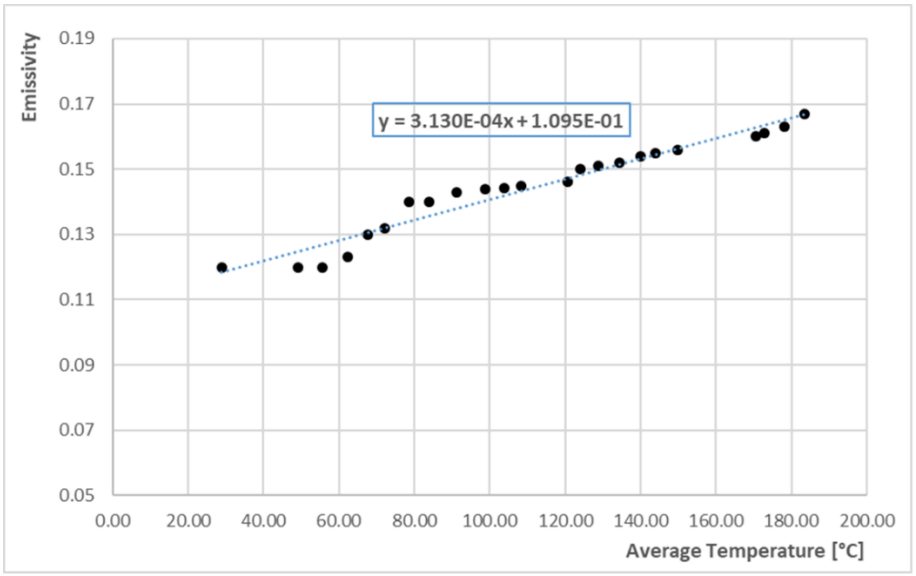

Average Temperature	Emissivity
29	0.12
49	0.12
55	0.12
62	0.123
68	0.13
72	0.132
79	0.14
84	0.14
91	0.143
99	0.144
104	0.1441
108	0.145
121	0.146
124	0.15
129	0.151
134	0.152
140	0.154
144	0.155
150	0.156
171	0.16
173	0.161
178	0.163
183	0.167

Figure 57. Emissivity of absorber coating with average temperature inside absorber tube.

Equation (45) has been used as a emissivity function in model in order to solve the model for various input power values. The obtained results from simulation confirmed that the model and emissivity function are able to predict the thermal loss with high accuracy. Figure 58 shows the comparison of heat loss values obtained from experimental and simulation as a function of ΔT (difference between the average absorber tube temperature and ambient temperature) for RT01.

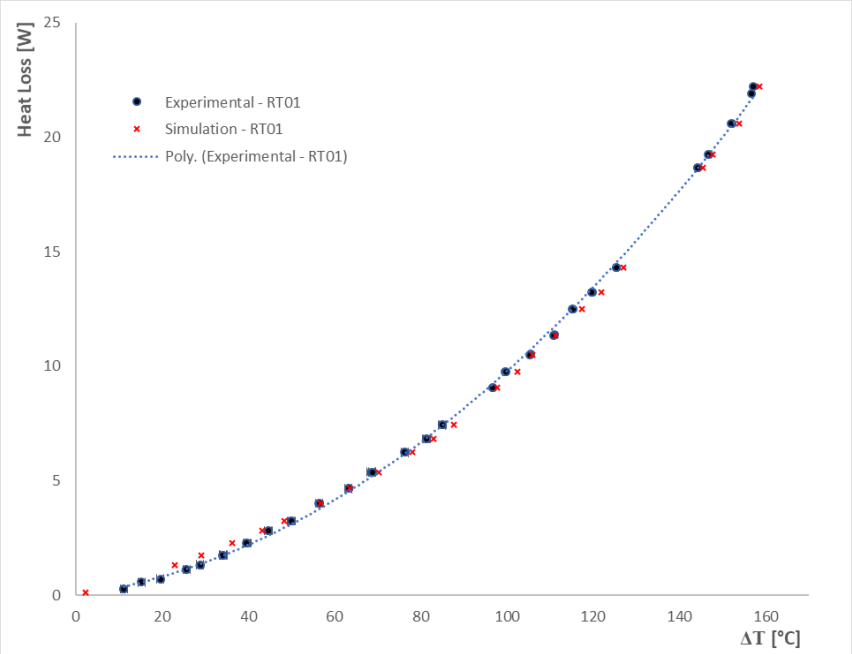

Figure 58. Comparison of heat loss values obtained from experimental and simulation as a function of ΔT for RT01.

4 - Characterization and Efficiency Test of the m-PTC

As mentioned before, concentrating collectors could be the right technology to produce heat at medium temperature to provide thermal energy to users that require temperatures between 85 and 250°C. Users with high consumption rates and low-temperature heat demand like domestic hot water and space heating in addition to the industrial process heat applications like ironing, cleaning, drying, sterilization, etc. are the main medium temperature users [31–33]. However, IEA reported on December 2015 that 0.3% of total installed solar thermal capacity (about 88MWth) is related to the solar heat for industrial processes [29].

Energy can be provided by flat plate and parabolic trough collectors (PTC) depending on requested temperature [139]. Low temperature collector is commercially available today and reached a high level of development. Flat plate and evacuated tube collectors in the market are able to operate at maximum temperature of 80 and 200°C, respectively [21]. While the parabolic trough collectors are able to operate up to 400°C [31].

An Ultra high vacuum flat plate collector was developed by SRB Energy Company in Spain and Switzerland with maximum operation temperature of 200°C. In Geneva (Switzerland), a thermal vacuum power charged flat plate collector was developed at TVP solar Company. Width and length of the aperture are 69.1 and 169.1 cm, respectively. The heat transfer fluid is pressurized hot water with maximum operation temperature of 200°C [29]. Ultrasonic welding technique has been used in industries for advance flat plate collectors in order to improvement in heat conduction rate [16]. In general, non-concentrating flat plate, evacuated tube and compound parabolic collectors are used in industrial air and water systems for low temperature application by temperature range of 60 up to 180°C.

Soliterm Group in Aachen (Germany) presented series of PTC for medium temperature application. Aperture width of Soliterm 1100, 1800, 3000 and 4000 are 110, 180, 300, 400 cm, respectively. Apart from Soliterm 1100, maximum operation temperature of other models is 250°C. For industrial processes and solar refrigeration a PTC was developed at Inventive Power Company in Mexico, aperture width, aperture length, maximum operation pressure and maximum operation temperature of this system are 110 cm, 300 cm, 15 bar and 200°C, respectively. Trivelli Energy SLR in Italy developed a PTC with aperture width of 125 cm and maximum operation temperature of 250°C for process heat and solar cooling application at maximum operation pressure of 16 bar. For higher operation temperature and pressure (maximum of 288°C and 40 bar) a PTC with aperture width of 230 cm was developed at Abengoa Solar Company in Spain. Also another PTC with aperture width of 114 cm was developed at this company to operate at 30 bar and 205°C. SL2300 and SL4600 PTC were developed in Solarlite CSP Technology Company to operate at maximum temperature of 200 and 400°C for food & beverages, paper, textiles and fabrication metal industries [29].

Due to the space limitation in industrial environments, design and development of the compact solar thermal energy systems is important. Over recent years, few small size parabolic trough collectors have been developed [11]. A small size PTC collector was developed during the CAPSOL project in collaboration with the University of Almeria. Aperture width and total length are 1 and 2 m, respectively. Maximum operation temperature for this system is 250°C. The dimension of this system are compatible for domestic and industrial application [140]. O. A. Jaramillo et al. [139], studied performance of parabolic trough solar collectors named PTC 45 and

PTC 90. Reported thermal efficiency in an open loop and in a closed loop form of the mentioned PTC system are 29% and 43%, respectively. J. Macedo-Valencia et al. [141], studied a PTC system with the parabolic aperture of 0.95m long and 0.5m wide. The efficiency during clear and partly cloudy weather condition is 50.7% and 36.49%, respectively.

J.-L. Bouvier et al. [142], reported small size PTC (46.5 m^2) with two axis tracking system for direct steam generation as a Micosol project (Micro solar CHP). Obtained thermal efficiency for this system with steam is around 50% and suitable for coupling with the steam engine. I. H. Yilmaz et al. [143], studied thermal performance of the parabolic trough collector array for a small-scale process heat application in agreement with ASHRAE 93-1986 standard and the maximum efficiency is 57%. G.Q. Chaudhary et al. [144], studied small size PTC system with aperture area of 2.077 m^2 integrated with a solid desiccant dehumidifier (SDD) for solar air-conditioning applications. Maximum thermal energy gain and peak efficiency for this system on a sunny day are 3.07 kW and 62%.

M. Yang et al. [145], designed a micro-parabolic trough solar collector for building integration. Optical and thermal performance of proposed collector were determined theoretically, experimentally and the incident angle modifier and normalized thermal efficiency curve were reported. Reported annual optical efficiency is 67% and the instant thermal efficiency is 59% at 200 °C. However, installed micro PTC on building's facade (31° latitude) shows thermal efficiency of 37.5% at 200 °C.

In order to address the problem of area limitation in industries, a small size parabolic trough collector (called m-PTC) has been developed in Department of Industrial Engineering of Florence University to produce heat at low-medium temperature (up to 200°C).

The information on the thermal performance of a solar thermal collector is important for the prediction of the energy output of any solar thermal system. Several standards are presented for test procedure on concentrating solar collector, such as ASHRAE 93 [146], EN 12975-2 [147], ISO 9806:2017 [148], ASTM E905-87:2013 [149] and SRCC 600 2014-07 [150]. However, the SRCC 600 2014-07 standard refers to ISO 9806 standard in relatively high similarity. Mentioned standards propose two different test approaches for characterizing the thermal performance of solar thermal collectors: The steady state test (SST) and the quasi-dynamic test (QDT) [98]. In SST, all important parameters for the thermal performance remain constant in the range of permitted value by the standard during the test period and test has to be performed under clear sky condition (low percentage of diffuse radiation). As a result, in obtained model by SST method there is no correction term for the diffuse radiation [98,147,151]. However, obtained model in QDT method is more detailed about description of collector and drives from SST model by adding some correction terms (wind speed and radiation of long wavelength incident on the collector should be considered). In this method, test has to be performed under varying sky conditions for at least 3 h [98,147,148,150]. Both methods lead to a same principle. Therefore, there are no arguments to choose between these methods [152].

Developed novel solar collector (SC) suitable to be integrated in the roof of industrial environments where the space for installation of solar collectors is in general limited and the heat demand temperature is below than 200°C. Preliminary study has been conducted in this laboratory to validate the test bench and calibrate the control systems [153]. In this chapter, the design, realization and detailed experimental efficiency study of this m-PTC test rig is presented.

4.1 - Design of the test stand for solar collector

4.1.1 - Design of the small size receiver tube and the concentrating system

The development of the novel PTC started from the design of the receiver tube where the Sun light is concentrated. The thermophysical analysis and the process to define the technical specs is reported on previous work with computational modelling and simulations [154]. The receiver is formed by two coaxial steel tubes covered by a glass envelope (Figure 59). The inlet and outlet of the heat transfer fluid are at the same side obtaining a counter-current flow mechanism as a result. The coaxial tubes layout brings some advantages in terms of feasibility, durability and cost reduction. That is due to the presence of only one metal to glass junction while in the opposite side the glass is sealed on itself. Consequently, the number of expensive components is halved (as well as well the manufacturing process becomes easier) and the vacuum condition is guaranteed in time by minor critical points of the geometry).

The outer absorber tube is made of steel and has a diameter of 10 mm (1 mm thickness) for a length of 1860 mm; the smaller coaxial tube is made of steel and has an internal diameter of 6 mm (0.5 mm thickness). It is worthwhile to mention that, a selective coating (Cermet coating, α=0.94 and ε=0.12 at ambient temperature) has been selected to reduce the emission in infrared range and increase the energy absorption in solar spectral range.

The absorber tube is covered by a glass envelope coated by AR layer to prevent reflection of the solar radiation. Inside, a vacuum level is fixed at 10^{-4} mbar. In order to keep the internal tube aligned in the reflector focus, four springs support are inserted. At the beginning of the tube, a small cylinder of Kovar allows the metal to glass junction and outlet is welded on a plug.

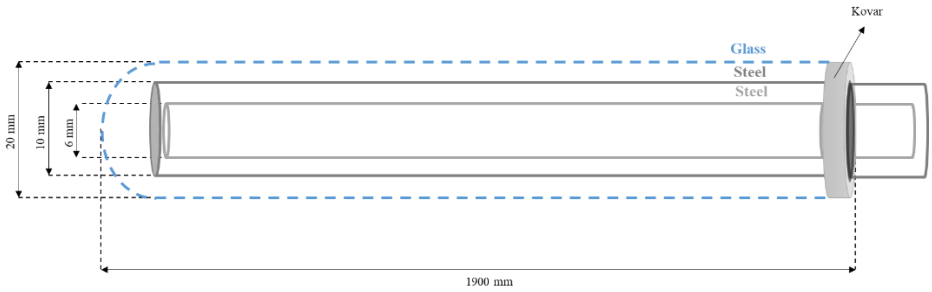

Figure 59. The scheme of the One-End receiver tube for m-PTC.

Four receiver tubes are placed in the focus of parabolic mirrors that are assembled close to each other aiming at the realization of a modular structure (Figure 60). The mirrors has an aperture area of 0.756 m^2 (width of 0.42 m and length of 1.8 m) and a rim angle of 100° was fixed in order to increase the acceptance angle and reduce the effect of optical errors, according to a previous study [155]. In this configuration, the rays are collected into the absorber if they reach the collector aperture with an angle inside ±1.5° in respect to normal direction. The reflective surfaces are made of thin anodized aluminium layers with a value of specular reflectivity of 0.89.

The movement of the concentrators is obtained with two linear commercial actuators that push, from both the module sides, a metal bar connected to hinges placed below the parabola's vertexes. Therefore, the mirrors are integral each other and rotate around the receiver tubes which are fixed instead.

The motors are supplied in direct current with a pulse-width modulation (PWM) that allows changing in position by steps up to a minimum value of 1 mm.

The tracking is mono-axial such as in the common parabolic trough systems layout and the collector accepts both N-S and E-W orientation: for the test, the last one was preferred reducing the daily rotation angle range and the mutual shadowing effect of mirrors since the motors has to compensate only the Sun elevation path.

Figure 60. The M-PTC module from one side.

The tracking method is preliminary managed by an algorithm based on ephemerides equations which were implemented in Arduino+Pyton environment; the angle position of mirrors is derived and controlled as a direct function of the motors' extension. This procedure let the start-up of plant and the continuous Sun tracking during the day also in variable conditions due for instance to the presence of clouds. A more precise alignment of the concentrators is guarantee thanks to a specific 2-quadants sensor, developed for this application. As can be seen in Figure 61 (a), two calibrated small phodetector (2x2 mm2) are mounted on a board, separated by a thin black flag made of plastic. Until the both elements are equally lighted up, their output signals have the same value; as soon the flag generates a shadow on the support (it is to say that the mirror aperture is not normal to the Sun rays) the output signals are not balanced, the control system based on Arduino (Figure 61 (b)) recognises a misalignment and imposes the necessary steps to the motors for repositioning, with a proportional-integral-derivative (PID) regulator. Based on a previous analysis, the overall

accuracy of the tracking procedure using the sensor, was found to be under 0.1° in respect to the instantaneous ideal direction along the full span.

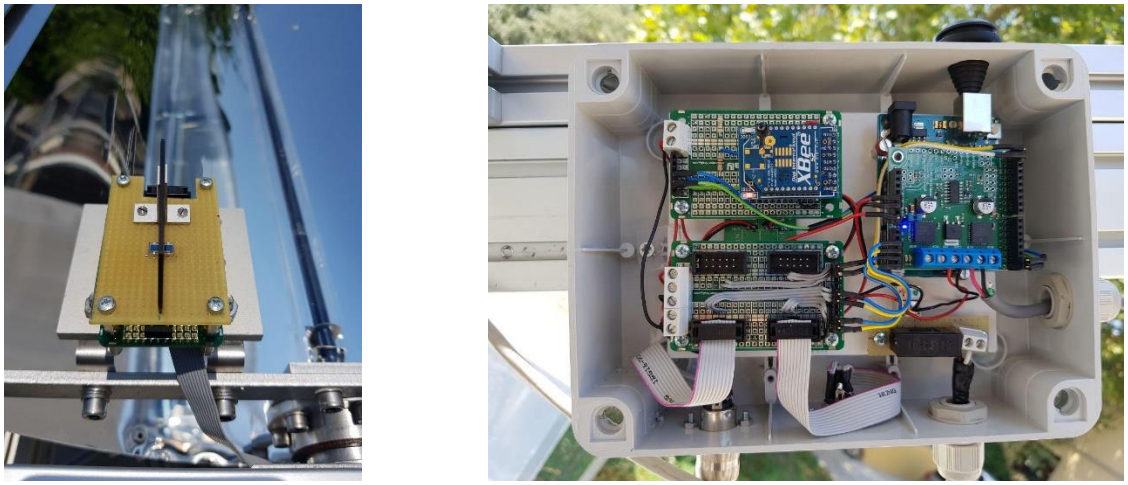

(a) (b)

Figure 61. (a) Sun positioning sensor. (b) Arduino platform to monitor the sensor and supply the linear actuators.

To record the measured values from the sensors, commercial data logger (dataTaker DT80) has been used during the test. It has been programmed with LabVIEW environment to manage all the acquisition and data recording process. A customized graphical user-interface (Figure 62) has been developed properly and used to real time monitoring of cold and hot circuit with the display of the main parameters and possible alarms.

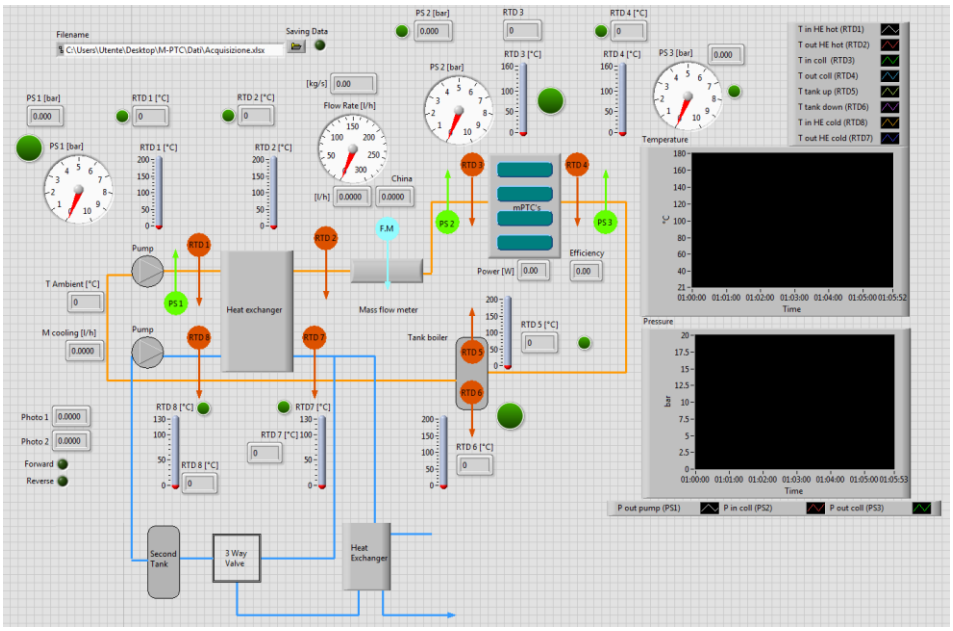

Figure 62. The graphical user-interface for monitoring the test rig in LabVIEW developed in DIEF.

4.1.2 - The test rig platform

In order to test the module according to ISO 9806:2017 [148], an Alt-Azimuth platform were designed and built with a rigid aluminium frame and a usable area of 7 m^2 (Figure 63).

The structure could be tilted in respect to the horizontal plane with two fixed bars which let to place frame manually at an adjustable angle in the range 0-45°. In combination of that feature, if the module is set in E-W orientation, the collector control system could guarantee the Sun tracking in elevation avoiding mutual mirrors' shadowing.

The platform is also equipped with a flat rail where the frame could rotate around a vertical axis: it permits the Sun azimuthal tracking during the day zeroing the incident angle modifier effects. The movement is automatically managed thanks to a gear-motor with an encoder supplied by inverter.

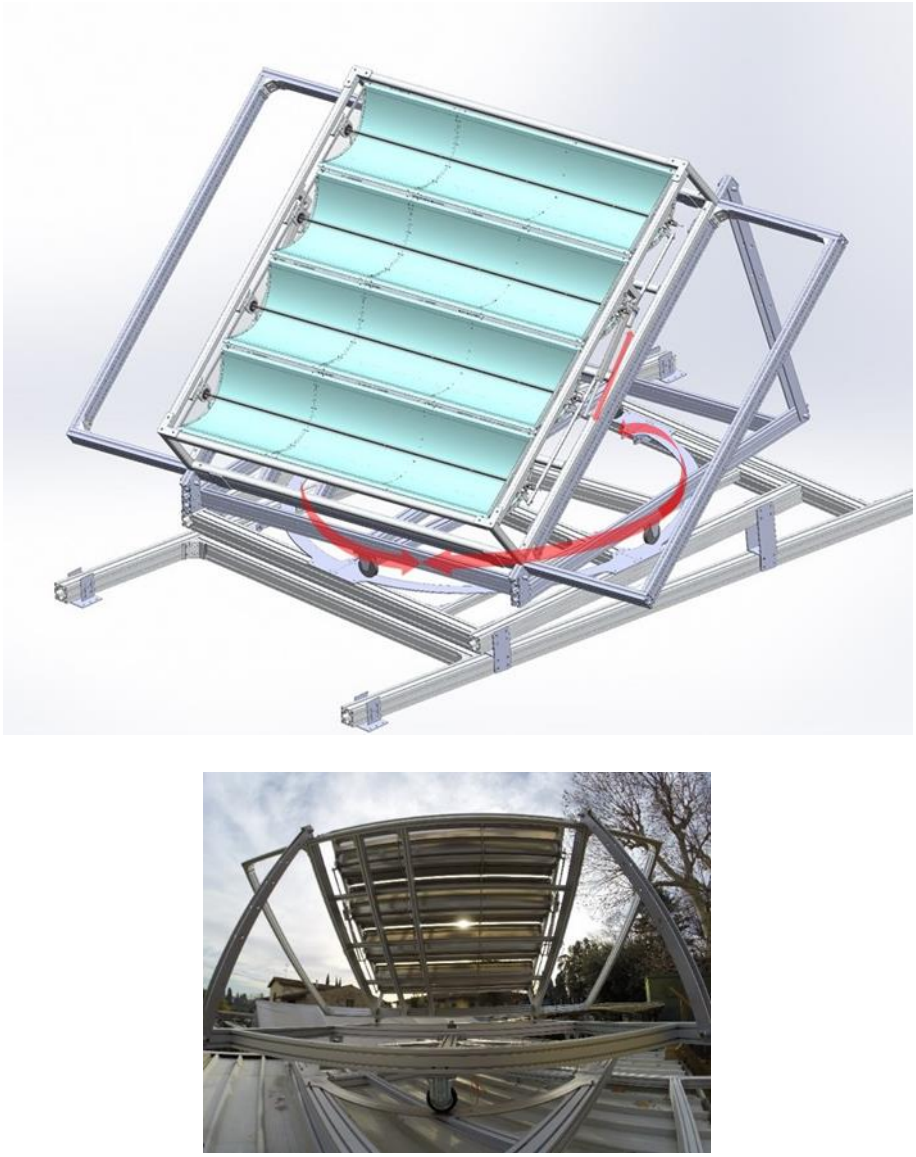

Figure 63. The scheme of the Alt-Azimuth platform.

4.1.3 - Design of the hydraulic circuit

The m-PTC module is tested under ISO9806 steady-state operative conditions [148] and a specific test rig was implemented. Figure 64 shows piping and instrumentation (P&I) of the test stand, highlighting a hot and cold circuit with red and blue color, respectively. Hot circuit is divided by main heat exchanger (Cooler in P&I layout) from cold circuit. The solar collector is connected to the hot circuit and works with pressurized hot water at medium temperature (up to 200°C and 16 bar). On the other side, the cold circuit matched to control the inlet temperature constant, keeping it stable during test. Its components are supposed to work in less stressful conditions (maximum 10 bar and 130°C).

In hot circuit the pumped water, reaches the solar collector under test, after passing through the main heat exchanger (Cooler). A sliding vane pump (Pump1 in P&I layout, maximum 250 l/h) is selected for circulating the heat transfer fluid and a Coriolis flowmeter is installed downstream for measurement. The electrical power of the heater needed to heat the water from 20°C to 190°C can be derived by equation (46).

$$\dot{Q}_{heating,elec.trical} = \frac{\frac{V_w \rho_w C_{P,w} \Delta T_w}{\Delta t} + \frac{V_{tank} \rho_{tank} C_{tank} \Delta T_{tank}}{\Delta t}}{\eta_{heat}} \quad \textbf{(46)}$$

Where V_w and V_{tank} are the volume of water and tank to be heated and the values are 0.05 m^3 and 0.01 m^3, respectively. Δt is the required time to heat up the water and the tank and the value is 90 min. ΔT_w and ΔT_{tank} are the temperature increase in the water and values are 120°C. Material properties are evaluated at the average of 20°C, 1 bar and 190°C, 15 bar. By this values the required power of the electric heater is about 8 kW. Therefore, A 9 kW electric resistance heater inside a 50 l expansion tank (consist of 9 electric resistance of 1 kW) is used to warm up the heat transfer fluid quickly by Joule effect and run test at different temperature levels. The circuit pressure controlled by a discharging security vale under 10 bar.

The maximum gained thermal heat by collector ($Q_{Gain_{max}}$) can be derived by equation (47) and the cooling power to balance the thermal power gained by the water of the main circuit in the collectors has to be equal to it.

$$Q_{Gain_{max}} = \eta_{th} \cdot DNI \cdot A_{net} \quad \textbf{(47)}$$

Where η_{th} is thermal efficiency (0.75), DNI is direct solar radiation (1000 W) and A_{net} is net area of the collector (2.856 m^2). Therefore, the maximum gained thermal heat by collector is 2150 W.

In cold circuit, a 3-way modulating valve automatically set the SC inlet temperature trough a PID controller (Figure 65). The 3-way valve manages mass flow by magnetic actuators imposing two different hydraulic branches: one is connected to cold sink (a water main bowl) and the other is a direct re-circulation. Depending on the collector inlet temperature gradient, the controller decides the amplitude of splitting for the optimal temperature value of mixed water after the valve. The feedback parameter is sent by a RTD Pt1000 sensor, which is placed at the inlet of SC. In addition,

another sliding vane pump (Pump2 in P&I layout) has been selected for circulating the water in cold circuit, with maximum flow rate of 33.4 l/min

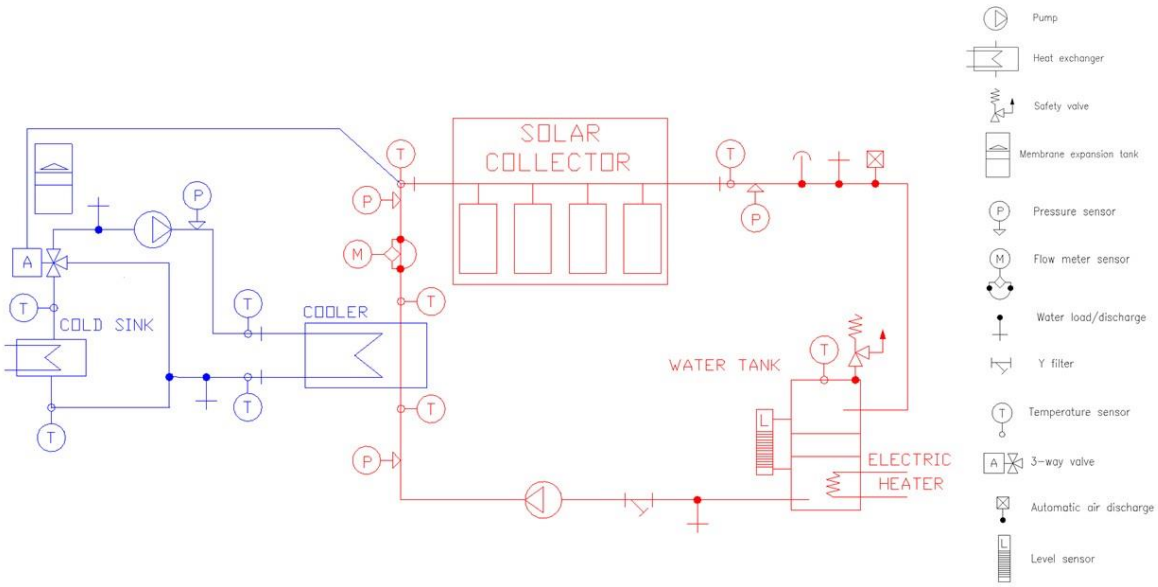

Figure 64. Hydraulic circuit Layout and Instrumentation of the test rig.

Figure 65. The 3-way valve mounted in cold circuit.

4.1.4 - Details of Measurement Devices

As mentioned before, in order to measure the test reference parameters several sensors are placed in circuit. Moreover, meteorological data are measured by a two axes weather station (Figure 66) installed on a roof, near to the test bench. It includes a pyrheliometer, two pyranometers, a thermos-hygrometer and an anemometer respectively for the measurement of direct, global and diffused radiation, outdoor temperature and humidity, wind direction and intensity. The features of overall sensors and devices for recording the measurement values are listed in Table 28.

Figure 66. Weather station.

Table 28. Information of test stand measurement equipment.

Device	Type	Accuracy	Description
Temperature sensor	RTD Pt100	0.03°C	Placed in the inlet of collector
Temperature sensor	RTD Pt100	0.03°C	Placed in the outlet of collector
Temperature sensor	RTD Pt1000	0.15+0.002·T	Provide signal for 3-way valve
Temperature sensor	RTD Pt100 1/10 DIN	0.05°C	Ambient temperature
Pressure sensor	Membrane transducer	0.25%	Measurement range 0-15 bar
Mass Flowmeter	Coriolis	0.09%	-
Sun Tracker	Fully automatic sun tracker with integrated GPS at BSRN level	<1%	Accuracy related to first class pyrheliometer
Data Acquisition	Real time Multiplexer for different I/O signals	depending on the signal	Acquisition frequency 3s

4.2 - Experimental results of outdoor test

According to ISO9806 :2017 (substitution for EN 12975-2) standard, in order to evaluate the thermal performance of the small-size parabolic trough collector the SST method has been selected. Since both SST and QDT methods lead to a same principle and SST method requires less parameters to be measured during the test. In order to carry out the SST method, one need is to ensure that all relevant parameters for the thermal performance remain constant in the range of permitted values by the standard, through the measurements. Furthermore, the test has to be performed under a clear sky condition (with low percentage of diffuse radiation). As a result, a model obtained by SST method has no correction term for the diffuse radiation and in this method normal incidence radiation is used to define the parameters of the efficiency curve [98,147,151].

By contrast, the QDT method requires less intervention from the operator and to successfully carry out the QDT, less sunny days are requires than for the SST method [151]. In addition, QDT method is more detailed and complex about description of collector in comparison to the SST method by adding some correction terms (wind speed and radiation of long wavelength incident on the collector should be considered in some collectors).

Table 29 presents proposed test conditions and the permitted deviations from average values by ISO 9806:2013 based on QDT and SST method.

Table 29. Test conditions and permitted deviations from average values base on QDT and SST method.

Variable	QDT method		SST method	
	Value	Deviation	Value	Deviation
Global radiation G[W/m^2]	-	-	>700	±50
Incidence angle θ[°]	-	-	<20	-
Diffuse fraction G_d/G [%]	-	-	<30	-
Ambient temperature T_a [K]	-	-	-	±1.5
Wind speed u[m/s]	1<u<4	-	2<u<4	-
Inlet temperature T_{in}[K]	-	±1	-	±0.1
Mass flow rate $\dot{m}$ [kgs^{-1}m^{-2}]	0.02	±1%	0.02	±1%

Equation (48) shows thermal efficiency (η_{th}) and it is defined as the ratio of useful gained heat by the heat transfer fluid (Q_{out}) and direct solar radiation (*DNI*) incident in net aperture surface of the collectors (A_{net}) [156]:

$$\eta_{th} = \frac{Q_{out}}{DNI \cdot A_{net}} \quad \textbf{(48)}$$

The amount of gained heat defined by the heat transfer fluid as equation (49):

$$Q_{out} = \dot{m} \cdot C_p \cdot (T_{out} - T_{in}) \text{ [W]} \quad \textbf{(49)}$$

where $\dot{m}$ [kg/s] is the mass flow rate, C_P [J/kg°C] is the specific heat capacity at constant pressure, A_{net} is about 0.705 m^2 for one collector, T_{out} and T_{in} [°C] are the outlet and inlet temperature of the heat transfer fluid to the collector, respectively. In addition, by considering the clear sky condition and the diffuse radiation contribute negligible, the heat balance equation based on the SST model can be described by equation (50).

$$\frac{Q_{out}}{A_{net}} = \eta_0 \cdot \mathrm{K}(\theta) \cdot \mathrm{DNI} - a_1(T_m - T_a) - a_2(T_m - T_a)^2 \quad \textbf{(50)}$$

Where Q_{out} [W] is useful power extracted from collector, η_0 is zero-loss collector efficiency when (T_m-T_a) = 0, $K(\theta)$ is the incidence angle modifier (angular dependence of the optical performance), a_1 [Wm^{-2}K^{-1}] and a_2 [Wm^{-2}K^{-2}] are temperature dependent heat loss coefficient, T_m and T_a [°C] are the mean temperature of heat transfer fluid and ambient air temperature, respectively [98]. The general point of the test is extracting the efficiency curve of the collector for normal incidence based on the coefficients η_0, a_1 and a_2.

Looking at the thermal collector model under the QDT procedure, the Quasi-Dynamic thermal collector model equation as adapted by the ISO 9806:2013 can be identified by equation (51).

$$\frac{\dot{Q}}{A} = \eta_{0,b}K_{\theta b}(\theta_L,\theta_T)G_b + \eta_{0,b}K_{\theta d}G_d - c_1(T_m - T_a) - c_2(T_m - T_a)^2 - c_3u(T_m - T_a) + c_4(E_L - \sigma T_a^4) - c_5\frac{dt_m}{dt} - c_6uG \quad (51)$$

In this model, c_1 is the heat loss coefficient at $T_m - T_a = 0$, c_2 is the temperature dependence of the heat loss coefficient, c_3 is the wind speed dependence of the heat loss coefficient, c_4 is the long wave irradiance dependence of the heat loss coefficient, c_5 is the effective thermal capacitance and c_6 is the wind speed dependence of the zero loss efficiency [148,157].

4.2.1 - Preliminary Test on m-PTC

Figure 67 shows recorded test parameters as a function of time (10 min) during clear sky day at 20.6°C average inlet temperature. The graph shows that the variables (inlet temperature, mass flow rate and direct normal irradiance (DNI)) are stable during the test interval; as a result, the system operates in steady state condition. During the test interval, the average value of DNI, mass flow rate and ambient temperature are 714 W/m^2, 29.6 Kg/h and 29.1°C, respectively. The deviation of ambient temperature, inlet temperature and mass flow rate should be less than ± 1.0°C, ± 0.1°C and ± 1.0%, respectively. During the test interval, the deviation of DNI, ambient temperature, inlet temperature and mass flow rate from average value are 1.37%, 0.19°C, 0.1°C and 0.66%, respectively. Therefore, the test stand meets the requirement of SST method and all the variables respect the imposed limitations. There is not any permitted value for DNI in EN 12975-2 standard based on SST method. However, based on ASTM E905-87:2013 standard in Quasi-SST method, the DNI value should be higher than 630 W/m^2 and the deviation should be less than ± 4%.

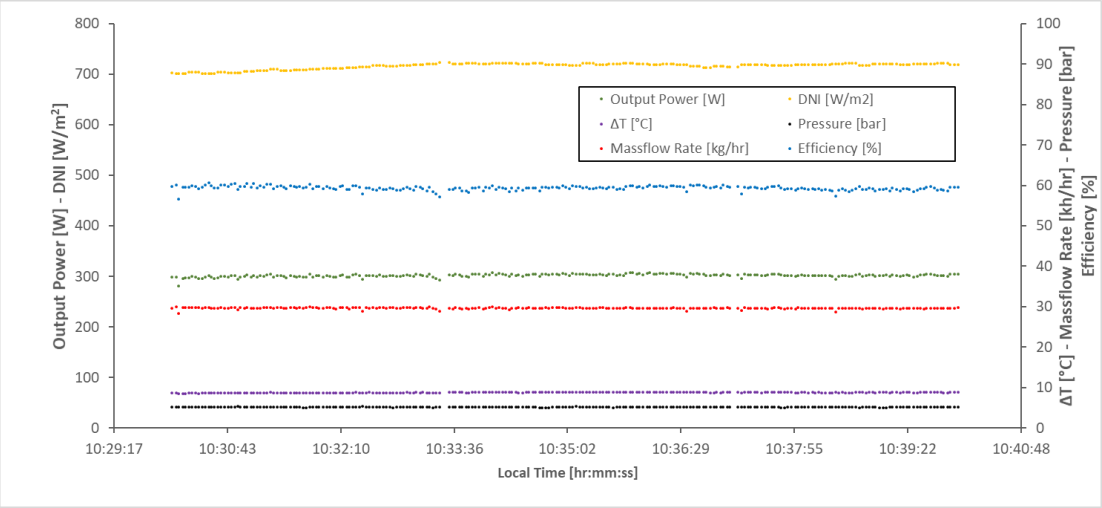

Figure 67. Test parameters as a function of time.

4.2.2 - Peak Optical Efficiency Test

During the peak optical efficiency measurement the collector must kept in normal incidence to avoid incident angle modifier effects, the inlet fluid temperature T_{in} must be kept steady and as close as possible to T_{amb} to minimize heat losses and the incidence angle must be at θ_i ± 0.1°. The

requirements for peak optical efficiency are presented in Table 30. Published report from SFERA II Project suggest that the measurement should carried out at least 3 times. Additional measurements may be necessary depending on the uncertainty level calculated. If during these tests the inlet fluid temperature is higher than T_{amb} + 20 K, the heat losses produced in the collector must be measured in different runs within the low temperature range, where it is foreseen to perform the peak optical efficiency tests. A measurement point will be the mean of measures read in an interval of at least 5 minutes fulfilling the quasi-steady conditions [158].

Table 30. Peak optical efficiency test: requirements for quasi-steady conditions [158].

Parameters to be controlled	**Permitted deviation from the mean**
Inlet fluid temperature (T_{in})	± 0.5 K
Increase of the fluid temperature ($\Delta T = T_{out} - T_{in}$)	± 0.5 K or 4.0%
Mass flow rate ($\dot{m}$)	± 1.0%
Direct solar radiation (*DNI*)	± 40 W/m^2

Threshold levels (additional conditions)	**Limit**
Direct solar radiation (*DNI*)	> 800 W/m^2
Longitudinal incidence angle ($\Delta\theta_L$)	< 5°
Transversal incidence angle ($\Delta\theta_r$)	± 0.1°
Wind speed	< 5 m/s
Collector cleanliness factor	> 0.95

The value of the collector peak optical efficiency is obtained from the average of three experimental measurements of peak optical efficiency, which are calculated according to equation (52). The peak optical efficiency can be evaluated experimentally as the ratio of the radiant solar power absorbed by the receiver to the direct normal irradiance on the aperture area when there are no heat losses.

$$\eta_{opt,0^\circ} = \frac{Q_{abs}}{A_{net} \cdot DNI} = \frac{\dot{m} \cdot \Delta h}{A_{net} \cdot DNI} = \frac{\dot{m} \cdot \int_{T_{in}}^{T_{out}} c_p \cdot dT}{A_{net} \cdot DNI} \quad \textbf{(52)}$$

The peak optical efficiency test has been conducted based on introduced requirements at quasi-steady condition. The time period of the test is about 5 minutes and the incidence angle (θ_i) is equal to zero. The reported values is the mean of measures read in an interval of at least 5 minutes. Thanks to the 3-way modulating valve the inlet temperature of collector is close to ambient temperature with mean value of 23.6 °C and the maximum deviation from the mean for inlet fluid temperature is less than ±0.2 K. Figure 68 shows the variation of inlet and ambient temperature as a function of time during the peak efficiency test. During the test, the inlet fluid temperature should not exceed the permitted temperature range ($T_{in} \leq T_{amb}$ + 20 K). The average value of increase in fluid temperature is about 9.5°C with maximum variation of less than ±0.4 °C (less than 3.5%).

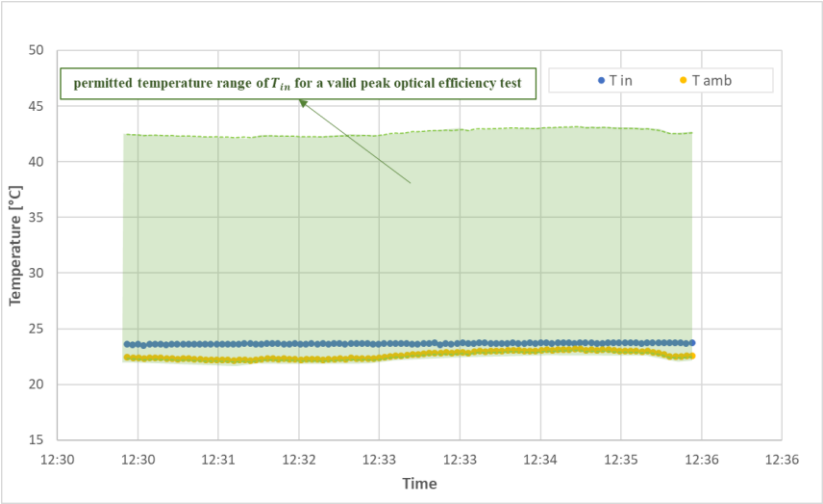

Figure 68. Inlet and ambient temperature as a function of time during the peak efficiency test.

Figure 69 shows test parameters including thermal power, DNI and efficiency as a function of time during the peak optical efficiency test. The average value of DNI is about 755 W/m^2 with the deviation from the mean of less than ±30 W/m^2. Due to the climatic situation of the test period, high level of direct solar radiation (DNI > 800 W/m^2) is not available. However, the recorded average value is not far from the imposed suggested additional conditions. Furthermore, the deviation from the mean for mass flow rate is less than 1%. The average peak optical efficiency of the collector is 61.8% with total absolute error of 1.4%.

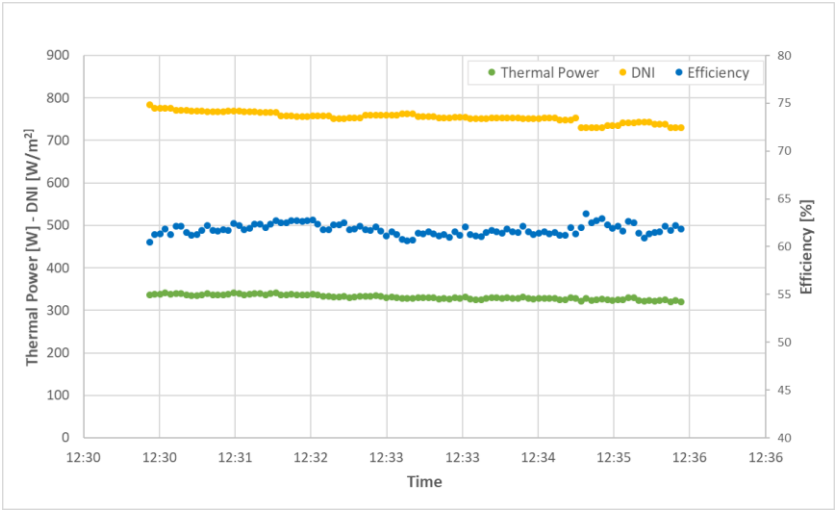

Figure 69. Test parameters as a function of time during the peak optical efficiency test.

As discussed in section 1.2.3.1, an additional cross check with single parameters available for each solar component of the whole collector can be performed. The peak optical efficiency can be calculated using the equation (15) from the intercept factor (the fraction of solar rays that actually reaches the receiver) and the optical properties (reflectance of the reflector, and transmittance of glass envelope and absorptance of the absorber tube. The intercept factor (γ) of the collector, which also accounts for the effective length of the receiver tube is equal to 1. The solar weighted reflectance of the mirrors (ρ_{total}) is 88%. The transmittance of the glass envelope (τ) and the absorptance of the absorber tube (α) are 95 and 94 percent, respectively. As a result, the peak optical efficiency calculated by equation (15) is 78.6%.

The deviation between the calculated (equation (15)) and measured (equation (52)) optical efficiency should be less than ± 5% [158].This value is an estimate and will depend on how much accurate are the values of components properties used. The report suggests that, if a high deviation is found, both each single component parameter and the results of the experimental test should be revised to look for the reason.

The deviation between calculated and measured optical efficiency is about 16%. The peak optical efficiency test valuie is 61.8% and the reduction of optical efficiency caused by experimental errors is not the main reason. In addition, good accuracy of tracking system (underlined from previous test) is also an additive powerful support for excluding the experimental errors. While the effect of transmittance of the glass envelope and absorptance of the absorber tube on the peak optical efficiency could not be verified in respect to the datasheet from the manufacturer. The optical efficiency drops could be also caused by reduction of the intercept factor due to the assembly operations of the parabolic mirror on the structure and possible micro and macro deformations of the mirrors from the ideal parabolic shape. Another reason could be caused by the reduction of the optical properties in material of receiver tube and collector due to the quality loss during the operation (corrosion, oxidation, etc.).

4.2.3 - Efficiency Test and Efficiency Curve

As mentioned earlier, the general point of the efficiency test is extracting the efficiency curve of the collector for normal incidence based on the coefficients η_0, a_1 and a_2.

According to the data presented in Table 32, 24 tests have been done under various inlet temperature and irradiance under clear sky condition for at least 5 minutes of test length. The exemplary performance measurement data for present research stems from 153 experimental points (each point represents a test of a minute length). Efficiency measurement of SC have been conducted from inlet temperature of 28 °C up to 123°C for various *DNI* values. A Maximum of 63.14% for thermal efficiency is found when the inlet temperature is 28.41°C and a minimum of 54.62% corresponds at 122.90°C. The total standard absolute uncertainty of thermal efficiency ($u_{Total}(\eta_{th})$) for test at inlet temperature of 28.41°C and 122.90°C are 0.69% and 0.77%, respectively.

Considering calculation of the uncertainty discussed in section 2.1.2 -by equations (26) and (27), uncertainty for efficiency test parameters is evaluated taking into account Type A errors for experimental data measurement and Type B errors for instrument characteristics and equipment uncertainty and total standard uncertainty is used for error propagation in the derived parameters, based on the sum-of-the-squares method on equation (53). Equation shows the propagation of the errors for the thermal efficiency by derived parameters.

$$u_{Total}(\eta_{th}) = \sqrt{\left(\frac{\partial \eta}{\partial \dot{m}} \cdot u_{Total}(\dot{m})\right)^2 + \left(\frac{\partial \eta}{\partial T_{in}} \cdot u_{Total}(T_{in})\right)^2 + \left(\frac{\partial \eta}{\partial T_{out}} \cdot u_{Total}(T_{out})\right)^2 + \left(\frac{\partial \eta}{\partial \mathrm{DNI}} \cdot u_{Total}(\mathrm{DNI})\right)^2 + \left(\frac{\partial \eta}{\partial C_p} \cdot u_{Total}(C_p)\right)^2} \quad (53)$$

Where it has been assumed that the $\dot{m}$, T_{in}, T_{out} and *DNI* values are measured during the thermal efficiency test with measurement devices described in Table 28 and the related values are presented in Table 31 and Table 32. In addition, based on ISO 9806:2017 standard specific heat

capacity of water at 1 to 12 bar is polynomial functions of the average temperature of the heat transfer fluid. Therefore, the uncertainty of the C_p *is* smaller than 0.04 %. In addition, T^* is defined by equation (54) and equation (55) shows the propagation of the errors for the T^* by derived parameters.

$$T^* = \frac{T_m - T_{amb}}{DNI} \quad \textbf{(54)}$$

$$u_{Total}(T^*) = \sqrt{\left(\frac{\partial T^*}{\partial T_{in}} \cdot u_{Total}(T_{in})\right)^2 + \left(\frac{\partial T^*}{\partial T_{out}} \cdot u_{Total}(T_{out})\right)^2 + \left(\frac{\partial T^*}{\partial T_{amb}} \cdot u_{Total}(T_{amb})\right)^2 + \left(\frac{\partial T^*}{\partial DNI} \cdot u_{Total}(DNI)\right)^2} \quad \textbf{(55)}$$

The reported expanded uncertainty is based on a standard uncertainty multiplied by a coverage factor k = 2, providing a level of confidence of approximately 95%. The expanded uncertainty, usually shown by the symbol *U* (Equation (56)).

$$U = ku_{Total} \quad \textbf{(56)}$$

Table 31. Measured values (T_{in}, T_{out} and T_{amb}) in efficiency test and their related uncertainty.

Test	Test length [min]	T_{in} [°C]	$u_{Total(Tin)}$ [°C]	T_{out} [°C]	$u_{Total(Tout)}$ [°C]	T_{amb} [°C]	$u_{Total(Tamb)}$ [°C]
1	5	28.41	0.02	38.18	0.03	20.51	0.07
2	5	31.67	0.02	42.10	0.03	22.41	0.05
3	5	35.23	0.02	45.75	0.03	22.87	0.05
4	6	38.59	0.02	49.27	0.02	22.13	0.05
5	6	38.93	0.02	49.64	0.02	22.29	0.08
6	6	39.81	0.02	50.47	0.02	22.59	0.06
7	5	41.14	0.02	51.43	0.02	23.06	0.06
8	9	50.63	0.02	60.21	0.02	29.03	0.04
9	5	53.29	0.02	63.38	0.02	31.14	0.05
10	5	53.38	0.02	63.77	0.02	31.44	0.05
11	5	53.38	0.02	63.77	0.02	31.44	0.05
12	7	65.88	0.02	75.09	0.02	27.77	0.05
13	6	83.56	0.02	93.96	0.02	28.12	0.04
14	5	83.92	0.02	94.24	0.02	27.24	0.05
15	6	84.09	0.02	94.19	0.02	27.88	0.05
16	5	88.51	0.02	98.32	0.02	30.37	0.05
17	19	89.99	0.02	100.06	0.02	29.63	0.04
18	8	91.74	0.02	102.53	0.02	18.43	0.03
19	5	92.68	0.02	103.36	0.03	18.50	0.04
20	5	93.48	0.02	104.26	0.03	18.35	0.04
21	5	95.41	0.02	104.13	0.02	30.04	0.05
22	5	98.83	0.02	108.84	0.02	32.99	0.03
23	6	122.90	0.03	132.05	0.03	29.03	0.05
24	9	123.61	0.03	132.62	0.03	28.74	0.05

Table 32. Measured values (ṁ and DNI) and obtained efficiency in efficiency test and their related uncertainty.

Test	Test length [min]	ṁ [kg/s]	$u_{Total(\dot{m})}$ [kg/s]	DNI [W/m^2]	$u_{Total(DNI)}$ [W/m^2]	η_{th} [%]	$U_{(\eta th)}$ [%]
1	5	0.008642	0.000008	787	5	63.1	1.4
2	5	0.008488	0.000008	819	5	63.6	1.3
3	5	0.008452	0.000008	841	5	62.2	1.3
4	6	0.008358	0.000008	846	5	62.2	1.3
5	6	0.008356	0.000008	846	5	62.3	1.3
6	6	0.008347	0.000008	847	5	61.8	1.3
7	5	0.008354	0.000008	842	5	60.2	1.3
8	9	0.008396	0.000007	792	5	60.7	1.4
9	5	0.008471	0.000007	832	5	60.9	1.3
10	5	0.008438	0.000007	844	5	61.6	1.3
11	5	0.008418	0.000007	844	5	61.6	1.3
12	7	0.008388	0.000007	792	5	58.9	1.3
13	6	0.008648	0.000008	877	5	60.8	1.3
14	5	0.008673	0.000008	868	5	61.1	1.3
15	6	0.008684	0.000008	869	5	59.8	1.3
16	5	0.008322	0.000007	832	5	60.4	1.3
17	19	0.008848	0.000008	892	5	59.2	1.3
18	8	0.008251	0.000008	886	5	59.6	1.3
19	5	0.008254	0.000009	890	5	58.7	1.4
20	5	0.008239	0.000009	888	5	59.3	1.4
21	5	0.008256	0.000008	762	4	58.5	1.3
22	5	0.008464	0.000008	850	5	62.0	1.3
23	6	0.00829	0.00002	832	5	54.6	1.5
24	9	0.008641	0.000013	843	5	55.4	1.5

Table 33 shows the obtained values for uncertainties calculation: x_i stands for each test parameter (T_{in}, T_{out}, $\dot{m}$, *DNI* and *Cp*), *U(xi)* defined by equation (57) and $U(C_p)$ value is $5.78 \cdot 10^{-8}$.

$$U(x_i) = \left(\frac{\partial \eta}{\partial x_i} \cdot u_{Total}(x_i) \right)^2 \quad \textbf{(57)}$$

The SC was operated under SST method and testing condition were very similar in terms of mass flow rate. As calculated uncertainty values were very small compared to their measured quantities due to the proper sensor selection and system design, the combined standard absolute uncertainty for thermal efficiency obtained by propagation of the errors based on equation (53) is also low and bring a maximum combined standard absolute error of about 0.77%. In addition, the maximum expanded uncertainty is 1.54%.

In addition, by considering the values in Table 33 the predominant influence on the overall uncertainty is caused by the measurement equipment (contributions originating from Type B uncertainty dominate those from Type A uncertainty). As a result, the accuracy of the measurements is high but their precision is in the given range.

Table 33. Calculation of the uncertainties parameters.

Test ID	T_{in} [°C]			T_{out} [°C]			$\dot{m}$ [kg/s]			DNI [W/m^2]		
	$u_A(x_i)$	$u_B(x_i)$	$U(x_i)$	$u_A(x_i)$	$u_B(x_i)$	$U(x_i)$	$u_A(x_i)$	$u_B(x_i)$	$U(x_i)$	$u_A(x_i)$	$u_B(x_i)$	$U(x_i)$
1	0.009	0.017	$1.7\cdot10^{-6}$	0.02	0.017	$3\cdot10^{-6}$	0.000003	0.000007	$3\cdot10^{-7}$	0.5	5	$1.4\cdot10^{-5}$
2	0.008	0.017	$1.4\cdot10^{-6}$	0.018	0.017	$2\cdot10^{-6}$	0.000002	0.000007	$3\cdot10^{-7}$	0.5	5	$1.4\cdot10^{-5}$
3	0.007	0.017	$1.2\cdot10^{-6}$	0.02	0.017	$2\cdot10^{-6}$	0.000002	0.000007	$3\cdot10^{-7}$	0.5	5	$1.3\cdot10^{-5}$
4	0.005	0.017	$1.1\cdot10^{-6}$	0.017	0.017	$2\cdot10^{-6}$	0.000003	0.000007	$3\cdot10^{-7}$	0.6	5	$1.3\cdot10^{-5}$
5	0.006	0.017	$1.2\cdot10^{-6}$	0.016	0.017	$2\cdot10^{-6}$	0.000003	0.000007	$3\cdot10^{-7}$	0.6	5	$1.3\cdot10^{-5}$
6	0.007	0.017	$1.2\cdot10^{-6}$	0.017	0.017	$2\cdot10^{-6}$	0.000003	0.000007	$3\cdot10^{-7}$	0.5	5	$1.3\cdot10^{-5}$
7	0.006	0.017	$1.2\cdot10^{-6}$	0.017	0.017	$2\cdot10^{-6}$	0.000002	0.000007	$3\cdot10^{-7}$	0.6	5	$1.2\cdot10^{-5}$
8	0.006	0.017	$1.4\cdot10^{-6}$	0.012	0.017	$1.9\cdot10^{-6}$	0.000002	0.000007	$3\cdot10^{-7}$	1.6	5	$1.4\cdot10^{-5}$
9	0.004	0.017	$1.2\cdot10^{-6}$	0.008	0.017	$1.3\cdot10^{-6}$	0.000002	0.000007	$3\cdot10^{-7}$	0.7	5	$1.3\cdot10^{-5}$
10	0.004	0.017	$1.1\cdot10^{-6}$	0.006	0.017	$1.2\cdot10^{-6}$	0.000002	0.000007	$3\cdot10^{-7}$	0.5	5	$1.3\cdot10^{-5}$
11	0.004	0.017	$1.1\cdot10^{-6}$	0.006	0.017	$1.2\cdot10^{-6}$	0.000002	0.000007	$3\cdot10^{-7}$	0.5	5	$1.3\cdot10^{-5}$
12	0.006	0.017	$1.4\cdot10^{-6}$	0.011	0.017	$1.7\cdot10^{-6}$	0.000002	0.000007	$3\cdot10^{-7}$	0.5	5	$1.1\cdot10^{-5}$
13	0.011	0.017	$1.6\cdot10^{-6}$	0.011	0.017	$1.5\cdot10^{-6}$	0.000002	0.000007	$3\cdot10^{-7}$	0.7	5	$1.3\cdot10^{-5}$
14	0.011	0.017	$1.4\cdot10^{-6}$	0.010	0.017	$1.4\cdot10^{-6}$	0.000002	0.000007	$3\cdot10^{-7}$	0.8	5	$1.3\cdot10^{-5}$
15	0.008	0.017	$1.3\cdot10^{-6}$	0.013	0.017	$1.7\cdot10^{-6}$	0.000002	0.000007	$3\cdot10^{-7}$	0.5	5	$1.2\cdot10^{-5}$
16	0.011	0.017	$1.5\cdot10^{-6}$	0.015	0.017	$2\cdot10^{-6}$	0.000002	0.000007	$3\cdot10^{-7}$	0.6	5	$1.2\cdot10^{-5}$
17	0.011	0.017	$1.5\cdot10^{-6}$	0.009	0.017	$1.4\cdot10^{-6}$	0.000002	0.000008	$3\cdot10^{-7}$	0.6	5	$1.2\cdot10^{-5}$
18	0.011	0.017	$1.4\cdot10^{-6}$	0.015	0.017	$1.7\cdot10^{-6}$	0.000005	0.000007	$4\cdot10^{-7}$	0.6	5	$1.2\cdot10^{-5}$
19	0.016	0.017	$1.8\cdot10^{-6}$	0.019	0.017	$2\cdot10^{-6}$	0.000005	0.000007	$4\cdot10^{-7}$	0.5	5	$1.2\cdot10^{-5}$
20	0.015	0.017	$1.7\cdot10^{-6}$	0.03	0.017	$3\cdot10^{-6}$	0.000006	0.000007	$5\cdot10^{-7}$	0.5	5	$1.2\cdot10^{-5}$
21	0.012	0.017	$1.9\cdot10^{-6}$	0.013	0.017	$2\cdot10^{-6}$	0.000003	0.000007	$3\cdot10^{-7}$	0.8	4	$1.1\cdot10^{-5}$
22	0.009	0.017	$1.5\cdot10^{-6}$	0.014	0.017	$1.9\cdot10^{-6}$	0.000002	0.000007	$3\cdot10^{-7}$	0.6	5	$1.2\cdot10^{-5}$
23	0.019	0.017	$2\cdot10^{-6}$	0.02	0.017	$3\cdot10^{-6}$	0.00002	0.000007	$1.9\cdot10^{-6}$	0.6	5	$1.1\cdot10^{-5}$
24	0.02	0.017	$3\cdot10^{-6}$	0.03	0.017	$4\cdot10^{-6}$	0.000011	0.000007	$7\cdot10^{-7}$	0.6	5	$1.1\cdot10^{-5}$

The contributions to the uncertainty on thermal efficiency are reported in Figure 70. From the pie chart, it is clear that the majority of contribution to the uncertainty is due to the measurement of *DNI* (about three-quarters). Thanks to calibration of RTD Pt100, sensor uncertainties of inlet and outlet temperature evaluations for the given set-up is low even in high temperature and contribution to the uncertainty for ΔT is 21.5%. Thanks to the selected Coriolis flowmeter the related contribution to the uncertainty is 2.43%. Whereas contribution of the C_p to the uncertainty is undoubtedly the smallest and negligible by 0.36%.

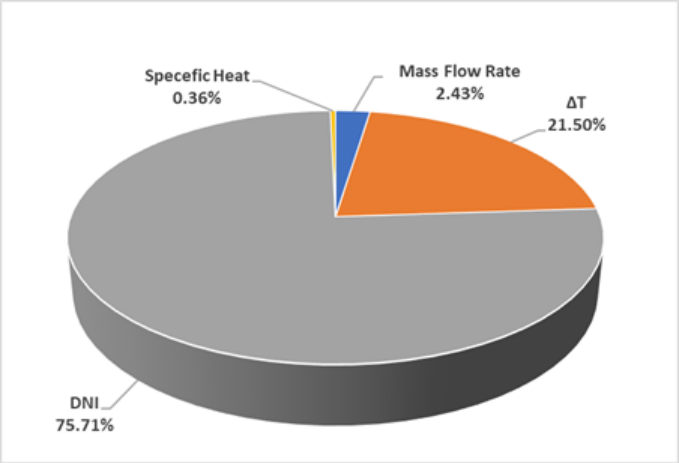

Figure 70. Uncertainty contributions of measured quantities to thermal efficiency.

The collector parameters (coefficient of η_0, a_1, a_2 in equation (50)) result from fitting a model equation to the experimental data. Multiple linear regression (MLR) based on least square (LS) and weighted least squares (WLS) are commonly used for fitting the measurement data and determine the values of coefficients. LS method uses constant value of uncertainty (deviation) for all observations. However, in WLS method measurement points with higher uncertainty have less

impact on the obtaining fit than those with lower uncertainty. As in reality, the uncertainty is almost never constant for all observations and each data point has its own uncertainty the WLS method has been used for fitting the measurement data [118,119,159]. More detailed information are presented in Appendix C.

Equation (58) shows weighted parameters evaluation function (χ^2) for N test points to be fitted with M parameters function.

$$\chi^2 = \sum_{i=1}^{N} \left(\frac{(\eta_i - \eta(x_i; a_1, \dots, a_M)^2}{u^2{}_i} \right) \quad \textbf{(58)}$$

Where $u^2{}_i$ is the variance of the difference and this weighting uncertainty is calculated as Equation (59) for uncertainty in *x* (independent) and in *y* (dependent variable).

$$u^2{}_i = u^2{}_y + \sum \left(\frac{\partial y}{\partial x_i} \right)^2 \cdot u^2{}_{x_i} \quad \textbf{(59)}$$

Based on equation (50), the description of the matrix calculation can be described by equation (60). Where T^* is defined by equation (54).

$$\begin{bmatrix} K(\theta)_{Test\ 1} & T^*_{Test\ 1} & (T_m - T_{amb}) \cdot T^*_{Test\ 1} \\ K(\theta)_{Test\ 2} & T^*_{Test\ 2} & (T_m - T_{amb}) \cdot T^*_{Test\ 2} \\ \vdots & \vdots & \vdots \\ K(\theta)_{Test\ N} & T^*_{Test\ N} & (T_m - T_{amb}) \cdot T^*_{Test\ N} \end{bmatrix} \begin{bmatrix} \eta_0 \\ a_1 \\ a_2 \end{bmatrix} = \begin{bmatrix} \eta_{Test\ 1} \\ \eta_{Test\ 2} \\ \vdots \\ \eta_{Test\ N} \end{bmatrix} \quad \textbf{(60)}$$

Table 34 shows the regression parameters and their associated errors based on LS and WLS method.

Table 34. Regression parameters based on LS and WLS (Fit I & Fit II) method and associated errors.

Method	**LS**	**WLS (Fit I)**		**WLS (Fit II)**	
Parameters	Estimate	Estimate	Uncertainty	Estimate	Uncertainty
η_0	0.6204	0.6207	0.00375	0.6207	0.00375
a_1 [W/(m^{2}K)]	0.0630	0.0632	0.13753	-	-
a_2 [W/(m^{2}K^2)]	-0.0059	-0.0059	0.00124	-0.0059	0.00124

Table 34 shows that the resulting WLS Fit I is not suitable to model thermal losses increasing with temperature because the positive value of a1 has not a physical sense. WLS Fit I has indeed a maximum at operative temperature higher than the ambient caused by its non-restricted fitting parameters, uneven spacing of measurement points and absence of many collector performance testing points at very low temperature difference (Which require cooling of the heat transfer fluid below the ambient temperature). Mentioned fitting problems can be solved by restricting the linear term (setting a_1=0), which leads to WLS Fit II. Equation (61) shows the efficiency curve of the collector by WLS Fit II.

$$\eta_{th} = 0.6207 - 0.0059\frac{(T_m - T_a)^2}{DNI} \quad \textbf{(61)}$$

Figure 71 shows the efficiency curve of the small size collector with the respective uncertainty limits.

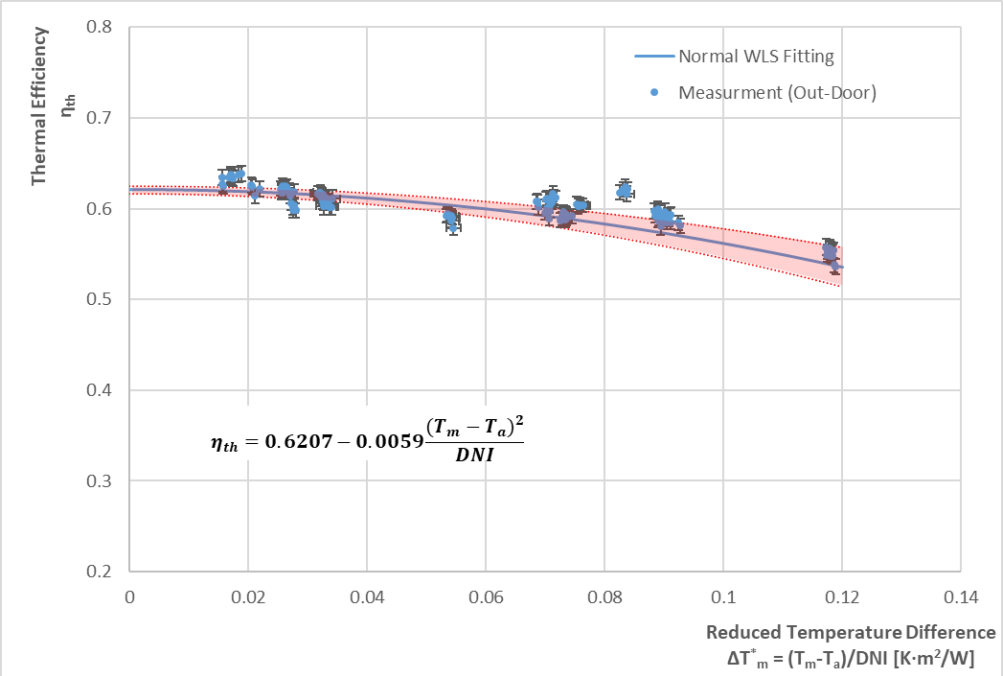

Figure 71. Fitting result of the efficiency test data at DNI= 1000W/m^2 with the respective uncertainty limits.

The heat losses measured in-door can be slightly different from the heat loss measured out-door due to the various factors including higher convective loss in outdoor test in comparison the indoor test [126]. In addition, overall collector heat loss could be affected by the long-wave radiation in the test room. It is not likely, however, that the interior will be far from radiative equilibrium since the shortwave radiation contains higher amounts of energy and longwave radiation contains a smaller amount of energy. Furthermore, the value of efficiency is varing with mass fluid temperature in outdoor condition and if a mean value is assigned to overall collector heat loss coefficient it will embody a mean efficiency value which will not be the same as the mean value for service conditions [160].

The efficiency curve for in-door test derived from measured heat losses. $\dot{Q}_{solar}$ is concentrated solar energy (the direct normal irradiance on the aperture area). The efficiency values from indoor test results are derived from heat losses, adding to the optical efficiency value (61.8%) and can be described by equation (62).

$$\eta_{th-indoor} = \eta_{opt,0^\circ} - \frac{\dot{Q}_{loss-indoor}}{\dot{Q}_{solar}} = \eta_{opt,0^\circ} - \frac{\dot{Q}_{loss-indoor}}{A_{net} \cdot DNI} \quad \textbf{(62)}$$

Where $\eta_{opt,0^\circ}$ is defined by equation (52) and A_{net} is about 0.705 m^2 for one collector. The *DNI* value for each ΔT ($\Delta T = T_m - T_{amb}$) is defined by closest value of *DNI* at the same ΔT in outdoor

test. When ΔT is 5 °C the efficiency is about 61.8% and lowest efficiency value is 60.4% at ΔT of 100 °C with absolute uncertainty of 1.4% for both of them. The reported expanded uncertainty is based on a standard uncertainty multiplied by a coverage factor k=2, providing a level of confidence of approximately 95%. The efficiency drops about 1.5% from almost ambient to 100 °C above the ambient temperature.

Figure 72 shows the efficiency curve obtained from in-door thermal loss test. When the collector is tested indoors, the thermal losses are determined for a range of temperature under a condition in which no solar radiation is incident on the receiver. The average thermal efficiency obtained from indoor tests is 60.5% with total absolute error of 1.5%.

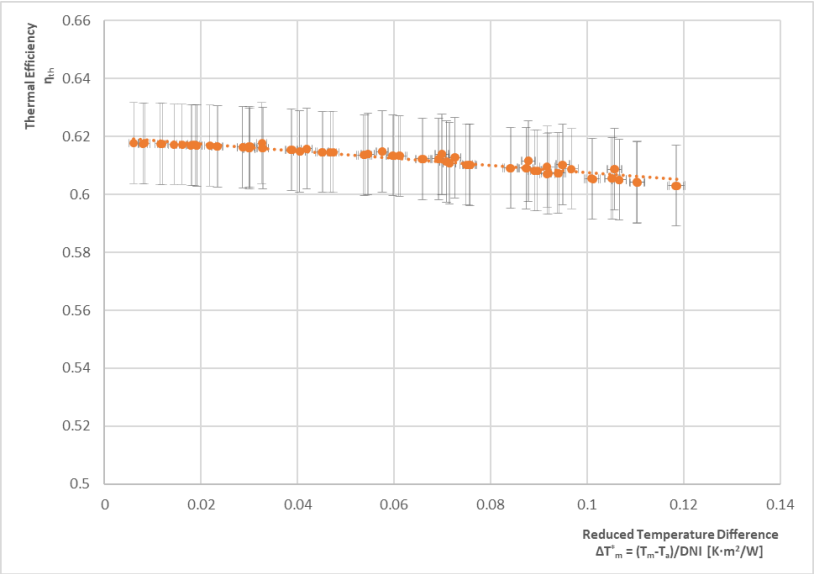

Figure 72. The efficiency curves obtained from indoor heat loss tests.

The contributions to the uncertainty presented in figure 67 and the majority of it is due to the measurement of peak optical efficiency (93% of 1.5% total absolute error) and the rest is related to the in-door thermal loss measurment. From this 93% in peak optical efficiency measurement the uncertainty mainly is related to the measurement of DNI (about three-quarters) and contribution to the uncertainty for ΔT and mass flow rate are 21.5%. and 2.43% , respectively.

Figure 73 shows comparison of efficiency curves obtained from outdoor and indoor tests results. In general the results of thermal efficiency test obtained from indoor test have lower values. For example at 27°C of temperature difference above ambient temperature the efficiency difference is less than 1%. Since, the estimation of thermal efficiency obtained from indoor test is not based on most accurate method at higher temperature the results obtained from outdoor test are not in agreement with it. For example, at 100°C of temperature difference above ambient temperature the efficiency difference is about 5%.

However the value determined for $\eta_{opt,0^\circ}$ is depend upon the diffuse fraction and the long-wave radiation intensity. It means that, overall collector heat loss coefficient could be affected by the long-wave radiation in the test room. Therefore, variation from the predicted value of $\eta_{opt,0^\circ}$ are to be expected as a result of variation in the diffuse fraction, the long-wave radiation and temperature dependence of the heat loss coefficient. Together, these factors may change the effective value of $\eta_{opt,0^\circ}$ by 5% or more. In detail, longwave atmospheric radiation can influence the collection efficiency by up to 3 per cent, and solar absorption in collector cover glasses also has an influence of 2–3 per cent. The effects are greater for collectors with strong dependency on fluid temperature

[160]. In addition, due to the more noticeable difference at higher temperature, the heat losses along the pipes could be another reason for efficiency difference between indoor and outdoor test. Moreover, unknown systematic errors can also cause this difference.

A)

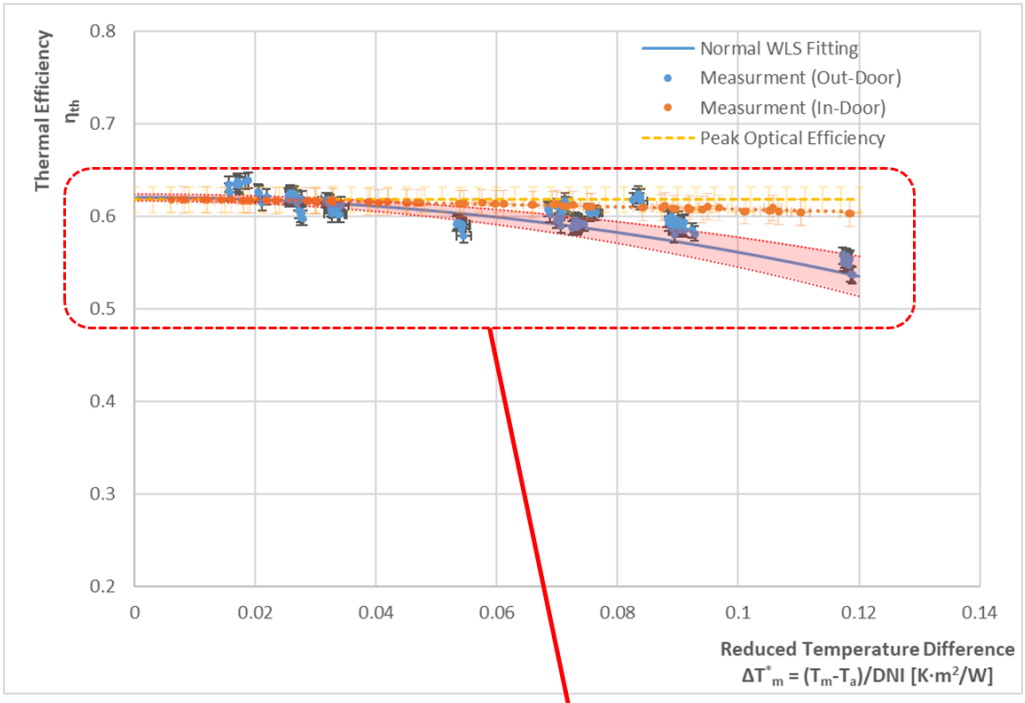

B)

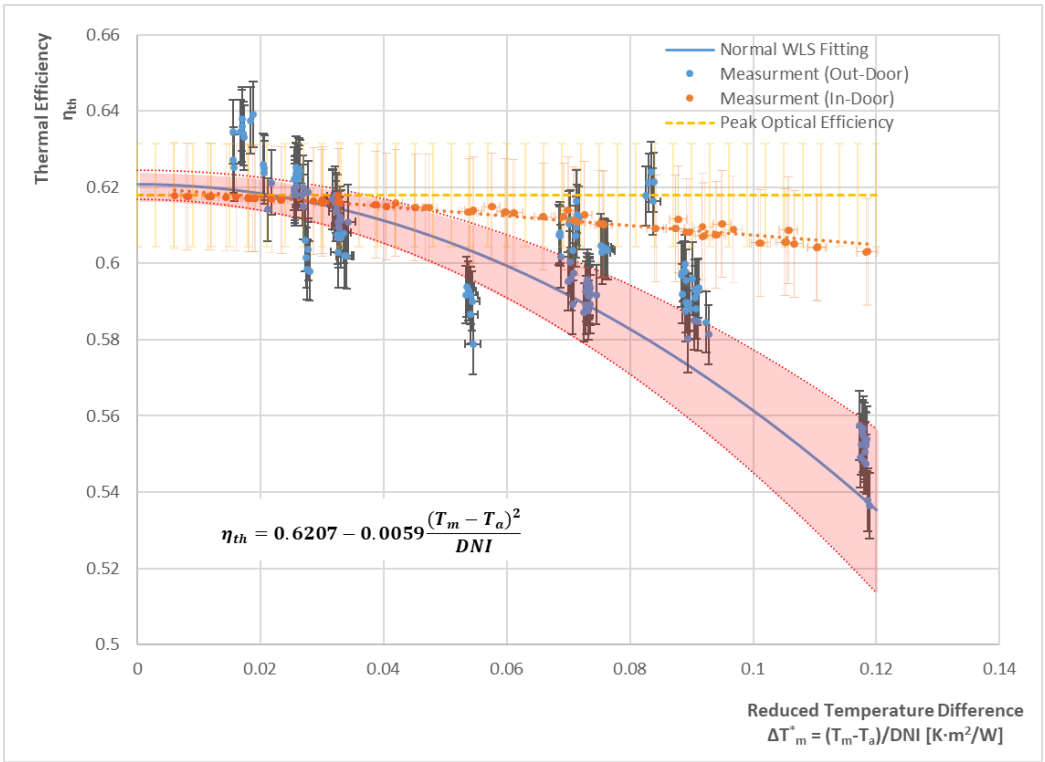

Figure 73. Comparison of efficiency curves obtained from outdoor and indoor tests results.

5 - Conclusion

The main objective of the work presented in this thesis was to analyze experimentally and computationally the small-size solar receiver (UF-RT01) for industrial and residential application. UF-RT01 receiver of small size parabolic trough collector called m-PTC were investigated experimentally by indoor and outdoor tests and computationally by 3D heat transfer FEM model. The UF-RT01 receiver has a specific design, being formed by two coaxial tubes so that the fluid inlet and output are at the same side. It was properly developed to scale the PTC technology toward smaller size. The purpose is the installation in urban context and the application in industrial process.

As mentioned before, almost all study cases are referred to common standard receivers for parabolic trough collectors. For common standard size receivers (absorber tube outer diameter of 70 mm) indoor and outdoor test stands have been developed at several institutions with the aim of studying receiver thermal losses. Therefore, measurement methods and facilities need to be improved for smaller size receivers.

An indoor test rig for small-size solar receivers (UF-RT01) have been realized and a specific prototype has been tested in order to evaluate the thermal loss. The dimensions of the absorber force to adapt the procedures on literature with a specific attention for sensors choice and positioning as well as the for power supply devices. Since the heat loss are expected to be low (under 50 W), in preliminary test stand by removing the inner coaxial steel tube, two nickel-chrome wire heaters are inserted along the length of absorber tube. An additional external heater is also placed before the Kovar part to meet the adiabatic condition and minimizing the temperature gradient. The preliminary results on the tested prototype shows the behavior of its performance at increasing temperature up to 180°C. In that regime a maximum heat loss of 23.98 W is found while at lower fixed temperatures (40, 59, 88, 106, 119, 143, 164 and 176°C) it drops down to 0.9, 2.31, 5.91, 6.41, 9.63, 14.03, 19.03 and 22.35 W, respectively. However, due to the small non-uniform temperature distribution along the tube, the preliminary indoor test stand at first phase has been slightly modified. The second and improved test set up has been developed for thermal loss measurement and instead of nickel-chrome wire heater, an industrial cartridge heater made of resistance wire (NiCr20/80) as a core covered with stainless steel 304 as a sleeve (sheath) has been used. Three different tube from same type (UF-RT01) have been tested in the range of interest and the procedure was repeated for about 150 cases. In comparison to preliminary test stand, results showed more uniformity in temperature distribution along the tube. A maximum value of 17.89 W is found when ΔT is 163°C (receiver average temperature of 190°C). In order to achieve production assurance and have more clear vision about the results due to the different results obtained from test on RT03 in comparison to the RT01 and RT02 with higher thermal loss, new tests have been conducted on additional tubes. Similar setup and test procedure have been conducted in order to evaluate the uniformity of temperature along the tube and estimate the heating supplier parameters in additional tubes. Seven different tube from same type have been tested and labeled as RT04-RT10. Results from tests on RT01 and RT02 are in accordance with new results obtained from heat loss test on RT04-RT10. Therefore, the different results related to the RT03 are to be expected as a result of variation in production quality by manufacturer of receiver tube.

In respect to standard PTCs technology, the proposed small size receiver is meant to be applied in collectors suitable for roofs or compact installation areas. The chord length is therefore limited under 500 mm and the absorber diameter could not be directly scaled down from the standard one to avoid too small flow section surface and high-pressure loss. The diameter is then set at 10 mm.

This led to obtain a concentration ratio of about 13 (aperture length/absorber circumference), lower than in the standard PTC. Consequently, thermal loss is expected to be higher per unit aperture area. At the same time, the one side inlet/outlet configuration is considered advantageous because it helps in piping layout and in ensuring the internal vacuum condition over time (the glass envelope is indeed sealed itself one side). Mentioned laboratory thermal loss test stand will be a useful tool for evaluating the current and future small-size receivers for parabolic trough collectors. By now, the work will be also focused on outdoor testing of heat loss for comparison and confirmation of results.

In order to predict the thermal performance and analyze the relevant physical characteristics of the receiver tube such as the value of emissivity at higher temperature, a heat transfer model using FEM simulation method has been realized with Comsol Multiphysics software. An adaptive mesh refinement (AMR) with different mesh configurations for the model has been conducted in order to increase storage and computational savings. By using a parametric sweep to vary the maximum element size, the model solved using meshes with different mesh density in order to study how it affects the solution. The model simulated with refined mesh having 77452 degrees of freedom (base mesh of C) showed more accurate temperature distribution along the absorber tube. The relative deviation in average temperature of the absorber tube from experimental result at low temperature (T_{ave} = 30°C) for base mesh of C is 3.8%. The heat transfer model is able to precisely predict the heat losses at low temperature of the absorber tube with constant value of emissivity reported by manufacturer. The results indicate that the difference of average temperature of absorber tube obtained by simulation and experiment is less than 1°C and obtained values for each thermocouple (TC1-TC5) from simulation are inside the uncertainty range of each sensor. The estimation of emissivity at the higher temperature obtained by solving the model with various emissivity values for each test at specific input power until the average temperature inside the absorber tube obtained by simulation were in agreement with experimental value.

In order to perform the out-door test according to ISO 9806:2017 the designed and assembled test rig platform at first phase has been slightly modified. The first phase test rig platform has an electric resistance heater (9 electric resistance of 1 kW) installed inside the tank with an on/off control system. However, due to the distance between the heat exchanger and the inlet of the collector the inlet temperature of collectors were not stable. Therefore, an implementation of silicon heater mats with a total power of 500W have been realized on the header pipe just before the inlet of collector to reduce the heat losses and reach stable inlet temperature. The reliability and behavior of the test rig has been evaluated thanks to 24 test points. ISO 9806:2017 standard devoted to assess the performance of the small-size PTC and the measurement devices properly selected in order to minimize the uncertainty.

The reliability of implemented test bench and output power and efficiency of a novel small size parabolic trough collector have been evaluated by preliminary test. For this purpose an out-door tests at ambient temperature on the designed small size PTC test rig is carried out during clear sky day. During the test interval, the average value of DNI, mass flow rate and ambient temperature are 714 W/m^2, 29.6 Kg/h and 29.1°C, respectively. The deviation of ambient temperature, inlet temperature and mass flow rate should be less than ± 1.0°C, ± 0.1°C and ± 1.0%, respectively. The peak optical efficiency test has been conducted at quasi-steady condition and the average peak optical efficiency of the collector is 61.8% with total absolute error of 1.4%. Efficiency measurement of solar collector have been conducted from inlet temperature of 28 °C up to 123°C for various DNI values. A Maximum of 63.1% for thermal efficiency is found when the inlet temperature is 28.4°C and a minimum of 54.6% corresponds at 122.9°C. The total standard absolute uncertainty of thermal efficiency for test at inlet temperature of 28.5°C and 122.9°C are 0.7% and 0.8%, respectively. About three-quarters of contribution to the uncertainty is due to the

measurement of *DNI*. In addition, the uncertainty related to the measurement equipment (Type B) causes the predominant influence on the overall uncertainty. In addition, the maximum expanded uncertainty is 1.6% by a coverage factor k = 2, providing a level of confidence of approximately 95%. The data have been fitted through a multiple linear regression based on WLS method and efficiency curve coefficients have been obtained for normal incidence. Based on WLS Fit II η_0, a_1 and a_2 are 0.6207, 0 and -0.0059, respectively.

The experimental and computational characterization carried out on the UF-RT01 receiver tube proved that the obtained results from indoor and outdoor test are in good agreement. Indoor test stand will be a useful tool for evaluating future small-size receivers for parabolic trough collectors. Developed heat transfer model using FEM simulation method is also able to predict the heat losses at low temperature of the absorber tube. Results from outdoor tests revealed that there is variation from the predicted value of efficiency adopted from indoor test results. The variation to be expected as a result of variation in the diffuse fraction, the long-wave radiation and temperature dependence of the heat loss coefficient. Together, these factors may change the effective value by 5% or more. In addition, due to the more noticeable difference at higher temperature, the heat losses along the pipes could be another reason for efficiency difference between indoor and outdoor test. Moreover, unknown systematic errors can also cause this difference.

The small size PTC technology for medium temperature application can offer many advantages over conventional plate collectors, and are associated with higher operating temperatures, smaller space requirements and greater system efficiencies.

A way to improve a PTC thermal efficiency would lies in the adoption of novel heat transfer fluid (HTF) in order to increase the operating temperature. As a results the amount of heat collected per unit area increases and therefore higher thermodynamic efficiencies and smaller heat losses could be reached. By changing the HTF the material of the tube receiver will need to be adopted with it. Therefore, the challenge is not only focused on HTF but also change in the material of the metal tube depending on properties of HTF, operating pressure and temperature of PTC, cost, etc.

Improvement and validation of new indoor test stand for novel small size receiver could be another field for future activities. This could be achieved by conducing further experimental investigations at the inlet of the receiver were the uniformity in temperature without external heater is not achievable. In addition, better understanding of heat transfer rate around the inlet of the receiver is also helpful for this purpose. Another promising study could be focused on the precise effect of variation in the diffuse fraction, the long-wave radiation and temperature dependence of the heat loss coefficient on the efficiency difference between indoor and outdoor test results. Furthermore, measuring the performances of the collector varying the incidence angle and performing the dynamic test method on the collector may be also beneficial for better understanding the system.

Reducing the cost of development and maintenance without compromising operational reliability would improve the value for money for small size PTC in medium temperature application. It would also release substantial capital for new investments contributing to the further studies in efficiency improvement. This could be achieved by replacing the bearing structure of small size PTC by composite materials, glass fibers and polyester resin in order to reduce the cost of operation, maintenance, assembly, transport and installation.

It is also challenging to increase/maintain the optical efficiency of a small size PTC while increasing the concentration ratio. Since the major part of the losses is due to optical losses, around 38%. In order to increase intercept factor and reduce optical losses, taking careful account in manufacturing and assembly of the parabolic mirror is necessary to avoid micro and macro

deformations of the mirrors from the ideal parabolic shape. Another way to reduce optical losses could be achieved by increasing the life time and stability of selective coating. Therefore, future breakthrough is needed to further improve the coating materials of the receiver. In addition, better linear actuator operation with same velocity can minimize the tracking and concentrating errors.

Another promising field of investigation could be focused on development of thermochemical energy storage (TCES). TCES is a key technology to developing highly efficient short and long-term thermal energy storage for various applications, such as solar thermal systems coupling with PTC. So far, main technology for storing heat is sensible seasonal heat storage (large hot water tanks). However, sensible seasonal heat storages have a low storage capacity (~ 60 kWh/m³ at a temperature difference of 50°C) and relatively high heat losses to the ambient during the storage period. Therefore, compact and long-term storage processes will play an important role in future energy systems. Reduced heat losses and high specific storage capacities are key technical characteristics for future energy storage developments.

References

[1] Zhou D, Zhao C-Y, Tian Y. Review on thermal energy storage with phase change materials (PCMs) in building applications. Appl Energy 2012;92:593–605.

[2] Canadell JG, Le Quéré C, Raupach MR, Field CB, Buitenhuis ET, Ciais P, et al. Contributions to accelerating atmospheric CO2 growth from economic activity, carbon intensity, and efficiency of natural sinks. Proc Natl Acad Sci 2007;104:18866–70.

[3] Evangelisti L, Vollaro RDL, Asdrubali F. Latest advances on solar thermal collectors: A comprehensive review. Renew Sustain Energy Rev 2019;114:109318.

[4] Pata UK. Renewable energy consumption, urbanization, financial development, income and CO2 emissions in Turkey: testing EKC hypothesis with structural breaks. J Clean Prod 2018;187:770–9.

[5] Murdock HE, Gibb D, André T, Appavou F, Brown A, Epp B, et al. Renewables 2019 Global Status Report 2019.

[6] First PJ. Global Warming of 1.5 C An IPCC Special Report on the Impacts of Global Warming of 1.5 C Above Pre-Industrial Levels and Related Global Greenhouse Gas Emission Pathways, in the Context of Strengthening the Global Response to the Threat of Climate Change. Sustain Dev Efforts to Eradicate Poverty Https//Www Ipcc Ch/Sr15/ Accessed 2019;1.

[7] Prentice IC, Farquhar GD, Fasham MJR, Goulden ML, Heimann M, Jaramillo VJ, et al. The carbon cycle and atmospheric carbon dioxide, Cambridge University Press; 2001.

[8] Agency IE. Key World Energy Statistics 2018. OECD Publishing; 2018.

[9] Conti J, Holtberg P, Diefenderfer J, LaRose A, Turnure JT, Westfall L. International energy outlook 2016 with projections to 2040. USDOE Energy Information Administration (EIA), Washington, DC (United States …; 2016.

[10] Blasing TJ. Recent Greenhouse Gas Concentrations. 2009. No August 2016:1–5.

[11] Kabir E, Kumar P, Kumar S, Adelodun AA, Kim K-H. Solar energy: Potential and future prospects. Renew Sustain Energy Rev 2018;82:894–900.

[12] UNDP U. WEC (2000) World Energy Assessment: Energy and the Challenge of Sustainability. United Nations Dev Program New York 2000.

[13] Fridleifsson IB. Geothermal energy for the benefit of the people. Renew Sustain Energy Rev 2001;5:299–312.

[14] Mette B, Kerskes H, Drück H. Process and reactor design for thermo-chemical energy stores. ISES Sol. World Congr., vol. 28, 2011.

[15] Bertoldi P, López-Lorente J, Labanca N. Energy Consumption and Energy Efficiency Trends in the EU-28 2000–2014. Jt Res Cent Ispra, Italy 2016.

[16] Kumar L, Hasanuzzaman M, Rahim NA. Global advancement of solar thermal energy technologies for industrial process heat and its future prospects: A review. Energy Convers Manag 2019;195:885–908.

[17] EIA J. International Energy Outlook. US Energy Information Administration. DOE/EIA-0484 (2013) Edition; 2013.

[18] Honoré A. Decarbonisation of heat in Europe: implications for natural gas demand 2018.

[19] Mathiesen BV. Heat Roadmap Europe: A low-carbon heating and cooling strategy for Europe. Resour Results 2018.

[20] Economidou M, Atanasiu B, Despret C, Maio J, Nolte I, Rapf O. Europe's buildings under the microscope. A country-by-country review of the energy performance of buildings. Build Perform Inst Eur 2011:35–6.

[21] Coccia G, Di Nicola G, Hidalgo A. Parabolic trough collector prototypes for low-temperature process heat. Springer; 2016.

[22] Cartalis C, Synodinou A, Proedrou M, Tsangrassoulis A, Santamouris M. Modifications in energy demand in urban areas as a result of climate changes: an assessment for the southeast Mediterranean region. Energy Convers Manag 2001;42:1647–56.

[23] Şen Z. Solar energy fundamentals and modeling techniques: atmosphere, environment, climate change and renewable energy. Springer; 2008.

[24] Besarati SM, Padilla RV, Goswami DY, Stefanakos E. The potential of harnessing solar radiation in Iran: Generating solar maps and viability study of PV power plants. Renew Energy 2013;53:193–9.

[25] Mohanty P, Muneer T, Gago EJ, Kotak Y. Solar radiation fundamentals and PV system components. Sol. Photovolt. Syst. Appl., Springer; 2016, p. 7–47.

[26] Herrando M, Markides CN. Hybrid PV and solar-thermal systems for domestic heat and power provision in the UK: Techno-economic considerations. Appl Energy 2016;161:512–32.

[27] Zhang HL, Baeyens J, Degrève J, Cacères G. Concentrated solar power plants: Review and design methodology. Renew Sustain Energy Rev 2013;22:466–81.

[28] Power CS. Technology roadmap concentrating solar power. Current 2010;5:1–52.

[29] Horta P, FhG ISE. Process Heat Collectors: State of the Art and available medium temperature collectors. Int Energy Agency Task 2015;49.

[30] Sharma AK, Sharma C, Mullick SC, Kandpal TC. Solar industrial process heating: A review. Renew Sustain Energy Rev 2017;78:124–37.

[31] Fernández-García A, Zarza E, Valenzuela L, Pérez M. Parabolic-trough solar collectors and their applications. Renew Sustain Energy Rev 2010;14:1695–721.

[32] Jradi M, Riffat S. Medium temperature concentrators for solar thermal applications. Int J Low-Carbon Technol 2014;9:214–24.

[33] Kalogirou S. The potential of solar industrial process heat applications. Appl Energy 2003;76:337–61.

[34] Islam MT, Huda N, Abdullah AB, Saidur R. A comprehensive review of state-of-the-art concentrating solar power (CSP) technologies: Current status and research trends. Renew Sustain Energy Rev 2018;91:987–1018.

[35] Solargis. Solar resource maps of World. World Bank Gr 2019. https://solargis.com/maps-and-gis-data/download.

[36] Heller P. Introduction to CSP systems and performance. Perform. Conc. Sol. power Syst., Elsevier; 2017, p. 1–29.

[37] Potential for Solar Thermal Energy By Country - Italy. SolarPACES 2015. https://www.solarpaces.org/csp-technologies/csp-potential-solar-thermal-energy-by-member-nation/italy/.

[38] Müller-Steinhagen H, Trieb F. Concentrating solar power. A Rev Technol Ingenia Inf QR Acad Eng 2004;18:43–50.

[39] Romero M, González-Aguilar J. Solar thermal CSP technology. Wiley Interdiscip Rev Energy Environ 2014;3:42–59.

[40] Upadhyay BH, Patel AJ, Ramana P V. A detailed review on solar parabolic trough collector. Int J Ambient Energy 2019:1–21.

[41] Gunther M, Joemann M, Csambor S. Advanced CSP Teaching Materials, Chapter 5: Parabolic Trough Technology. EnerMENA Ger Aerosp Cent [DLR] 2011.

[42] Arasu AV, Sornakumar T. Design, manufacture and testing of fiberglass reinforced parabola trough for parabolic trough solar collectors. Sol Energy 2007;81:1273–9.

[43] Schweitzer A, Schiel W, Birkle M, Nava P, Riffelmann K-J, Wohlfahrt A, et al. ULTIMATE TROUGH®-Fabrication, erection and commissioning of the world's largest parabolic trough collector. Energy Procedia 2014;49:1848–57.

[44] Montes IEP, Benitez AM, Chavez OM, Herrera AEL. Design and construction of a parabolic trough solar collector for process heat production. Energy Procedia 2014;57:2149–58.

[45] Behar O, Khellaf A, Mohammedi K. A novel parabolic trough solar collector model–Validation with experimental data and comparison to Engineering Equation Solver (EES). Energy Convers Manag 2015;106:268–81.

[46] Zou B, Dong J, Yao Y, Jiang Y. A detailed study on the optical performance of parabolic trough solar collectors with Monte Carlo Ray Tracing method based on theoretical analysis. Sol Energy 2017;147:189–201.

[47] Upadhyay BH, Patel AJ, Ramana P V. Parabolic Trough Collector, a Novel Design for Domestic Water Heating Application. Int J Res Appl Sci Eng Technol 2017;5:497–503.

[48] Agagna B, Smaili A, Falcoz Q, Behar O. Experimental and numerical study of parabolic trough solar collector of MicroSol-R tests platform. Exp Therm Fluid Sci 2018;98:251–66.

[49] Cabrera FJ, Fernández-García A, Silva RMP, Pérez-García M. Use of parabolic trough solar collectors for solar refrigeration and air-conditioning applications. Renew Sustain Energy Rev 2013;20:103–18.

[50] Price H, Lu¨ pfert E, Kearney D, Zarza E, Cohen G, Gee R, et al. Advances in parabolic trough solar power technology. J Sol Energy Eng 2002;124:109–25.

[51] Maccari A, Donnola S, Matino F, Tamano S. Archimede solar energy molten salt parabolic trough demo plant: Improvements and second year of operation. AIP Conf. Proc., vol. 1734, AIP Publishing LLC; 2016, p. 100007.

[52] Maccari A, Bissi D, Casubolo G, Guerrini F, Lucatello L, Luna G, et al. Archimede solar energy molten salt parabolic trough demo plant: a step ahead towards the new frontiers of CSP. Energy Procedia 2015;69:1643–51.

[53] Wittmann M, Müller-Elvers C, Schenk H, Bruce B. Optimization of Molten Salt Parabolic Trough Power Plants using different Salt Candidates 2012.

[54] Zaversky F, Medina R, García-Barberena J, Sánchez M, Astrain D. Object-oriented modeling for the transient performance simulation of parabolic trough collectors using molten salt as heat transfer fluid. Sol Energy 2013;95:192–215.

[55] Hussein AK. Applications of nanotechnology to improve the performance of solar collectors–Recent advances and overview. Renew Sustain Energy Rev 2016;62:767–92.

[56] Wang Y, Xu J, Liu Q, Chen Y, Liu H. Performance analysis of a parabolic trough solar collector using Al2O3/synthetic oil nanofluid. Appl Therm Eng 2016;107:469–78.

[57] Ghasemi SE, Ranjbar A. Effect of nanoparticles in working fluid on thermal performance of solar parabolic trough collector. J Mol Liq 2016;222:156–66.

[58] Bellos E, Tzivanidis C, Antonopoulos KA. A detailed working fluid investigation for solar parabolic trough collectors. Appl Therm Eng 2017;114:374–86.

[59] Bellos E, Tzivanidis C. Thermal efficiency enhancement of nanofluid-based parabolic trough collectors. J Therm Anal Calorim 2019;135:597–608.

[60] Meyen S, Lüpfert E, Pernpeintner J, Fend T. Optical characterisation of reflector material for concentrating solar power technology 2009.

[61] Holze C, Brüggen H, Misseeuw R, Cosijns B, Albers R, Isaza D, et al. Laminated solar thin glass mirror solution for cost effective CSP systems 2013.

[62] AGC Glass Europe. AGC SOLAR MIRROR THIN 2020. https://www.agc-yourglass.com/sites/default/files/agc_docs/Factsheet_SolarMirrorThin_0820_EN.pdf.

[63] Alanod. Efficient solar solutions n.d. https://alanod.com/en/industries/solar.

[64] DiGrazia M, Jorgensen G. Reflectech mirror film: design flexibility and durability in reflecting solar applications. 39th ASES Natl. Sol. Conf., 2010, p. 1.

[65] Sagade AA, Aher S, Shinde NN. Performance evaluation of low-cost FRP parabolic trough reflector with mild steel receiver. Int J Energy Environ Eng 2013;4:5.

[66] Sagade AA, Shinde NN, Patil PS. Effect of receiver temperature on performance evaluation of silver coated selective surface compound parabolic reflector with top glass cover. Energy Procedia 2014;48:212–22.

[67] AGC Glass Europe. AGC SOLAR MIRROR THIN 2020.

[68] SCHOTT. SCHOTT PTR®70 n.d. https://www.us.schott.com/csp/english/schott-solar-ptr-70-receivers.html.

[69] SolarPower. UVAC Solar Receiver n.d. https://www.solarpowerworldonline.com/2010/08/uvac-solar-receiver-has-heat-loss-levels-below-9/.

[70] Bellos E, Tzivanidis C. Enhancing the performance of evacuated and non-evacuated parabolic trough collectors using twisted tape inserts, perforated plate inserts and internally finned absorber. Energies 2018;11:1129.

[71] Moya EZ. Parabolic-trough concentrating solar power systems. Conc. Sol. power Technol., Elsevier; 2021, p. 219–66.

[72] Li M, Wang LL. Investigation of evacuated tube heated by solar trough concentrating system. Energy Convers Manag 2006;47:3591–601.

[73] Daniel P, Joshi Y, Das AK. Numerical investigation of parabolic trough receiver performance with outer vacuum shell. Sol Energy 2011;85:1910–4.

[74] Kasaeian A, Daviran S, Azarian RD, Rashidi A. Performance evaluation and nanofluid using capability study of a solar parabolic trough collector. Energy Convers Manag 2015;89:368–75.

[75] Archimede Solarenergy Receiver Tube n.d. http://www.archimedesolarenergy.it/download.htm.

[76] Sohr O, Möllenhoff M, Kuckelkorn T. Laser induced release of encapsulated noble gas in SCHOTT receiver. Energy Procedia 2014;49:524–9.

[77] Weiss W, Rommel M. Solar heat for industrial processes. IEA SHC-TASK 2005;33.

[78] Usmani B, Harinipriya S. High-Temperature Solar Selective Coating. Syst. Think. Approach Soc. Probl., Springer; 2015, p. 181–9.

[79] Valdés A, Almanza R, Soria A. Determining the deflection magnitude of a steel receiver from a DSG parabolic trough concentrator under stratified flow conditions. Energy Procedia

2014;57:341–50.

[80] Khanna S, Singh S, Kedare SB. Effect of angle of incidence of sun rays on the bending of absorber tube of solar parabolic trough concentrator. Energy Procedia 2014;48:123–9.

[81] Fuqiang W, Jianyu T, Lanxin M, Chengchao W. Effects of glass cover on heat flux distribution for tube receiver with parabolic trough collector system. Energy Convers Manag 2015;90:47–52.

[82] Bortolato M, Dugaria S, Del Col D. Experimental study of a parabolic trough solar collector with flat bar-and-plate absorber during direct steam generation. Energy 2016;116:1039–50.

[83] Conrado LS, Rodriguez-Pulido A, Calderón G. Thermal performance of parabolic trough solar collectors. Renew Sustain Energy Rev 2017;67:1345–59.

[84] Prahl C, Röger M, Stanicki B, Hilgert C. Absorber tube displacement in parabolic trough collectors–A review and presentation of an airborne measurement approach. Sol Energy 2017;157:692–706.

[85] Potenza M, Milanese M, Colangelo G, de Risi A. Experimental investigation of transparent parabolic trough collector based on gas-phase nanofluid. Appl Energy 2017;203:560–70.

[86] Gong X, Wang F, Wang H, Tan J, Lai Q, Han H. Heat transfer enhancement analysis of tube receiver for parabolic trough solar collector with pin fin arrays inserting. Sol Energy 2017;144:185–202.

[87] Jamal-Abad MT, Saedodin S, Aminy M. Experimental investigation on a solar parabolic trough collector for absorber tube filled with porous media. Renew Energy 2017;107:156–63.

[88] Demagh Y, Hachicha AA, Benmoussa H, Kabar Y. Numerical investigation of a novel sinusoidal tube receiver for parabolic trough technology. Appl Energy 2018;218:494–510.

[89] Donga RK, Kumar S. Parabolic trough collector with rhombus tube absorber for higher concentration ratio. Energy Sources, Part A Recover Util Environ Eff 2018;40:2620–31.

[90] Meyer R, Schlecht M, Chhatbar K. Solar resources for concentrating solar power (CSP) systems. Conc. Sol. Power Technol., Elsevier; 2012, p. 68-e2.

[91] ISO EN. 9488: 1999. Sol Energy–Vocabulary 1999.

[92] Gama A, Larbes C, Malek A, Yettou F, Adouane B. Design and realization of a novel sun tracking system with absorber displacement for parabolic trough collectors. J Renew Sustain Energy 2013;5:33108.

[93] Kumar D, Kumar S. Thermal performance of the solar parabolic trough collector at different flow rates: an experimental study. Int J Ambient Energy 2018;39:93–102.

[94] Qu W, Wang R, Hong H, Sun J, Jin H. Test of a solar parabolic trough collector with rotatable axis tracking. Appl Energy 2017;207:7–17.

[95] Mageshwaran G, Ramachandran S, Gobinath K, DuraiRaj RB. Design of tracking system for helical-coiled receiver tube of parabolic trough collector. Int J Ambient Energy 2018;39:29–33.

[96] Janotte N, Feckler G, Kötter J, Decker S, Herrmann U, Schmitz M, et al. Dynamic performance evaluation of the HelioTrough® collector demonstration loop–towards a new benchmark in parabolic trough qualification. Energy Procedia 2014:109–17.

[97] Eck M, Hirsch T, Feldhoff JF, Kretschmann D, Dersch J, Morales AG, et al. Guidelines for CSP yield analysis–optical losses of line focusing systems; definitions, sensitivity analysis and modeling approaches. Energy Procedia 2014;49:1318–27.

[98] Osório T, Carvalho MJ. Testing of solar thermal collectors under transient conditions. Sol Energy 2014;104:71–81.

[99] Chaves JRF. Concentrated Solar Power: A comparison and evaluation of innovative parabolic trough collector concepts for large scale application. Technical University of Applied Sciences Wildau, 2019.

[100] Cleveland CJ, Morris CG. Handbook of energy: diagrams, charts, and tables. vol. 1. Newnes; 2013.

[101] Bellos E, Tzivanidis C. Alternative designs of parabolic trough solar collectors. Prog Energy Combust Sci 2019;71:81–117.

[102] Schenk H, Eck M. Yield Analysis for Parabolic Trough Solar Thermal Power Plants-A Basic Approach. DLR, Col 2012.

[103] Fuqiang W, Ziming C, Jianyu T, Yuan Y, Yong S, Linhua L. Progress in concentrated solar power technology with parabolic trough collector system: A comprehensive review. Renew Sustain Energy Rev 2017;79:1314–28.

[104] Lüpfert E, Riffelmann K-J, Price H, Burkholder F, Moss T. Experimental analysis of overall thermal properties of parabolic trough receivers. J Sol Energy Eng 2008;130.

[105] Dudley VE, Kolb GJ, Mahoney AR, Mancini TR, Matthews CW, Sloan M, et al. Test results: SEGS LS-2 solar collector. Sandia National Labs., Albuquerque, NM (United States); 1994.

[106] Burkholder F, Brandemuehl M, Price H, Netter J, Kutscher C, Wolfrum E. Parabolic trough receiver thermal testing. ASME 2007 Energy Sustain. Conf., American Society of Mechanical Engineers Digital Collection; 2007, p. 961–70.

[107] Burkholder F, Kutscher C. Heat-loss testing of Solel's UVAC3 parabolic trough receiver. National Renewable Energy Lab.(NREL), Golden, CO (United States); 2008.

[108] Burkholder F, Kutscher C. Heat loss testing of Schott's 2008 PTR70 parabolic trough receiver. National Renewable Energy Lab.(NREL), Golden, CO (United States); 2009.

[109] Márquez JM, López-Martín R, Valenzuela L, Zarza E. Test bench HEATREC for heat loss measurement on solar receiver tubes. AIP Conf. Proc., vol. 1734, AIP Publishing LLC;

2016, p. 30025.

[110] Dreyer S, Eichel P, Gnaedig T, Hacker Z, Janker S, Kuckelkorn T, et al. Heat loss measurements on parabolic trough receivers. 16th SolarPACES, Perpignon, Fr 2010:8.

[111] Hoste G, Schuknecht N. Thermal efficiency analysis of SkyFuel's advanced, large-aperture, parabolic trough collector. Energy Procedia 2015;69:96–105.

[112] Pernpeintner J, Schiricke B. Parabolic trough receiver heat loss measurement–Correction of absorber temperature over-prediction. AIP Conf. Proc., vol. 2126, AIP Publishing LLC; 2019, p. 120015.

[113] Sanchez M, Mateu E, Perez D, García P, Villuendas F, Heras C, et al. Optical and thermal characterization of solar receivers for parabolic trough collectors. Adv. Sci. Technol., vol. 74, Trans Tech Publ; 2010, p. 313–9.

[114] Keysight. 34970A Data Acquisition / Data Logger Switch Unit n.d. https://www.keysight.com/en/pd-1000001313%3Aepsg%3Apro-pn-34970a/data-acquisition-data-logger-switch-unit?cc=GB&lc=eng.

[115] Keysight. 34970A Data Acquisition / Data Logger Switch Unit n.d.

[116] SCHOTT PTR®70 Receiver Tube n.d. http://www.schott.com/d/csp/370a8801-3271-4b2a-a3e6-c0b5c78b01ae/1.0/schott_ptr70_4th_generation_brocure.pdf.

[117] Silva R, Pérez M, Fernández-Garcia A. Modeling and co-simulation of a parabolic trough solar plant for industrial process heat. Appl Energy 2013;106:287–300.

[118] Janotte N, Lüpfert E, Pitz-Paal R, Pottler K, Eck M, Zarza E, et al. Influence of measurement equipment on the uncertainty of performance data from test loops for concentrating solar collectors. J Sol Energy Eng 2010;132.

[119] Dieck RH. Measurement uncertainty: methods and applications. ISA; 2007.

[120] Padilla RV, Demirkaya G, Goswami DY, Stefanakos E, Rahman MM. Heat transfer analysis of parabolic trough solar receiver. Appl Energy 2011;88:5097–110.

[121] Yılmaz İH, Mwesigye A. Modeling, simulation and performance analysis of parabolic trough solar collectors: A comprehensive review. Appl Energy 2018;225:135–74.

[122] Patnode AM. Simulation and performance evaluation of parabolic trough solar power plants 2006.

[123] Edenburn MW. Performance analysis of a cylindrical parabolic focusing collector and comparison with experimental results. Sol Energy 1976;18:437–44.

[124] Ratzel AC, Hickox CE, Gartling DK. Techniques for reducing thermal conduction and natural convection heat losses in annular receiver geometries 1979.

[125] Clark JA. An analysis of the technical and economic performance of a parabolic trough concentrator for solar industrial process heat application. Int J Heat Mass Transf

1982;25:1427–38.

[126] Dudley V, Kolb G, Sloan M, Kearney D. SEGS LS2 solar collector-test results. Rep Sandia Natl Lab SANDIA94-1884, USA 1994.

[127] Thomas A, Thomas SA. Design data for the computation of thermal loss in the receiver of a parabolic trough concentrator. Energy Convers Manag 1994;35:555–68.

[128] Heidemann W, Spindler K, Hahne E. Steady-state and transient temperature field in the absorber tube of a direct steam generating solar collector. Int J Heat Mass Transf 1992;35:649–57.

[129] Forristall R. Heat transfer analysis and modeling of a parabolic trough solar receiver implemented in engineering equation solver. National Renewable Energy Lab., Golden, CO.(US); 2003.

[130] Cheng ZD, He YL, Xiao J, Tao YB, Xu RJ. Three-dimensional numerical study of heat transfer characteristics in the receiver tube of parabolic trough solar collector. Int Commun Heat Mass Transf 2010;37:782–7.

[131] He Y-L, Xiao J, Cheng Z-D, Tao Y-B. A MCRT and FVM coupled simulation method for energy conversion process in parabolic trough solar collector. Renew Energy 2011;36:976–85.

[132] Kalogirou SA. A detailed thermal model of a parabolic trough collector receiver. Energy 2012;48:298–306.

[133] Huang W, Hu P, Chen Z. Performance simulation of a parabolic trough solar collector. Sol Energy 2012;86:746–55.

[134] Hachicha AA, Rodríguez I, Capdevila R, Oliva A. Heat transfer analysis and numerical simulation of a parabolic trough solar collector. Appl Energy 2013;111:581–92.

[135] Wu Z, Li S, Yuan G, Lei D, Wang Z. Three-dimensional numerical study of heat transfer characteristics of parabolic trough receiver. Appl Energy 2014;113:902–11.

[136] Kumaresan G, Sudhakar P, Santosh R, Velraj R. Experimental and numerical studies of thermal performance enhancement in the receiver part of solar parabolic trough collectors. Renew Sustain Energy Rev 2017;77:1363–74.

[137] Multiphysics C. Heat transfer module user's guide. COMSOL Version 2014;4.

[138] COMSOL AB. COMSOL multiphysics reference manual, version 5.5. COMSOL AB 2019.

[139] Jaramillo OA, Venegas-Reyes E, Aguilar JO, Castrejón-García R, Sosa-Montemayor F. Parabolic trough concentrators for low enthalpy processes. Renew Energy 2013;60:529–39.

[140] Fernández-García A, Zarza E, Valenzuela L, Pérez M, Valcárcel E, Rojas E, et al. Development of a small-sized parabolic trough collector. Final Capsol project results. ISES Sol. World Congr. 2011, 2011.

[141] Macedo-Valencia J, Ramírez-Ávila J, Acosta R, Jaramillo OA, Aguilar JO. Design, construction and evaluation of parabolic trough collector as demonstrative prototype. Energy Procedia 2014;57:989–98.

[142] Bouvier J-L, Michaux G, Salagnac P, Nepveu F, Rochier D, Kientz T. Experimental characterisation of a solar parabolic trough collector used in a micro-CHP (micro-cogeneration) system with direct steam generation. Energy 2015;83:474–85.

[143] Yılmaz İH, Hayta H, Yumrutaş R, Söylemez MS. Performance testing of a parabolic trough collector array for a small-scale process heat application. ISI Bilim VE Tek DERGISI-JOURNAL Therm Sci Technol 2018;38:43–53.

[144] Chaudhary GQ, Kousar R, Ali M, Amar M, Amber KP, Lodhi SK, et al. Small-Sized Parabolic Trough Collector System for Solar Dehumidification Application: Design, Development, and Potential Assessment. Int J Photoenergy 2018;2018.

[145] Yang M, Moghimi MA, Zhu Y, Qiao R, Wang Y, Taylor RA. Optical and thermal performance analysis of a micro parabolic trough collector for building integration. Appl Energy 2020;260:114234.

[146] Norm M. ASHRAE standard 93. Methods of testing to determine thermal performance of solar collectors. ASHRAE Washington, DC, USA 2003.

[147] EN12975-2. EN 12975-2. Thermal solar systems and components-Solar collectors. Test Methods 2006.

[148] ISO9806:2017. ISO 9806:2017. Solar Energy-Solar Thermal Collectors-Test Methods. ISO; 2017.

[149] ASTM E905-87(2007). Standard Test Method for Determining Thermal Performance of Tracking Concentrating Solar Collectors. ASTM International, West Conshohocken; 2007.

[150] SRCC600. SRCC 600. Minimum standard for solar thermal concentrating collectors. Florida: Solar Rating and Certification Corporation (SRCC); 2014.

[151] Osório T, Carvalho MJ. Testing of solar thermal collectors under transient conditions. Energy Procedia 2012;30:1344–53.

[152] Fernández-García A, Valenzuela L, Zarza E, Rojas E, Pérez M, Hernández-Escobedo Q, et al. SMALL-SIZED parabolic-trough solar collectors: Development of a test loop and evaluation of testing conditions. Energy 2018;152:401–15.

[153] Pierucci G, Hosouli S, Messeri M, Salvestroni M, Fagioli F, Taddei F, et al. Realization of a test rig for small solar collectors and preliminary test. AIP Conf. Proc., vol. 2126, AIP Publishing LLC; 2019, p. 120016.

[154] Salvestroni M, Pierucci G, Fagioli F, Pourreza A, Messeri M, Taddei F, et al. Design of a small size PTC: computational model for the receiver tube and validation with heat loss test. IOP Conf. Ser. Mater. Sci. Eng., vol. 556, IOP Publishing; 2019, p. 12025.

[155] Pierucci G, Fontani D, Sansoni P, De Lucia M. Shape Optimization For Parabolic Troughs

Working In Non-Ideal Conditions. Energy Procedia 2014;57:2231–40.

[156] Bharti A, Mishra A, Paul B. Thermal performance analysis of small-sized solar parabolic trough collector using secondary reflectors. Int J Sustain Energy 2019;38:1002–22.

[157] Osório T. Solar thermal collectors under transient conditions: optical and thermal characterization based on the quasi-dynamic model 2011.

[158] Valenzuela L (SFERA2). Protocol for evaluation of optical quality, thermal losses and incident angle modifier of parabolic trough concentrators. 2014.

[159] Sabatelli V, Marano D, Braccio G, Sharma VK. Efficiency test of solar collectors: uncertainty in the estimation of regression parameters and sensitivity analysis. Energy Convers Manag 2002;43:2287–95.

[160] Gillett WB. The equivalence of outdoor and mixed indoor/outdoor solar collector testing. Sol Energy 1980;25:543–8.

Appendix A

Table A 1. Voltage, current and total power of test points for RT01.

Test	Q_{Main} Voltage (V)	Q_{Main} Current (A)	Total Power (W)	Test	Q_{Main} Voltage (V)	Q_{Main} Current (A)	Total Power (W)
1	1.730	0.168	0.291	26	8.080	0.845	6.829
2	1.730	0.168	0.291	27	8.449	0.881	7.444
3	2.495	0.255	0.637	28	8.449	0.881	7.440
4	2.647	0.272	0.721	29	8.449	0.973	9.089
5	3.315	0.341	1.131	30	9.338	0.973	9.087
6	3.315	0.341	1.130	31	9.700	1.007	9.767
7	3.573	0.375	1.338	32	9.700	1.008	9.778
8	3.573	0.374	1.338	33	10.065	1.045	10.517
9	4.098	0.430	1.762	34	10.064	1.041	10.478
10	4.098	0.430	1.762	35	10.474	1.086	11.371
11	4.678	0.490	2.293	36	10.474	1.085	11.361
12	4.673	0.488	2.282	37	10.982	1.138	12.495
13	5.209	0.543	2.831	38	10.982	1.138	12.494
14	5.209	0.543	2.831	39	11.294	1.171	13.228
15	5.592	0.582	3.255	40	11.294	1.171	13.228
16	5.592	0.582	3.255	41	11.757	1.217	14.309
17	6.189	0.648	4.010	42	11.756	1.216	14.295
18	6.189	0.648	4.010	43	13.439	1.389	18.660
19	6.687	0.697	4.664	44	13.438	1.388	18.653
20	6.689	0.698	4.666	45	13.644	1.410	19.239
21	7.179	0.750	5.384	46	13.644	1.410	19.233
22	7.180	0.750	5.384	47	14.144	1.455	20.578
23	7.723	0.809	6.245	48	14.144	1.455	20.577
24	7.724	0.809	6.245	49	14.626	1.499	21.917
25	8.080	0.845	6.828	50	14.759	1.504	22.197

Table A 2. Voltage, current and total power of test points for RT02.

Test	Q_{Main} Voltage (V)	Q_{Main} Current (A)	Total Power (W)	Test	Q_{Main} Voltage (V)	Q_{Main} Current (A)	Total Power (W)
1	1.506	0.155	0.226	21	10.040	1.052	10.554
2	1.321	0.136	0.172	22	10.090	1.043	10.521
3	2.549	0.265	0.674	23	10.838	1.128	12.224
4	2.549	0.265	0.674	24	10.838	1.127	12.215
5	3.680	0.383	1.408	25	11.536	1.205	13.898
6	3.680	0.383	1.407	26	11.677	1.214	14.172
7	4.552	0.473	2.150	27	12.471	1.297	16.165
8	4.552	0.473	2.151	28	12.471	1.295	16.147
9	5.452	0.566	3.078	29	13.264	1.381	18.309
10	5.452	0.565	3.077	30	13.265	1.379	18.289
11	6.210	0.646	4.006	31	14.111	1.467	20.701
12	6.210	0.646	4.004	32	14.111	1.467	20.696
13	6.978	0.726	5.058	33	14.967	1.559	23.327
14	6.978	0.726	5.058	34	14.967	1.558	23.313
15	7.727	0.803	6.203	35	14.938	1.558	23.264
16	7.727	0.803	6.201	36	14.938	1.557	23.254
17	8.542	0.897	7.660	37	14.938	1.556	23.240
18	8.493	0.885	7.509	38	14.938	1.557	23.243
19	9.233	0.958	8.847	39	14.938	1.556	23.239
20	9.234	0.960	8.865	40	14.938	1.557	23.246

Table A 3. Voltage, current and total power of test point for RT03.

Test	Q_{Main} Voltage (V)	Q_{Main} Current (A)	Total Power (W)	Test	Q_{Main} Voltage (V)	Q_{Main} Current (A)	Total Power (W)
1	1.097	0.113	0.116	18	7.184	0.751	5.376
2	1.097	0.113	0.118	19	7.889	0.826	6.495
3	2.345	0.245	0.564	20	7.888	0.825	6.487
4	2.345	0.245	0.565	21	8.574	0.898	7.679
5	3.101	0.325	0.997	22	8.574	0.898	7.678
6	3.101	0.325	0.995	23	9.403	0.979	9.174
7	3.769	0.394	1.470	24	9.403	0.979	9.179
8	3.769	0.394	1.470	25	10.152	1.058	10.707
9	4.580	0.480	2.184	26	10.152	1.057	10.701
10	4.580	0.480	2.183	27	10.776	1.123	12.068
11	5.239	0.551	2.874	28	10.777	1.122	12.061
12	5.239	0.551	2.872	29	11.566	1.205	13.913
13	5.917	0.621	3.653	30	11.566	1.202	13.883
14	5.917	0.620	3.654	31	12.242	1.273	15.561
15	6.550	0.685	4.470	32	12.286	1.276	15.653
16	6.550	0.685	4.468	33	13.130	1.364	17.873
17	7.184	0.751	5.378	34	13.126	1.363	17.857

Table A 4. Voltage, current and total power of test point for RT04.

Test	Q_{Main} Voltage (V)	Q_{Main} Current (A)	Total Power (W)	Test	Q_{Main} Voltage (V)	Q_{Main} Current (A)	Total Power (W)
1	6.628	0.682	4.519	7	11.044	1.145	12.645
2	6.628	0.681	4.515	8	11.128	1.158	12.883
3	9.496	0.985	9.350	9	12.611	1.305	16.461
4	9.496	0.984	9.346	10	12.611	1.304	16.448
5	9.496	0.984	9.343	11	14.574	1.513	22.053
6	11.045	1.145	12.643				

Table A 5. Voltage, current and total power of test point for RT05.

Test	Q_{Main} Voltage (V)	Q_{Main} Current (A)	Total Power (W)	Test	Q_{Main} Voltage (V)	Q_{Main} Current (A)	Total Power (W)
1	5.098	0.544	2.771	7	12.966	1.359	17.661
2	6.765	0.718	4.864	8	12.996	1.359	17.664
3	8.345	0.883	7.363	9	12.997	1.358	17.655
4	9.389	0.986	9.253	10	14.761	1.536	22.673
5	9.388	0.985	9.252	11	14.762	1.536	22.672
6	11.242	1.181	13.267				

Table A 6. Voltage, current and total power of test point for RT06.

Test	Q_{Main} Voltage (V)	Q_{Main} Current (A)	Total Power (W)	Test	Q_{Main} Voltage (V)	Q_{Main} Current (A)	Total Power (W)
1	4.936	0.518	2.556	9	11.035	1.153	12.7264
2	4.937	0.511	2.522	10	12.709	1.318	16.7510
3	6.496	0.681	4.422	11	12.709	1.318	16.7478
4	6.515	0.673	4.384	12	12.709	1.317	16.7430
5	7.986	0.837	6.682	13	14.358	1.486	21.3339
6	9.547	0.999	9.539	14	14.358	1.486	21.3313
7	9.652	1.011	9.823	15	15.170	1.568	23.7909
8	11.035	1.153	12.726	16	15.170	1.568	23.7884

Table A 7. Voltage, current and total power of test point for RT07.

Test	Q_{Main} Voltage (V)	Q_{Main} Current (A)	Total Power (W)	Test	Q_{Main} Voltage (V)	Q_{Main} Current (A)	Total Power (W)
1	5.141	0.530	2.724	8	9.798	1.005	9.837
2	5.141	0.530	2.724	9	11.311	1.171	13.240
3	6.782	0.696	4.719	10	12.897	1.341	17.279
4	6.782	0.696	4.719	11	12.897	1.341	17.285
5	8.245	0.856	7.059	12	14.491	1.510	21.882
6	8.245	0.856	7.059	13	14.491	1.510	21.879
7	9.798	1.005	9.837				

Table A 8. Voltage, current and total power of test point for RT08.

Test	Q_{Main} Voltage (V)	Q_{Main} Current (A)	Total Power (W)	Test	Q_{Main} Voltage (V)	Q_{Main} Current (A)	Total Power (W)
1	5.141	0.540	2.778	7	11.703	1.199	14.032
2	5.141	0.540	2.778	8	11.703	1.199	14.036
3	6.845	0.719	4.918	9	13.110	1.360	17.832
4	6.845	0.718	4.918	10	13.110	1.360	17.826
5	8.494	0.891	7.565	11	15.000	1.551	23.263
6	8.494	0.890	7.564	12	14.982	1.544	23.134

Table A 9. Voltage, current and total power of test point for RT09.

Test	Q_{Main} Voltage (V)	Q_{Main} Current (A)	Total Power (W)	Test	Q_{Main} Voltage (V)	Q_{Main} Current (A)	Total Power (W)
1	4.794	0.497	2.382	8	9.843	1.018	10.015
2	4.794	0.497	2.382	9	11.392	1.168	13.306
3	6.694	0.690	4.620	10	11.392	1.168	13.305
4	6.694	0.690	4.618	11	12.995	1.331	17.296
5	8.389	0.869	7.286	12	12.995	1.331	17.303
6	8.389	0.868	7.283	13	14.546	1.505	21.899
7	9.843	1.017	10.012	14	14.546	1.506	21.905

Table A 10. Voltage, current and total power of test point for RT10.

Test	Q_{Main} Voltage (V)	Q_{Main} Current (A)	Total Power (W)	Test	Q_{Main} Voltage (V)	Q_{Main} Current (A)	Total Power (W)
1	3.190	0.333	1.061	9	9.662	1.007	9.729
2	3.190	0.333	1.062	10	9.662	1.007	9.731
3	5.008	0.524	2.624	11	11.185	1.164	13.025
4	5.008	0.524	2.624	12	13.190	1.366	18.024
5	6.612	0.689	4.555	13	13.190	1.366	18.013
6	6.612	0.689	4.553	14	14.544	1.507	21.912
7	8.093	0.845	6.838	15	14.544	1.506	21.908
8	8.093	0.845	6.837				

Appendix B

Table B 1. Temperature variation along the RT01 receiver tube during the test points.

Test	TC1 (°C)	TC2 (°C)	TC3 (°C)	TC4 (°C)	TC5 (°C)	TC6 (°C)	TC-G1 (°C)	TC-G2 (°C)	TC-G3 (°C)	TC-G4 (°C)	T_{amb} (°C)
1	39	39	30	30	29	29	24	24	24	24	22
2	39	39	30	30	30	29	24	24	24	24	22
3	43	44	35	35	34	33	24	24	24	25	23
4	46	47	40	39	38	38	24	24	24	24	22
5	53	55	46	45	44	44	25	24	25	25	23
6	53	55	46	45	44	44	25	24	25	25	23
7	53	56	50	49	49	48	24	24	24	24	23
8	54	56	50	49	48	48	24	24	24	24	23
9	59	63	55	54	53	53	25	25	25	25	23
10	59	63	55	54	53	53	25	24	25	25	23
11	65	69	61	59	59	59	25	25	25	26	23
12	65	69	61	59	59	59	25	25	25	25	23
13	67	73	66	65	64	64	25	25	25	25	23
14	68	73	66	65	64	64	25	25	25	25	23
15	73	80	72	70	70	70	26	25	26	26	23
16	73	80	72	70	70	69	26	25	26	26	23
17	78	86	79	77	76	76	26	25	26	26	23
18	78	87	79	77	76	76	26	25	26	26	23
19	85	94	86	84	83	83	27	26	26	27	23
20	85	94	86	84	83	83	27	26	26	27	23
21	91	100	91	89	87	86	27	26	27	27	23
22	91	100	91	89	89	88	27	27	27	27	23
23	98	108	100	97	97	97	28	27	27	28	24
24	97	108	100	97	97	96	28	27	27	28	24
25	102	113	105	103	102	102	28	27	28	28	24
26	102	113	105	103	102	102	28	27	28	28	24
27	104	115	110	108	107	107	28	27	28	28	24
28	104	116	110	108	107	107	28	27	28	28	24
29	117	130	122	119	118	118	30	28	29	30	24
30	117	130	122	119	118	118	30	29	29	30	24
31	117	130	126	123	122	122	29	28	29	29	24
32	117	131	126	123	122	122	29	28	29	30	24
33	123	137	131	128	128	128	30	29	29	30	24
34	123	137	131	128	128	128	30	29	29	30	24
35	129	143	136	133	133	133	30	29	30	30	24
36	129	143	136	133	133	133	30	29	30	30	24
37	132	147	142	139	139	139	31	30	30	30	25
38	133	147	142	139	139	139	31	31	30	31	25
39	138	153	147	144	143	143	31	30	31	32	25
40	138	153	147	144	143	143	32	31	31	32	25
41	143	159	152	149	149	149	32	31	32	33	25
42	143	159	152	149	149	149	32	31	32	33	25
43	161	180	172	169	169	168	35	33	34	35	26
44	161	180	172	169	169	168	35	33	34	35	26
45	164	182	175	172	172	171	35	33	34	35	26
46	164	182	175	172	172	172	35	34	34	35	26
47	169	188	180	177	178	178	35	34	35	36	26
48	169	188	180	177	178	178	36	34	35	36	26
49	173	193	185	182	183	183	36	34	35	37	26
50	174	193	186	182	183	183	36	34	35	37	22

Table B 2. Temperature variation along the RT02 receiver tube during the test points.

Test	TC1 (°C)	TC2 (°C)	TC3 (°C)	TC4 (°C)	TC5 (°C)	TC6 (°C)	TC-G1 (°C)	TC-G2 (°C)	TC-G3 (°C)	TC-G4 (°C)	T_{amb} (°C)
1	38	38	31	30	31	30	27	27	27	27	26
2	39	38	31	31	30	30	27	27	27	27	26
3	47	48	40	40	39	39	27	27	28	28	26
4	47	48	40	40	39	39	28	28	28	28	26
5	56	58	51	50	49	49	28	28	28	28	26
6	56	59	51	50	49	49	28	28	28	28	26
7	64	68	60	60	58	58	28	28	28	29	26
8	64	68	60	60	58	58	29	29	28	29	26
9	66	72	71	70	67	66	28	28	27	28	26
10	67	73	71	70	67	67	28	28	28	28	26
11	76	84	80	80	77	76	28	29	28	29	26
12	77	85	80	80	77	76	29	29	29	29	26
13	86	96	91	90	87	86	29	29	29	30	26
14	86	96	91	90	87	86	29	30	29	30	26
15	95	106	101	99	96	96	30	30	30	31	26
16	95	106	101	99	96	96	30	30	30	31	26
17	99	112	111	110	108	107	29	30	29	30	26
18	105	117	111	110	106	106	31	31	30	32	26
19	107	122	120	119	115	115	30	30	30	31	26
20	108	122	120	119	115	115	30	31	30	31	26
21	118	134	130	129	125	125	31	31	31	32	26
22	120	135	131	129	126	125	31	32	31	32	26
23	129	146	141	139	135	135	32	33	32	33	26
24	129	146	141	139	136	135	32	33	32	33	26
25	137	155	150	149	144	144	32	33	32	34	26
26	139	156	151	149	145	145	32	34	33	34	26
27	143	163	160	159	154	154	32	33	32	34	26
28	143	163	160	159	155	154	32	34	33	34	26
29	156	176	171	169	165	164	33	35	34	36	26
30	156	176	171	169	165	164	33	35	34	36	26
31	165	186	181	178	174	174	34	36	35	37	26
32	165	186	181	178	175	175	34	36	35	37	26
33	174	197	190	188	184	183	35	37	36	38	26
34	175	197	191	188	185	184	35	37	36	38	26
35	173	196	191	188	183	181	35	37	35	38	26
36	174	196	191	188	184	183	35	37	35	38	26
37	174	196	191	189	184	183	35	37	36	38	26
38	174	196	191	189	184	183	35	37	36	38	26
39	174	197	191	189	185	184	35	37	36	38	26
40	175	197	191	189	185	184	35	37	36	38	26

Table B 3. Temperature variation along the RT03 receiver tube during the test points.

Test	TC1 (°C)	TC2 (°C)	TC3 (°C)	TC4 (°C)	TC5 (°C)	TC6 (°C)	TC-G1 (°C)	TC-G2 (°C)	TC-G3 (°C)	TC-G4 (°C)	T_{amb} (°C)
1	31	31	30	30	28	27	26	25	25	26	25
2	32	31	31	30	28	28	26	26	26	26	25
3	43	43	41	40	35	34	27	27	27	27	26
4	44	44	41	40	36	35	27	27	27	27	26
5	55	56	51	50	45	44	28	27	28	28	26
6	55	56	51	50	46	44	28	28	28	28	26
7	65	66	61	59	56	54	28	28	28	28	26
8	65	66	61	59	56	54	28	28	28	29	26
9	74	76	71	69	68	67	29	28	28	29	26
10	74	77	71	69	69	67	29	28	28	29	26
11	83	86	80	79	79	78	29	29	29	29	26
12	83	86	81	79	80	79	29	29	29	30	26
13	92	96	90	88	90	88	30	29	29	30	26
14	92	96	90	88	90	89	30	29	29	30	26
15	102	106	100	98	100	98	30	30	30	30	27
16	102	106	101	98	100	98	30	30	30	30	27
17	112	115	110	108	110	108	31	30	30	31	27
18	112	116	110	108	110	108	31	30	30	31	27
19	120	121	121	118	120	118	30	30	29	29	26
20	120	122	120	118	120	118	30	30	29	30	26
21	131	134	130	127	130	128	31	31	30	31	27
22	131	135	130	127	130	128	31	31	31	31	27
23	139	142	140	137	140	137	31	31	30	31	26
24	139	143	140	137	140	137	31	31	30	31	26
25	150	154	151	147	150	147	32	32	31	32	26
26	151	155	151	147	150	147	32	32	31	32	27
27	161	164	160	156	159	156	33	33	32	33	27
28	160	164	160	156	159	156	33	33	32	33	27
29	169	171	171	167	170	168	33	33	32	33	27
30	169	172	170	166	171	168	33	33	32	33	27
31	180	183	180	176	181	179	34	34	33	34	27
32	180	183	180	175	181	179	34	34	33	34	27
33	192	194	190	186	191	188	35	35	34	35	27
34	192	194	190	185	191	188	35	35	34	35	27

Table B 4. Temperature variation along the RT04 receiver tube during the test points.

Test	TC1 (°C)	TC2 (°C)	TC3 (°C)	TC4 (°C)	TC5 (°C)	TC6 (°C)	TC-G1 (°C)	TC-G2 (°C)	TC-G3 (°C)	TC-G4 (°C)	T_{amb} (°C)
1	84	84	80	77	77	83	24	24	24	25	21
2	84	84	81	77	77	83	24	24	24	25	21
3	122	127	119	114	114	123	24	24	24	25	21
4	122	127	119	114	113	123	24	24	24	25	21
5	122	127	119	114	113	123	24	24	24	25	21
6	141	146	139	133	133	146	24	24	24	25	20
7	141	147	139	133	133	146	24	24	24	25	21
8	142	148	140	135	133	145	24	24	24	25	19
9	161	166	159	153	153	168	24	24	24	25	21
10	161	167	159	153	153	168	24	24	24	25	21
11	183	189	182	175	173	189	24	24	24	25	19

Table B 5. Temperature variation along the RT05 receiver tube during the test points.

Test	TC1 (°C)	TC2 (°C)	TC3 (°C)	TC4 (°C)	TC5 (°C)	TC6 (°C)	TC-G1 (°C)	TC-G2 (°C)	TC-G3 (°C)	TC-G4 (°C)	T_{amb} (°C)
1	66	70	60	61	60	60	22	22	22	23	19
2	88	92	81	81	79	80	22	22	22	23	19
3	108	113	102	101	99	101	22	22	22	23	20
4	122	126	115	113	113	115	22	22	22	23	19
5	122	126	115	113	113	115	22	22	22	23	19
6	146	149	138	136	136	139	22	22	22	23	20
7	166	169	159	157	157	160	22	22	22	23	19
8	166	170	159	157	157	160	22	22	22	23	19
9	167	170	159	157	157	160	22	22	22	23	19
10	188	191	179	177	176	179	22	22	22	23	19
11	188	191	179	177	176	179	22	22	22	23	19

Table B 6. Temperature variation along the RT06 receiver tube during the test points.

Test	TC1 (°C)	TC2 (°C)	TC3 (°C)	TC4 (°C)	TC5 (°C)	TC6 (°C)	TC-G1 (°C)	TC-G2 (°C)	TC-G3 (°C)	TC-G4 (°C)	T_{amb} (°C)
1	60	68	60	60	61	62	21	21	21	21	18
2	59	66	59	59	61	62	21	21	21	21	19
3	77	88	79	79	82	82	21	21	21	21	19
4	77	87	78	78	81	82	21	21	21	21	19
5	95	108	99	99	102	103	21	21	21	21	19
6	112	128	120	119	124	124	21	21	21	21	19
7	112	128	120	119	124	125	21	21	21	21	19
8	130	147	139	139	144	145	21	21	21	21	19
9	130	147	139	139	145	145	21	21	21	21	19
10	147	165	159	158	165	165	21	21	21	21	20
11	147	165	158	158	165	165	21	21	21	21	20
12	147	165	158	158	165	165	21	21	21	21	20
13	166	186	177	177	186	186	21	21	21	21	20
14	166	186	177	177	186	186	21	21	21	21	20
15	175	196	187	186	195	195	21	21	21	21	20
16	175	196	187	186	195	195	21	21	21	21	20

Table B 7. Temperature variation along the RT07 receiver tube during the test points.

Test	TC1 (°C)	TC2 (°C)	TC3 (°C)	TC4 (°C)	TC5 (°C)	TC6 (°C)	TC-G1 (°C)	TC-G2 (°C)	TC-G3 (°C)	TC-G4 (°C)	T_{amb} (°C)
1	60	65	61	60	61	61	22	22	22	22	20
2	60	65	61	60	61	61	22	22	22	22	20
3	79	86	81	79	81	81	22	22	22	22	20
4	79	86	81	79	82	82	22	22	22	22	20
5	95	105	102	100	102	102	22	22	22	22	19
6	95	105	102	99	102	102	22	22	22	22	19
7	111	124	120	118	121	121	22	22	22	22	19
8	111	124	120	118	121	121	22	22	22	22	19
9	129	145	141	138	142	142	22	22	22	22	19
10	146	164	161	157	163	163	22	22	22	22	20
11	146	164	161	157	163	163	22	22	22	22	20
12	164	184	181	177	183	184	22	22	22	22	20
13	164	184	181	177	183	184	22	22	22	22	20

Table B 8. Temperature variation along the RT08 receiver tube during the test points.

Test	TC1 (°C)	TC2 (°C)	TC3 (°C)	TC4 (°C)	TC5 (°C)	TC6 (°C)	TC-G1 (°C)	TC-G2 (°C)	TC-G3 (°C)	TC-G4 (°C)	T_{amb} (°C)
1	62	67	60	60	60	62	22	22	22	22	19
2	62	68	60	60	60	62	22	22	22	22	19
3	80	90	82	81	80	82	22	22	22	22	19
4	80	91	82	81	80	82	22	22	22	22	19
5	99	112	104	101	99	100	22	22	22	22	19
6	99	112	104	101	99	100	22	22	22	22	19
7	133	150	143	139	136	137	22	22	22	22	20
8	133	150	143	139	137	137	22	22	22	22	20
9	151	171	162	158	155	156	22	22	22	22	20
10	151	171	162	158	156	156	22	22	22	22	20
11	170	192	183	178	177	177	22	22	22	22	20
12	170	192	183	179	177	177	22	22	22	22	20

Table B 9. Temperature variation along the RT09 receiver tube during the test points.

Test	TC1 (°C)	TC2 (°C)	TC3 (°C)	TC4 (°C)	TC5 (°C)	TC6 (°C)	TC-G1 (°C)	TC-G2 (°C)	TC-G3 (°C)	TC-G4 (°C)	T_{amb} (°C)
1	61	66	57	57	58	60	23	23	23	23	20
2	61	66	57	57	58	60	23	23	23	23	20
3	82	90	80	79	79	82	23	23	23	23	20
4	82	90	80	79	79	82	23	23	23	23	20
5	100	111	103	101	100	104	23	23	23	23	20
6	101	112	103	101	100	104	23	23	23	23	20
7	118	132	121	120	119	123	23	23	23	23	21
8	118	132	122	120	119	123	23	23	23	23	21
9	136	152	141	138	138	142	23	23	23	23	21
10	135	152	140	138	138	142	23	23	23	23	21
11	154	172	160	158	157	162	23	23	23	23	21
12	154	172	160	158	157	162	23	23	23	23	21
13	173	193	180	178	177	182	23	23	23	23	21
14	173	193	180	178	178	182	23	23	23	23	21

Table B 10. Temperature variation along the RT10 receiver tube during the test points.

Test	TC1 (°C)	TC2 (°C)	TC3 (°C)	TC4 (°C)	TC5 (°C)	TC6 (°C)	TC-G1 (°C)	TC-G2 (°C)	TC-G3 (°C)	TC-G4 (°C)	T_{amb} (°C)
1	43	43	39	40	41	41	22	22	22	22	20
2	43	43	39	40	41	41	22	22	22	22	20
3	61	65	59	60	60	60	22	22	22	22	20
4	61	65	59	60	60	60	22	22	22	22	20
5	77	85	79	80	80	80	22	22	22	22	20
6	77	84	79	80	80	81	22	22	22	22	20
7	94	103	99	100	101	102	22	22	22	22	20
8	94	104	99	100	101	102	22	22	22	22	20
9	111	123	119	120	122	122	22	22	22	22	20
10	111	123	119	119	122	122	22	22	22	22	20
11	129	143	138	139	142	142	22	22	22	22	21
12	147	163	161	161	166	167	22	22	22	22	21
13	147	163	161	161	166	167	22	22	22	22	21
14	164	181	177	177	184	185	22	22	22	22	21
15	164	181	176	177	184	185	22	22	22	22	21

Appendix C - Measurement uncertainties in solar collector efficiency testing (ISO 9806:2017)

The basic target of solar collector efficiency testing is the determination of the collector efficiency by measurements under specific conditions. More specifically, it is assumed that the behavior of the collector can be described by a M-parameter single node, steady-state or quasi-dynamic model:

$$\eta = c_1 p_1 + c_2 p_2 + \cdots + c_M p_M \qquad \textbf{(Eq. C 1)}$$

where

η is the collector instantaneous efficiency

$p_1, p_2, \ldots, p_M$ are quantities, the values of which are determined experimentally through testing

$c_1, c_2, \ldots, c_M$ are characteristic constants of the collector that are determined through testing

In the case of the steady-state model, for example, $M = 3$, $c_1 = \eta_0$, $c_2 = U_1$, $c_3 = U_2$, $p_1 = 1$, $p_2 = (T_m - T_a)/G$ and $p_3 = (T_m - T_a)^2/G$.

During the experimental phase, the output, solar energy and the basic climatic quantities are measured in J steady-state or quasi-dynamic state points, depending on the model used. From these primary measurements the values of parameters η, p_1, $p_2, \ldots, p_M$ are derived for each point of observation j, $j = 1 \ldots J$. Generally, the experimental procedure of the testing leads to a formation of a group of J observations which comprise, for each one of the J testing points, the values of η_j, $p_{1,j}$, $p_{2,j}, \ldots, p_{M,j}$. For the determination of uncertainties, it is essential to calculate the respective combined standard uncertainties $u(\eta_j)$, $u(p_{1,j})$, $\ldots u(p_{M,j})$ in each observations point. It should be noted that in practice the uncertainties $u(\eta_j)$, $u(p_{1,j})$, $\ldots u(p_{M,j})$ are almost never constant and the same for all points, but that each testing point has its own standard deviation.

During analyzing the data a least square fitting of the model formula is performed, in order to determine the values of coefficients $c_1, c_2, \ldots, c_M$ for which the model of Formula (Eq. C 1) represents the series of J observations with the greatest accuracy.

Since in reality the typical deviation is almost never constant and the same for all observations, but each data point (η_j, $p_{1,j}$, $p_{2,j}, \ldots, p_{M,j}$) has its own standard deviation σ_j, an interesting solution is the use of the **weighted least square (WLS)** method, which calculates, on the base of the measured values and their uncertainties, not only the model parameters but also their uncertainty. In the case of WLS, the maximum likelihood estimate of the model parameters is obtained by minimizing the chi-squared function:

$$\chi^2 = \sum_{J=1}^{J} \frac{(\eta_j - (c_1 p_{1,j} + c_2 p_{2,j} + \cdots c_N p_{M,j}))^2}{u_j^2} \qquad \textbf{(Eq. C 2)}$$

Where $u_j{}^2$ is the variance of the difference:

$$\eta_j - \left(c_1 p_{1,j} + c_2 p_{2,j} + \cdots c_N p_{M,j}\right) \qquad \textbf{(Eq. C 3)}$$

$$\boldsymbol{u_j^2 = \left(\eta_j - \left(c_1 p_{1,j} + c_2 p_{2,j} + \cdots c_N p_{M,j}\right)\right)}$$

$$\boldsymbol{= (u(\eta_j))^2 + c_1^2 (u\left(p_{1,j}\right))^2 + \cdots c_M^2 (u\left(p_{M,j}\right))^2}$$

Finding coefficients c_1, c_2,…,c_M and their standard uncertainties by minimizing chi-squared function is complicated, because of the nonlinearity present in Formula (Eq. C 2) A strategy is therefore to find these uncertainties numerically. A method for the case of a M-parameter model is presented below.

Let K be a matrix whose JxM components $k_{j,m}$ are constructed from M basic functions evaluated at the J experimental values of p_1, …,p_M weighted by the uncertainty u_j:

$$k_{j,m} = \frac{p_{m,j}}{u_j}, K = \begin{bmatrix} \frac{P_{1,1}}{u_1} & \cdots & \frac{P_{1,M}}{u_1} \\ \vdots & \ddots & \vdots \\ \frac{P_{1,J}}{u_J} & \cdots & \frac{P_{M,J}}{u_J} \end{bmatrix} \qquad \textbf{(Eq. C 4)}$$

Let also L be a vector of length J whose components l_j are constructed from values of η_j to be fitted, weighted by the uncertainty u_j:

$$I_j = \frac{\eta_j}{u_j}, L = \begin{bmatrix} \eta_1/u_1 \\ \vdots \\ \eta_j/u_j \end{bmatrix} \qquad \textbf{(Eq. C 5)}$$

The normal formula of the least square problem can be written:

$$(K^T \cdot K) \cdot C = K^T \cdot L \qquad \textbf{(Eq. C 6)}$$

where C is a vector whose elements are the fitted coefficients. Given the fact that for the calculation of variances u_j^2 the knowledge of coefficients c_1, c_2,…,c_M is needed, a possible solution is to use the values of coefficients calculated by standard least squares fitting as the initial values. These initial values can be used in Formula (Eq. C 3) for the calculation of u_j^2 , $J = 1 \ldots J$ and the formation of matrix K and of vector L. The solution of Formula (Eq. C 6) gives the new values of coefficients c_1, c_2,…,c_M, which however are not expected to differ noticeably from those calculated by standard least squares fitting and used as initial values for the calculation of u_j^2.

Moreover, $Z = INV(K^T \cdot K)$ is a matrix whose diagonal elements $z_{k,k}$ are the squared uncertainties (variances) and the off-diagonal elements $z_{k,l} = z_{l,k}$, $k \neq l$ are the covariance between fitted coefficients:

$$u(c_m) = \sqrt{z_{m,m}} \quad ; m = 1, \dots, M \qquad \textbf{(Eq. C 7)}$$

$$Cov(c_k, c_l) = z_{k,l} = z_{l,k}\ , k = 1, \dots, M\ and\ l = 1, \dots, M\ and\ k \neq 1 \qquad \textbf{(Eq. C 8)}$$

The term combined standard uncertainty means the standard uncertainty in a result when that result is obtained from the values of a number of other quantities. In most cases a measured Y is determined indirectly from P other directly measured quantities X_1, X_2, ...X_P through a functional relationship $Y = f(X_1, X_2, \dots X_P)$. The standard uncertainty in the estimate y is given by the law of error propagation:

$$u(y) = \left(\sum_{i=1}^{P} \left(\frac{\partial f}{\partial x_i} \right)^2 (u(x_i))^2 + 2 \sum_{i=1}^{P-1} \sum_{j=i+1}^{P} \frac{\partial f}{\partial x_i} \frac{\partial f}{\partial x_j} cov(x_i, x_j) \right)^{1/2} \qquad \textbf{(Eq. C 9)}$$

It should be noted that the knowledge of covariance between the fitted coefficients is necessary if one wishes to calculate, in a next stage, the uncertainty $u(\eta)$ in the predicted values of η using Formula (Eq. C 1) and Formula (Eq. C 1). Formula (Eq. C 6) can be solved by a standard numerical method, for example, by Gauss-Jordan elimination.

Appendix D - A detailed review on solar parabolic trough collector

Title of Paper	Journal	Year	Authors	Objectives	Critics outcomes
Design, manufacture and testing of fibreglass reinforced parabola trough for parabolic trough solar collectors Indian Standard time	*Solar energy*	2007	A. V. Arasu and T. Sornakumar	Design and mfg. Smooth 90° rim angles, 7mm thick fibreglass, reinforced parabolic trough by hand layup method.	FRP trough tested at a wind speed of 34 m/s & found within acceptable limits.
Concentrating solar power - Technology, potential and policy in India	*Renew. Sustain. Energy Rev.*	2011	A. Summarising and M. S. Soni	Discussed global and Indian CPC policies, compatibility and need of such technology in India and details about available technology and types of CSP with comparisons.	Gujarat and Rajasthan are in a solar belt for harvesting maximum solar energy
A new system to produce cooling and power using solar thermal energy	*Energy Sources, Part A Recover. Util. Environ. Eff.,*	2011	Z. S. Abdel-Rehim	In this study, A new system to produce cooling and power with the energy obtained from low-temperature as a thermal resource is presented. This resource can be obtained from concentrating solar thermal energy or parabolic trough.	The theoretical study is presented, which identifies expander inlet conditions, expander efficiency, and exhaust pressure as the factors determining exhaust temperature. It is concluded that the proposed system improves expander performance, output power, and cooling production and can be satisfied with this concept.
Energy for Sustainable Development Solar collector field design and viability analysis of stand-alone parabolic trough power plants for Indian conditions	*Energy Sustain. Dev.*	2012	K. S. Reddy and K. R. Kumar	Analysis of solar parabolic trough collector field for power generation is carried out using different working fluids like oil and water of 58 locations in India. SPTC field has been designed using MAT Lab 7.0.1.	Optimum configuration of the collector field is found as 6m angle of 65° has been considered.Jodhpur is considered as the reference location
Performance studies of a solar parabolic trough collector with a thermal energy storage system	*Energy*	2012	G. Kumaresan, R. Sridhar, and R. Velraj	Experimental study is carried out to investigate the performance of a solar parabolic trough collector (PTC) integrated with a storage unit. HTFTherminol 55	Max. Temp 212°C at noon & 116°C at outlet. For minimising heat loss, PTC locates very close to storage tank & insulate properly.
Object-oriented modelling for the transient performance simulation of parabolic trough collectors using molten salt as the heat transfer fluid	*Solar energy*	2013	M. Sa, F. Zaversky, R. Medina, J. Garcı, and D. Astrain	Transient modelling of parabolic trough solar collectors that use molten salt, a mixture of 60% NaNO3 and 40% KNO3 (weight percent), as the heat transfer fluid	Max temp achieved was 520°C and average min. Temp. was 352°C
Performance evaluation of low-cost FRP parabolic trough reflector with a mild steel receiver,	*Int. J. Energy Environ. Eng.*	2013	A. a Sagade, S. Aher, and N. N. Shinde	Discussed the experimental results of the prototype parabolic trough made of fibreglass-reinforced plastic with its aperture area coated by aluminium foil with a reflectivity of 0.86.	Instantaneous efficiency of 51% and 39% have been achieved with and without glass cover
Design and realization of a novel sun tracking system with absorber displacement for parabolic trough collectors	*Jnl. Renew. Sustain. Energy*	2013	Fatiha yet to, Amor gama, Cherif larbes, Malek ali	In this paper, authors propose and describe a new single axis sun tracking system that has a moveable absorber which can be adjusted to minimise the optical losses caused by the cosine effect in parabolic trough concentrators (PTC).	Authors observe that the efficiency of our new sun tracking system with reflector displacement is in between the efficiency of one and two axes sun tracking.
Thermal energy storage technologies and systems for concentrating solar power plants	*Prog. Energy Combust. Sci*	2013	S. Kuravi, J. Trahan, D. Y. Goswami, M. M. Rahman, and E. K. Stefanakos	A review of thermal energy storage system design methodologies and the factors to be considered at different hierarchical levels for concentrating solar power (CSP) plants.	Final results indicated that the hightemperature concrete is suitable for use as a sensible heat storage material up to 500°C

(continued).

Title of Paper	Journal	Year	Authors	Objectives	Critics outcomes
Use of parabolic trough solar collectors for solar refrigeration and air-conditioning applications	*Renew. Sustain. Energy Rev*	2013	M. Pe, F. J. Cabrera, and A. Ferna	Comprehensive literature survey on worldwide air-conditioning and refrigeration facilities fed by a PTC solar field	PTC present similar costs of energy for cooling than flat plate collector (FPC) and lower than evacuated tube collectors (ETC) and compound parabolic collectors (CPC).
Design and performance characteristics of solar adsorption refrigeration system using parabolic trough collector: Experimental and statistical optimisation technique	*Energy Convers. Manag*	2013	N. H. Abu-hamdeh, K. A. Alnefaie, and K. H. Almitani	The developed model of a solar adsorption refrigeration system can be employed as a refrigerator and cooler unit suitable for remote areas.	Highest COP obtained 0.75. The highest temperature reached by the collector was 120°C
Wind engineering analysis of parabolic trough solar collectors: The effects of varying the trough depth,	*Jnl.Wind Eng. Ind. Aerodyn.*	2014	J. Paetzold, S. Cochard, A. Vassallo, and D. F. Fletcher	Airflow is investigated in a parametric study reduction of the wind load thermal sand losses in the receiver tubes to provide a basis for higher concentration ratios Series of three-dimensional simulations were conducted using the commercial CFD programme ANSYS CFX 14.5.	Most significant overall forces on the PTC are generally observed at pitch angles larger than 15° and smaller than -60°.
Design and Construction of a Parabolic Trough Solar Collector for Process Heat Production	*Energy Procedia*	2014	I. Eleazar, P. Montes, A. Mejia, and O. Mercado	His paper presented the results of designing a parabolic trough solar collector (PTSC), and its application in a solar thermal system for the production of process heat. Implementing a series of innovations in the structural form, the material selection and the adoption of new manufacturing processes; enables a faster erection on installation site and reduction in production costs.	The peak temperature has been 80°C, which coincides with the preliminary design information for solar radiation conditions above 19 MJ/m^2/day, in a day with excellent weather conditions.
Effect of receiver temperature on performance evaluation of silver coated selective surface compound parabolic reflector with a top glass cover	*Energy Procedia*	2014	A. A. Sagade, N. N. Shinde, and P. S. Patil	Experimental results of the prototype compound parabolic trough solar collector made of mild steel and its surface coated with an aluminium foil of thickness 10microns as a selective surface with top cover	The average efficiency of 59.8% with a mass flow rate of 0.011Kg/S average 68°C temperature is attained by the black copper coated receiver with a maximum temperature of 76°C
Effect of angle of incidence of sun rays on the bending of absorber tube of solar parabolic trough concentrator	*Energy Procedia*	2014	S. Khanna, S. Singh, and S. B. Kedare	An analytical expression is derived for finding the deflection in the central axis of the absorber tube from the focal line of the trough.	Results show that the absorber tube will not deflect from the focal line at Ψ=0°. However, it will deflect during non-zero angle of incidence because the sun facing the end of absorber tube does not receive any concentrated rays
Determining the deflection magnitude of a steel receiver from a DSG parabolic trough concentrator under stratified flow conditions	*Energy Procedia*	2014	A. Valdes, R. Almanza, and A. Soria	The purpose of this study is to determine the magnitude of the deformation of the receiver of a direct steam-generating system based on the angular distribution of temperature obtained from the water flow rate for a parabolic trough collector under stratified conditions	Themodel results lie within a range of ±10% from experimental data.
Optical and thermal evaluations of a medium temperature parabolic trough solar collector used in a cooling installation	*Energy Convers. Manag*	2014	M. Balghouthi, A. Bel, H. Ali, S. E. Trabelsi, and A. Guizani	Optical evaluations of the collectors using photogrammetric techniques were performed. The analysis and readjustments of the optical results were conducted using Matlab code.	Values of the overall optical efficiency were 0.48 and 0.514.

(continued).

Title of Paper	Journal	Year	Authors	Objectives	Critics outcomes
Design of semi-static solar concentrator for charcoal Production	*Energy Procedia*	2014	G. Ramos and D. Perez-Marquez	Non-tracking type design of solar oven capable of producing charcoal out of wood, Evacuated tube isolation resulted in a mean temperature of 309°C	At typical irradiance of 800 W/m^2 efficiency is 380 kg per ton.
Performance study on evacuated tube solar collector using therminol D-12 as heat transfer fluid coupled with the parabolic trough,	*Energy Convers. Manag*	2014	P. Selvakumar, P. Somasundaram, and P. Thangavel	A new system with evacuated tube collector using synthetic oil as heat transfer fluid coupled with a parabolic trough is developed and studied experimentally for instant hot water generation in the presence of low solar irradiance	Evacuated tube using therminol D-12 as heat transfer fluid coupled to parabolic trough can produce instant hot water at temperatures between 40°C and 68°C under low solar radiation.
Numerical simulation of solar parabolic trough collector performance in the Algeria Saharan region	*Energy Convers. Manag*	2014	Y. Marif, H. Benmoussa, H. Bouguettaia, M. M. Belhadj, and M. Zerrouki	Authors determine the optical and thermal performance of a solar parabolic trough collector under the climate conditions of Algerian Sahara	For low temperatures (T < 100°C) such as domestic hot water, water distillation, air-conditioning and refrigeration. For very high temperatures application it is necessary to use synthetic oil.
ULTIMATE TROUGH ® - Fabrication, erection and commissioning of the world's largest parabolic trough collector	*Energy Procedia*	2014	A. Schweitzer, W. Schiel, M. Birkle, P. Nava, K. Riffelmann, and A. Wohlfahrt	This paper discussed the development of the Ultimate Trough started in 2010, a prototype was installed and tested in 2011, and the test loop was launched in 2012.	It is expected that this collector reduces the solar field cost by 20-25%.
A novel parabolic trough solar collector model – Validation with experimental data and comparison to Engineering Equation Solver (EES)	*Energy Convers. Manag*	2015	O. Behar, A. Khellaf, and K. Mohammedi,	The validation has been carried out through a comparison with results of previous studies conducted in theworldwide most renowned laboratories, i.e. Sandia National Laboratory (SNL) and National Renewable Energy Laboratory (NERL).	The proposed model has a slight deviation in the estimation of heat losses at higher operation temperatures
Effects of glass cover on heat flux distribution for tube receiver with parabolic trough collector system	*Energy Convers. Manag*	2015	W. Fuqiang, T. Jianyu, M. Lanxin, and W. Chengchao	Effects of a glass cover (GC) on heat flux distribution are analysed by Monte Carlo Ray Tracing (MCRT) method	Adopting a GC with an elliptic-circular cross-section for the tube receiver can effectively decrease the heat flux gradient, the peak heat flux reduction is up to 32.3%.
A new desalination system using a combination of a heat pipe, evacuated tube and parabolic trough collector	*Energy Convers. Manag*	2015	H. J. Mosleh, S. J. Mamouri, M. B. Shafii, and A. H. Sima	Combination of a heat pipe and a twin-glass evacuated tube collector is utilised with a parabolic trough collector	Cost analysis of the system showed that the CPL value for 25 years of operation is 0.0450 $\$/l/m^2$, which is higher compared to some of the other recent works
Year-round performance assessment of a solar parabolic trough collector under the climatic condition of Bhiwani, India: A case study	*Energy Convers. Manag*	2015	D. Kumar and S. Kumar	Comprehensive thermo-optical modelling has been proposed to evaluate the performance of a mini-level SPTC considering various heat equilibriums with the environment. The collector consists of a non-evacuated receiver tube with black paint coating and enveloped with a glass cover	Maximum optical efficiency is attained as 72.26% and 72.4% on horizontal and an inclined plane, respectively. Peak instantaneous thermal efficiency is accomplished as 66.78% in July on a horizontal plane, 65.77% in September on the inclined plane of the collector

(continued).

Title of Paper	Journal	Year	Authors	Objectives	Critics outcomes
A review of solar parabolic trough collector	*Renew. Sustain. Energy Rev.*	2016	V. K. Jebasingh and G. M. J. Herbert,	Reviews the related applications of solar energy such as air heating system, desalination, refrigeration, industrial heating purposes and power plants.	The thermal storage system on solar PTC makes a future pathway for many thermal applications. Since the phase change from solid to liquid, it is made to store much energy that can be used for night time and also during cloudy days.
Applications of nanotechnology to improve the performance of solar collectors – Recent advances and overview	*Renew. Sustain. Energy Rev.*	2016	A. K. Hussein	Detail overview of the recent advances related to the application of the nanotechnology in various kinds of solar collectors.	It was found that SiO2-H2O based nanofluid had comparatively higher efficiency at higher volume flow rates.
Performance analysis of a parabolic trough solar collector using Al2O3/synthetic oil nanofluid	*Appl. Therm. Eng*	2016	Y.Wang, J. Xu, Q. Liu, Y. Chen and H. Liu	In this paper, the applications of nanofluids on the parabolic trough collector (PTC) systems are investigated	It was found that using water-based CuO nanofluids could significantly enhance the efficiency compared with pure water
Effect of Nanoparticles in Working Fluid on Thermal performance of Solar parabolic Trough collector	*J. Mol. Liq*	2016	S. E. Ghasemi and A. Ranjbar	In this work, forced convection heat transfer turbulent flow inside the receiver tube of solar parabolic trough collector with nanofluids as working fluid is numerically simulated	Results showed that the adding of nanoparticles produced a considerable enhancement of the Nusselt number concerning that of the base fluid.
A detailed working fluid investigation for solar parabolic trough collectors	*Appl. Therm. Eng*	2016	E. Bellos, C. Tzivanidis, and K. A. Antonopoulos	Pressurised water, Therminol VP-1, molten nitrate salt, sodium liquid, air, carbon dioxide and helium are the examined working fluids	The thermal analysis is performed with the EES tool.
Experimental study of a parabolic trough solar collector with flat bar-and-plate absorber during direct steam generation	*Energy*	2016	M. Bortolato, S. Dugaria, and D. Del	The present work aims at investigating an innovative flat aluminium absorber for process heat and direct steam generation in small linear solar concentrating collectors	The results show that a promising overall thermal efficiency of 64% at 0.160 K m^2 W can be achieved with a negligible pressure drop
Solar parabolic trough collectors: A review on heat transfer augmentation techniques	*Renew. Sustain. Energy Rev*	2016	H. M. Sandeep and U. C. Arunachala	The present study is focused on analysis and feasibility of various heat transfer augmentation techniques for PTC receiver. These include the use of evacuated receivers, nanofluids with/ without inserts and use of supplements with base fluids	The enhanced heat transfer in laminar regime was 20%-300% for base fluid with insert compared to that in the plain receiver. Similarly, the rise was 30% – 50% for nanofluid with insert
The use of parabolic trough collectors for solar cooling – A case study for Athens climate	*Case Stud. Therm. Eng*	2016	C. Tzivanidis and E. Bellos	Examined one stage water/lithium-bromide absorption chiller powered by a PTC coupled with a storage tank.	It is found that a PTC module with an aperture area of 14m^2 and a building area of about 25m^2 can be cooled for 13 h daily during the summer season
An experimental investigation on a small-sized parabolic trough solar collector for water heating in cold areas	*Appl. Energy*	2016	B. Zou, J. Dong, Y. Yao and Y. Jiang	Particular small-sized parabolic trough solar collector (PTC) proposed for water heating in cold areas. An experimental platform was developed, and extensive tests were conducted to evaluate the characteristics of the proposed PTC	HTF synthetic thermal oil with a freezing point of −30°C. The thermal efficiency of the proposed PTC reached about 67% even under the condition of solar radiation of less than 310 W/m^2
Study of Applications of Parabolic Trough Solar Collector Technology in Mexican Industry	*Energy Procedia*	2016	P. D. Tagle, A. Agraz, and C. I. Rivera	Two systems installed comparing the results with computational and experimental data.	The model predicts the thermal output with around 10% of error in the accuracy
Development and performance assessment of a parabolic trough solar collector-based integrated system for an ice-cream factory	*Energy*	2016	O. Kizilkan, A. Kabul, and I. Dincer	In this paper, a new solar-based renewable energy system integrated with PTSCs (parabolic trough solar collectors) is proposed, designed and analysed for an ice-cream factory located in Isparta, Turkey	The results show that the energy consumption of the actual system is 85.81 kWh per day, while the energy consumption of the proposed method is calculated to be 1.235 kWh which leads to an energy saving of 98.56%.

(continued).

Title of Paper	Journal	Year	Authors	Objectives	Critics outcomes
Experimental investigation of solar cooker during sunshine and off-sunshine hours using thermal energy storage unit based on parabolic trough collector,	*Int. J. Ambient Energy,*	2016	K. S. & A. Y. Gagandeep Sainia, Harvinder Singha,	A solar cooker based on parabolic trough collector with thermal energy storage was investigated. In this experimental setup, solar radiations were focused on the absorber tube, and the collected heat was transferred to the solar cooker by natural circulation (thermosiphon) of working fluid.	Using hot oil as working fluid, the quantity of heat stored by PCM was increased by an amount of 19.45% to 30.38% as compared to water.
Parabolic Trough Collector, a Novel Design for Domestic Water Heating Application	*IJRASET*	2017	B. H. Upadhyay, A. J. Patel, and P. V Ramana	The aim is to design a novel parabolic trough collector which is useful in low-temperature applications like domestic water heating.	The modern design also allows for changing the trough length. The model has provision for attaching an automatic tracking system and storage device
A detailed study on the optical performance of parabolic trough solar collectors withMonte Carlo Ray Tracingmethod based on theoretical analysis	*Sol. Energy*	2017	B. Zou, J. Dong, Y. Yao and Y. Jiang	MCRT models are established, and the theoretical equations of several critical parameters are derived firstly. And then the effects of different geometrical parameters on the optical performance are discussed in detail.	The presentwork will study in depth the optical performance of PTCs under conditions of zero incident angle
Thermal performance of parabolic trough solar collectors,	*Renew. Sustain. Energy Rev*	2017	L. S. Conrado, A. Rodriguez-pulido, and G. Calderon	Presents a review of the thermal performance, various types of mathematical models, simulation and numerical methods, and experimental setups of PTC.	The primary goal is to study the principal thermal aspects that need to be considered in future developments
Absorber tube displacement in parabolic trough collectors – A review and presentation of an airborne measurement approach	*Sol. Energy*	2017	C. Prahl,M. Roger, B. Stanicki, and C. Hilgert	This paper provides a comprehensive overview of the causes and effects of absorber tube displacement and state of the art measurement techniques.	Authors present an airborne approach, which delivers mirror shape and absorber tube position with an integrated, airborne measurement system.
Experimental investigation of transparent parabolic trough collector based on gas-phase nanofluid	*Appl. Energy*	2017	M. Potenza, M. Milanese, G. Colangelo, and A. De Risi	A preliminary study on new high-temperature parabolic trough collector (PTC), with transparent receiver tube, based on gasphase nanofluid, has been carried out for the first time	The fluid temperature higher than 145°C has been maintained for about 10 h, reaching a maximum value of 180°C, with lowefficiency of about 65%.
Modelling and simulation of a novel Electrical Energy Storage (EES) Receiver for Solar Parabolic Trough Collector (PTC) power plants	*Appl. Energy*	2017	D. D. Nation, P. J. Heggs, and D. W. Dixon-hardy	Mathematical modelling of a novel Electrical Energy Storage (EES) Receiver for PTC.EES receiver is essentially a Heat Collecting Element (HCE) with built-in electrical storage in the form of thermal batteries such as the Sodium Sulphur (NaS) battery.	The heat flux conducted through the absorber wall flux, which was solved using the goal seeks tool available in Microsoft Excel.
Heat transfer enhancement analysis of tube receiver for parabolic trough solar collector with pin fin arrays inserting	*Sol. Energy*	2017	G. Xiangtao, W. Fuqiang, W. Haiyan, T. Jianyu, L. Qingzhi, and H. Huaizhi	Numerical results have been compared with experimental results conducted in the DISS test facility in Spain.	The max temperature gradient on the cross section for PFAI-PTR is 15.0% less than that of PTR, and the high- temperature region with temperature larger than 206°C disappeared when the pin fin arrays are inserted in the absorber tube of PTR
Experimental investigation on a solar parabolic trough collector for absorber tube filled with porous media	*Renew. Energy*	2017	M. T. Jamal-abad, S. Saedodin, and M. Aminy	The efficiency of a solar parabolic trough has been investigated experimentally. An absorber filled with metal foam is used to improve the heat transfer and increase the efficiency of PTC	The overall loss coefficient UL decreases by 45%, and it causes to increase efficiency because less energy is lost.

(continued).

Title of Paper	Journal	Year	Authors	Objectives	Critics outcomes
A new approach for obtaining the angular acceptance function of non-perfect parabolic concentrating collectors	*Sol. Energy*	2017	N. Fraidenraich, M. Henrique, D. O. P. Filho, and O. De	A new approach to calculate the angular acceptance function of cylindrical parabolic collectors has been developed. The procedure is rapid, simple and enables obtaining the acceptance function with or without absorber deviations	When only linear displacement exists, significant optical losses are observed from d > 0.5 Rabs on. However, the absorber is seen, almost with the same view angle from both sides of the reflector, (h > 0) and (h < 0), for even large displacements (1.0/Rabs).
Test of a solar parabolic trough collector with rotatable axis tracking	*Appl. Energy*	2017	W. Qu, R.Wang, H. Hong, J. Sun, and H. Jin	In summer, the solar incidence angle is small, and the north-south axis tracking is adopted. In winter, the solar incidence angle is large, and the cosine loss is severe, so using the rotatable axis tracking enables more solar irradiation to be harvested	The experimental results show that, by using the rotatable axis tracking, the daily average efficiency can be enhanced from 43% to 48% in winter
Materials selection for thermal energy storage systems in parabolic trough collector solar facilities using high chloride content nitrate salts	*Sol. Energy Mater. Sol. Cells*	2017	F. J. Ruiz-cabanas, C. Prieto, V. Madina, A. I. Fernandez, and L. F. Cabeza	A516 Gr70 carbon steel corrosion performance evaluation under high-chlorides content nitrates salts (1.2% and 3% by weight) at 400°C.	Current materials selection should be replaced by higher corrosion resistant alloys being the Cr-Mo steels, martensitic stainless steels and ferritic stainless steels a first approach to be evaluated
Progress in concentrated solar power technology with parabolic trough collector system: A comprehensive review	*Renew. Sustain. Energy Rev*	2017	W. Fuqiang, C. Ziming, T. Jianyu, Y. Yuan, S. Yong, and L. Linhua	This review first covered the theoretical framework of CSP technology with a PTC system. Next, the detailed derivation process of the maximum theoretical concentration ratio of the PTC was initially given.	Various types of heat transfer fluids in tube receivers were reviewed to present the capability of the application. Moreover, recent developments on heat transfer enhancement methods for CSP technology with a PTC system were highlighted
Review of solar parabolic-trough collector geometrical and thermal analyses, performance, and applications	*Renew. Sustain. Energy Rev.,*	2018	A. Jaber, N. Mariah, M. Zainal, A. Ab-kadir, and A. Aziz	This review contains geometrical analysis, including the thermal approach of the PTC model, heat transfer, and method of enhancing thermal efficiency on the PTC receiver.	Also includes performance analysis, thermal efficiency, and applications of the solarpowered PTC and the history of PTC evolution.
Design analysis of solar parabolic trough thermal collectors,	*Renew. Sustain. Energy Rev.,*	2018	A. Z. Hafez et al	This paper presents a review of the design parameters, mathematical techniques and simulations used in the design of parabolic trough solar systems, along with a discussion on their applications.	The paper also discusses the different kinds of software and test methods of solar collectors
Experimental and numerical study of parabolic trough solar collector of MicroSol-R tests platform	*Exp. Therm. Fluid Sci.*	2018	B. Agagna, A. Smaili, Q. Falcoz, and O. Behar	PROMES-CNRS laboratory has recently inaugurated a small scale parabolic trough power plant, named “MicroSol-R“, for research activities is aimed to test and improve various technologies including thermal energy storage, power conversion cycle, heat transfer fluid and collectors.	The main goal is to identify the advantages and the limitations of each model to the others, and therefore, selecting the most suitable tool for modelling the PTCs.
Numerical investigation of a novel sinusoidal tube receiver for parabolic trough technology	*Appl. Energy*	2018	E. W. Bitam, Y. Demagh, A. A. Hachicha, H., Benmoussa, and Y. Kabar	In this study, a numerical approach has been developed to analyse the possible improvement in the PTC performances by replacing the conventional straight tube receiver by a newly designed one with a longitudinally curved shape.	The average Nusselt number is increased up to 45%–63%. The average friction coefficient increases of less than 40.8%.

(continued).

Title of Paper	Journal	Year	Authors	Objectives	Critics outcomes
Development and performance evaluation of an active solar distillation system integrated with a vacuum-type heat exchanger	*Desalination*	2018	S.Gorjian, Ali Hosseini, Ahmad Banakar	In the present study, a solar distillation system combined with a solar parabolic trough concentrator and a vacuum-type heat exchanger with falling film technique has been developed and experimentally evaluated	The results obtained from the energy and exergy analysis, the highest energy and exergy efficiencies were obtained as 60.98% and 56.80% respectively
A detailed review of solar desalination techniques	*Int. J. Ambient Energy*	2018	H. Thakkar, A. Sankhala, P. V Ramana, and H. Panchal	The attempt is made to study different solar desalination techniques and find out the solution by combinations of varying desalination techniques for the small and arid region.	Integration of HDH system with Flash system could increase efficiency as well as distillate output.
Experimental Study and Analysis of Air Heating System using a Parabolic Trough Solar Collector Experimental Study and Analysis of Air Heating System using a Parabolic Trough Solar Collector,	*Int. J. Ambient Energy,*	2018	S. Nain, A. Parinam, and S. Kajal,	Experimental study of the air heating system was carried out using a parabolic trough collector with U-tube aluminium heat exchanger. An evacuated tube placed at the focal length of the parabolic trough, collected the solar radiations reflected from the surface of the parabolic trough.	It was observed that by using fins at a high mass flow rate of 4.557 kg/hr, the maximum temperature of 126°C was achieved, which is 13.27% more than the maximum temperature obtained without fins. Further, for a low mass flow rate of 1.69 kg/hr, the maximum temperature received was 149°C.
Thermal performance of solar parabolic trough collector at variable flow rates: An experimental investigation	*Int. J. Ambient Energy,*	2018	D. Kumar and S. Kumar	In this thermal study performance of the parabolic trough collector (PTC) is investigated experimentally at varying flow rates of the working fluid. Here, PTC is constructed with a simple structure having a nonevacuated tube and tested for tracking, and south facing mode utilising water as working fluid.	Mass flow rate is one of the key parameter influencing its performance.
Design of tracking system for helicalcoiled receiver tube of parabolic trough collector	*Int. J. Ambient Energy,*	2018	G. Mageshwaran, S. Ramachandran, K. Gobinath, and R. B. Durairaj	In the present work, a suitable tracking system is designed for helical-coiled receiver tube. The helical geometry decreases the concentration ratio, which in turn reduces efficiency. To increase the solar efficiency tracking is provided.	For keeping the operation and initial cost economical a single-axis tracking system with ‘A plane is rotated about northsouth axis horizontally with continuous adjustment to minimise the angle of incidence‘ is selected.
Parabolic trough collector with rhombus tube absorber for higher concentration ratio	*Energy Sources, Part A Recover. Util. Environ. Eff.,*	2018	R. K. Donga and S. Kumar	In the present study, the concentration ratio of the parabolic trough collector using rhombus tube absorber has been estimated. An analytical technique has been developed to determine the optimum size of the rhombus tube absorber for given trough dimensions.	The optimum size of the rhombus tube absorber is 13.8% smaller than the circular tube absorber for the LS3 trough with no change in intercept factor. The maximum improvement in the concentration ratio is found to be 31.5% for the troughs with a rim angle 90° in comparison to circular tube absorber.
Thermal efficiency enhancement of nanofluid-based parabolic trough collectors	*J. Therm. Anal. Calorim.*	2019	C. T. Evangelos Bellos	Investigated six different nanoparticles dissolved in thermal oil. Effect of varying concentration ratio, solar intensity and the flow rate was calculated using EES.	Cu concentrations of 6% were recorded maximum thermal efficiency of 0.74%.
Optical and thermal performance analysis of a micro parabolic trough collector for building integration	*Appl. Energy*	2020	M. Yang, M. A. Moghimi, Y. Zhu, R. Qiao, Y. Wang	Designed micro parabolic trough collector for building integration and determined optical and thermal performancetheoretically, experimentally	Annual optical efficiency was 67% and the instant thermal efficiency was 59% at 200 °C.